Computer Aided Medical Procedures
Prof. Dr. Nassir Navab

Dissertation

Advanced Hybrid Tracking and Navigation for Computer-Assisted Interventions

Tobias Reichl

Fakultät für Informatik
Technische Universität München

TECHNISCHE UNIVERSITÄT MÜNCHEN

Lehrstuhl für Informatikanwendungen in der Medizin & Augmented Reality

Advanced Hybrid Tracking and Navigation for Computer-Assisted Interventions

Tobias Christian Reichl

Vollständiger Abdruck der von der Fakultät für Informatik der Technischen Universität München zur Erlangung des akademischen Grades eines

Doktors der Naturwissenschaften (Dr. rer. nat.)

genehmigten Dissertation.

Vorsitzender: Univ.-Prof. Dr. Hans Michael Gerndt

Prüfer der Dissertation:

1.   Univ.-Prof. Dr. Nassir Navab

2.   Prof. Kevin Cleary, PhD

     Children's National Medical Center, Washington DC, USA

3.   a. o. Univ.-Prof. Dr. Wolfgang Birkfellner

     Medizinische Universität Wien, Österreich

Die Dissertation wurde am 11. Juli 2012 bei der Technischen Universität München eingereicht und durch die Fakultät für Informatik am 23. Februar 2013 angenommen.

Acknowledgments

This work would not have been possible without the work, help, support, and advice of supervisors, colleagues, friends, and family. All achievements described in this dissertation I owe to them, any errors and omissions are my own.

I would like to thank Nassir Navab for his support during and beyond this dissertation. I'm grateful for him sharing knowledge, but I'm even more grateful for him sharing wisdom and amazement about life. He taught me that "alone you can walk fast, but together you can walk far", and he has always been generous with his ideas and comments.

Thanks to Kevin Cleary and Wolfgang Birkfellner for reviewing this dissertation.

I would like to thank all the people who made my stay with the Chair for Computer Aided Medical Procedures and Augmented Reality so enjoyable. They are too numerous to name them all, but in particular (and in rough order of appearance) I'd like to thank Marco Feuerstein, Jörg Traub, Thomas Wendler, Jakob Vogel, Martina Hilla, Selen Atasoy, Dzhoshkun Shakir, Richard Brosig, Maximilian Baust, Alexandru Duliu, José Gardiazabal, and Philipp Matthies.

Thanks to Olivier Salvado, Josh Passenger, Oscar Acosta, and all the other folks at the Australian e-Health Research Centre, who made my stay in Brisbane, Australia, a truly great experience. Thanks to Kensaku Mori, Takayuki Kitasaka, Masahiro Oda, Xióngbiāo Luo, Jiang Wang, and Bin Chen for their hospitality at Nagoya University, Japan.

Finally I want to thank my wife Maren, my parents Johann and Gabriele, and my brother Michael for all their continuous love and support. It was from them that I learned the most important things in life.

Abstract

Modern surgery is transitioning from traditional open surgery to minimally invasive procedures, and intra-operative imaging is increasingly used to refine surgical planning and to precisely target regions of interest. One fundamental requirement for image-guided interventions is the accurate knowledge about the spatial relations between all objects of interest. We critically review clinically established tracking technologies, including optical and electromagnetic tracking, and novel, upcoming technologies. Optical tracking offers high accuracy and reliability, but requires a constant line of sight. Electromagnetic tracking is susceptible to distortions of the electromagnetic field, but does not depend on line of sight. It is currently the dominant technology for tracking of internal organs, and of flexible instruments within the human body, but still poses challenges in terms of non-uniform accuracy and noise.

This dissertation presents several new concepts for advanced hybrid tracking systems for computer-assisted interventions. First, the power of electromagnetic and optical tracking systems is amplified through mathematical modelling of a laparoscopic ultrasound transducer's flexible parts. We visualise the ultrasound images in a tracked laparoscope's video images, and via computer vision methods we close the loop to optimise the very same overlay accuracy, which is most important for live laparoscope video augmentation.

Then we demonstrate a novel approach to hybrid image-based and electromagnetic tracking, by modelling the output as continuous. Compared to previous methods, smoothness in terms of inter-frame motion is greatly improved.

Finally, we introduce a completely new tracking paradigm, by robotically keeping the electromagnetic tracking sensor always close to the centre of the tracking volume, in order to minimise electromagnetic tracking errors. This is the first general solution providing uniform tracking accuracy throughout the volume. In particular, this solution improves tracking accuracy by a factor of two, while at the same time extending the tracking volume up to the reach of the robot.

The methods presented in this dissertation were developed in close collaboration with medical partners. In order to meet clinical requirements for use on real patients, they were thoroughly evaluated on phantoms and ex-vivo animal specimens. In a conclusion we demonstrate, how such advanced hybrid tracking solutions can be used to approach abdominal settings, where just a decade ago tracking might have been dismissed as impossible.

Keywords: Image-Guided Interventions, Computer-Aided Surgery, Hybrid Tracking Systems, Medical Augmented Reality

Zusammenfassung

Moderne Chirurgie befindet sich im Übergang von der traditionellen, offenen Chirurgie zu minimal invasiven Eingriffen, und intra-operative Bildgebung wird immer mehr genutzt, um chirurgische Planung anzupassen und Zielregionen präzise anzusteuern. Eine Grundlegende Voraussetzung für bildgestützte Chirurgie sind genaue Informationen über die räumliche Lage aller relevanten Objekte. Wir betrachten klinisch etablierte Technologien wie optisches oder elektromagnetisches Tracking und neue, aufkommende Technologien. Optisches Tracking bietet eine hohe Genauigkeit und Zuverlässigkeit, benötigt aber eine konstante Sichtverbindung. Elektromagnetisches Tracking ist empfindlich für Störungen des elektromagnetischen Felds, aber hängt nicht von einer Sichtverbindung ab. Es ist aktuell die vorherrschende Technologie, innere Organe oder flexible Instrumente innerhalb des menschlichen Körpers zu verfolgen, aber bietet immer noch Herausforderungen in Bezug auf nicht gleichförmige Genauigkeit und Rauschen.

Diese Dissertation stellt mehrere neue Konzepte für erweiterte hybride Trackingsysteme für computer-unterstützte Eingriffe vor. Zunächst werden die Möglichkeiten von elektromagnetischen und optischen Systemen dadurch verstärkt, flexible Teile einer laparoskopischen Ultraschall-Sonde mathematisch zu modellieren. Wir stellen die Ultraschallbilder innerhalb von Videobildern eines nachverfolgten Laparoskops dar. Über Methoden des Bildverstehens schließen wir den Kreis, und wir optimieren genau die Überlagerungsgenauigkeit, die für die Augmentierung von laparoskopischen Videobildern am meisten bedeutsam ist. Dann stellen wir einen neuen Ansatz für hybrides bildbasiertes und elektromagnetisches Tracking vor, indem wir die Ausgabe als kontinuierlich modellieren. Im Vergleich zu früheren Methoden wird die Stabilität im Hinblick auf Bewegung zwischen einzelnen Videobildern deutlich verbessert. Schließlich zeigen wir eine völlig neue Sichtweise auf, indem wir einen elektromagnetischen Sensor mit Hilfe eines Roboters stets im Zentrum des Tracking-Volumens halten, um die Fehler von elektromagnetischem Tracking zu minimieren. Dies ist die erste allgemeine Lösung, gleich bleibende Tracking-Genauigkeit über das gesamte Volumen hinweg zur Verfügung zu stellen. Insbesondere verbessert diese Lösung die Tracking-Genauigkeit um einen Faktor von zwei und erweitert gleichzeitig das Tracking-Volumen bis zur Reichweite des Roboters.

Die Methoden, die in dieser Dissertation vorgestellt werden, wurden in enger Zusammenarbeit mit medizinischen Partnern entwickelt. Um klinische Anforderungen für die Anwendung an tatsächlichen Patienten zu erfüllen, wurden diese Methoden sorgfältig an Phantomen und tierischen Proben ex vivo getestet. Als Abschluss zeigen wir auf, wie solche erweiterten hybriden Tracking-Lösungen benutzt werden können, abdominelle Aufgabenstellungen anzugehen, die vor gerade einmal zehn Jahren noch als unlösbar hätten gelten können.

Schlagwörter: Bildgestützte Chirurgie, Computerunterstützte Chirurgie, Hybride Trackingsysteme, Medizinische Erweiterte Realität

Contents

1. Introduction: Image-Guided Interventions

"The winds and waves are always on the side of the ablest navigators." – Edward Gibbon

1.1. Image-Guided Interventions

In image-guided interventions, surgical tools and devices are intra-operatively localised and tracked, pre-operative 3-D images are registered to physical space, and tools and devices are visualised with respect to these pre-operative images [Pete 08]. Increasingly, intra-operative imaging is used to refine surgical planning and to precisely target regions of interest.

Nowadays, there is a growing number of commercially available solutions for image-guided interventions like StealthStation (Medtronic, Louisville, CO, USA) for neurosurgery, iLogic (superDimension, Minneapolis, MN, USA) for bronchoscopy, or declipseSPECT (SurgicEye, München, Germany) for surgical oncology.

Notwithstanding the importance of other sub-tasks like visualisation, tracking is an essential component for image-guided interventions. Accuracy and integration requirements are ever increasing, or vice versa, ever increasing accuracy and better integration enable novel applications, and image-guided interventions are gradually expanding from neurosurgery and orthopaedic surgery to other disciplines like endoscopic [Gild 05, Haut 05, Eber 07] or abdominal surgery [Klee 06, Rass 09].

Tracking systems have to meet strict clinical requirements regarding accuracy and reliability, but also seamless integration into the workflow. Clinically established tracking technologies are optical and electromagnetic tracking. Optical tracking offers high accuracy and reliability, but requires a constant line of sight. Electromagnetic tracking is susceptible to distortions of the electromagnetic field, but it does not depend on line of sight. It is currently the dominant technology for tracking of internal organs, and of flexible instruments within the human body, but still poses challenges in terms of non-uniform accuracy and noise.

1.2. Outline and Major Contributions

After a critical review of established and upcoming tracking technologies, we demonstrate calibration and registration techniques for intra-operative tracking and navigation. This dissertation then presents several new concepts for advanced hybrid tracking systems for computer-assisted interventions.

1.2.1. Hybrid Magneto-Optic Tracking of Laparoscopic Ultrasound

Related Work: Electromagnetic tracking of laparoscopic ultrasound has been proposed for augmentation of laparoscopic images [Harm 01, Ells 04, Kruc 05]. Electromagnetic tracking alone, however, is susceptible to tracking errors from distortions of the electromagnetic field. Hybrid optical and electromagnetic tracking systems for laparoscopic ultrasound were proposed [Naka 02, Koni 07, Naka 08a], in order to overcome this limitation. Similarly, tracking of a robotically controlled laparoscopic ultrasound transducer was presented [Leve 05], but none of these approaches consider the bending of the laparoscopic probe's flexible parts, and none are suitable to detect or correct dynamic tracking errors, which occur due to varying distortions of the electromagnetic tracking field.

Contribution: [Feue 07, Feue 08b, Feue 09] The power of electromagnetic and optical tracking systems is amplified through mathematical modelling of a laparoscopic ultrasound transducer's flexible parts. Tracking accuracy is optimised intra-operatively in real-time. We visualise the ultrasound image in a tracked laparoscope's video images, and via computer vision methods we close the loop to optimise the very same overlay accuracy, which is most important for live laparoscope video augmentation.

1.2.2. Hybrid Image-Based Tracking with Smooth Output

Related Work: Bronchoscope tracking by electromagnetic tracking systems has been proposed more than a decade ago [Solo 98], as well as "virtual bronchoscopy", where bronchoscopy-like images are rendered from pre-operative computed tomography (CT) volumes [Engl 98, Aqui 99, Hapo 99]. Shortly after, bronchoscope tracking by 2-D/3-D registration between the real 2-D video images and the 3-D CT volume was proposed [Mori 00, Sher 00], and later extended to hybrid image-based and electromagnetic tracking for bronchoscopy [Mori 05, Sope 09]. In these approaches electromagnetic tracking is used as an initialisation for the image registration. The numerical optimisation, however, is prone to local minima, and small changes in the initialisation from electromagnetic tracking may lead to different local minima. Thus, noise from electromagnetic tracking is amplified by hybrid tracking.

Contribution: [Luo 10b, Reic 11, Reic 12] We demonstrate a novel approach to hybrid image-based and electromagnetic tracking, by modelling the output as continuous. We model the output using Catmull-Rom splines for position and spherical linear interpolation (SLERP) of quaternions for rotation. Compared to previous methods, smoothness in terms of inter-frame motion is greatly improved.

This approach leads to an extensible framework for registration to preoperative CT images, and we provide a thorough evaluation of our approach using expert-provided ground truth data, including quantitative measurements for these experts' performance.

1.2.3. Electromagnetic Servoing

Related Work: Co-calibration between optical and electromagnetic tracking systems has been proposed [Birk 98a, Naka 00, Naka 02], in order to at least partly avoid the line of

sight limitation for optical tracking systems by switching to electromagnetic tracking in case of obstruction. It has been noted before [Fran 03, Schn 07] that electromagnetic tracking accuracy is not uniform across the tracking volume. Recently, a novel compact field generator for electromagnetic tracking with limited tracking volume was presented for applications, where the field generator is mobile (Northern Digital, Waterloo, ON, Canada).

Contribution: We introduce a completely new tracking paradigm, by robotically keeping the electromagnetic tracking sensor always close to the centre of the tracking volume, in order to minimise electromagnetic tracking errors. This is the first general solution providing uniform tracking accuracy throughout the volume. In particular, this solution improves tracking accuracy by a factor of two, while at the same time extending the tracking volume up to the reach of the robot.

2. Tracking Technologies – State of the Art

In this chapter we will critically discuss the clinically established tracking technologies, including optical and electromagnetic tracking, and novel, upcoming technologies, including radio frequency identification (RFID) and fibre-optic tracking. Tracking systems need to be carefully evaluated with regard to clinical requirements, and in general, the choice of the optimal tracking technology will be highly application-specific.

During the last decade mostly two technologies have become clinically accepted and put into widespread use: optical tracking, and electromagnetic tracking. Both have been evaluated for surgical use, and found to provide sufficient accuracy for e.g. orthopaedic surgery [Spar 03] or neurosurgery [Masc 05].

Examples for optical tracking systems include the Polaris and Optotrak systems (Northern Digital, Waterloo, ON, Canada), and ARTtrack (Advanced Realtime Tracking, Weilheim, Germany). Examples for electromagnetic include the Aurora (Northern Digital) and 3DGuidance medSAFE systems (Ascension Technology, Burlington, VT, USA), for both of which there are miniature sensors available. Sensors of the Fastrak system (Polhemus, Colchester, VT, USA) are several centimetres wide and mostly targeted towards motion capture.

Besides these, there is an ever growing number of application-specific systems incorporating optical and/or electromagnetic tracking systems: VectorVision (Brainlab, Feldkirchen, Germany), StealthStation (Medtronic, Louisville, CO, USA), PercuNav (Philips, Hamburg, Germany), eNLite (Stryker, Freiburg, Germany), and others.

Optical tracking systems are accurate and reliable, but need a constant line of sight. Electromagnetic tracking systems can operate without a line of sight, but require a carefully controlled environment in order to avoid distortions of the electromagnetic tracking field. Due to the various influences in the operating room, all tracking systems in general perform worse there than specified for an ideal environment [Wagn 02].

2.1. Optical Tracking

For optical tracking two or more cameras are used, which are mounted in a known, fixed configuration, e.g. ceiling-mounted. Dedicated fiducials or "markers" are segmented in camera images. There are several designs for such markers, which can be distinguished into visible-light patterns, passive retro-reflective infra-red markers, and active infra-red light-emitting diodes (LEDs).

Visible-light patterns can be segmented in regular visible-light video. These patterns have high contrast edges for robust segmentation, and one particular advantage is that only a single video stream is required for both tracking and recording of the scene. Compact tracking systems based on this technology are available (MicronTracker, Claron, Toronto, ON, Canada) [Deke 05]. However, robustness suffers in cluttered environments.
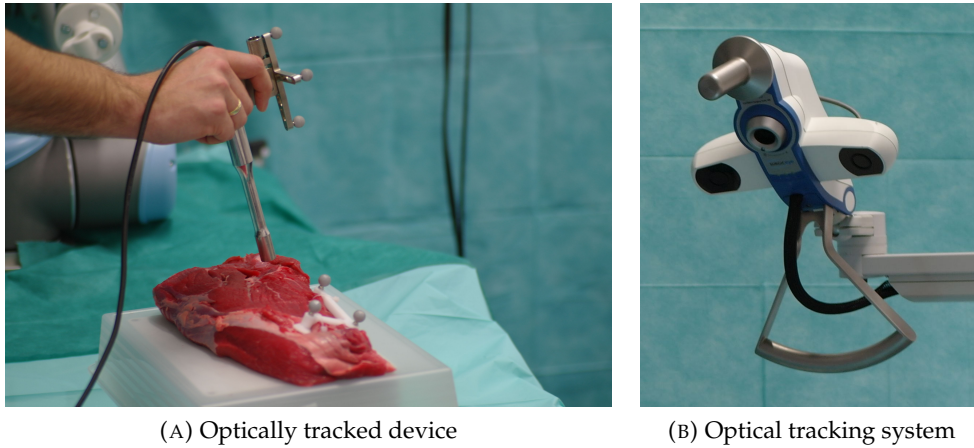
(A) Optically tracked device   (B) Optical tracking system

FIGURE 2.1.: **Optically tracked device, and optical tracking system. 2.1a) Optical tracking targets are mounted on an intra-operative hand-held gamma probe, and on an ex-vivo phantom. 2.1b) declipseSPECT imaging system (SurgicEye), including an optical tracking system. There are rings of infra-red strobe lights around the two tracking cameras left and right.**

Instead of visible light, images can be taken in the invisible near infra-red spectrum. Then, additional illumination is possible without disturbing the users, and markers have a well-defined, bright appearance in the camera images, since there are usually no other sources of near infra-red illumination.

Passive retro-reflective infra-red markers are usually spheres and used in a "passive" configuration, where the scene is illuminated by strobe lights close to the cameras. An example of such an optical tracking system is shown in Figure 2.1. Spheres are particularly suitable, since the image of a sphere is always a circle, regardless of orientation. These circles may be segmented with sub-pixel accuracy using standard image-processing techniques – a spherical fiducial can typically be segmented with 0.04 pixel accuracy, as long as it covers at least three pixels in the image [Adva 12]. However, all markers look identical and tracked objects need to be distinguished at a later stage.

Several implementations of retro-reflection are possible: Retro-reflective coatings like "Scotchlite" (3M, Neuss, Germany) are used, which are densely packed with a large number of miniature wide-angle retro-reflective lenses, or transparent spheres with a refractive index of 1.9. and a reflective coating on the rear part [Brun 06].

When *active infra-red light emitting diodes* (LEDs) are used, no additional illumination from the cameras is needed. Since groups of LEDs can be triggered separately, identification is implicit, and tracked objects can be distinguished. Active systems are usually wired, but wireless active targets are also available (Advanced Realtime Tracking).

A fixed arrangement of three or more markers or LEDs with known, non-symmetric configuration constitutes a "target" and it is fixed to tools, patient, or other objects to be tracked, as shown in Figure 2.1a. A non-symmetric configuration is needed in order to have a unique relation between the target pose and the resulting camera images. Targets

may consist of more than three markers, and the resulting redundancy increases accuracy. Also, an object can still be tracked, even if some markers are occluded, as long as at least three markers are visible.

With passive infra-red systems, each target has to have a unique geometry, since the markers themselves appear identical. With active infra-red systems, targets may be identical, since they are activated in sequence.

The three-dimensional position of each marker can be triangulated, if it is visible in at least two camera images, and position and orientation of targets may be computed, if the position of at least three of their markers is known. There is a trade-off between tracking accuracy and the geometry of the tracking system set-up: The larger the distance, or base-line, between the cameras, the better the marker detection accuracy (fiducial registration error), but this requires a bigger housing for fixed, factory-calibrated camera arrangements, or separately mounted cameras, which then need additional calibration. Similarly, the greater the distance between markers of a single target, the better the target position and orientation error (target registration error), but larger targets may be more unwieldy.

Variations: Instead of at least two 2-D cameras, it is also possible to use at least three line (1-D) cameras, which yields a higher accuracy of 0.1 mm and update rate of 4600 Hz, but such systems are usually heavier and bulkier than those with 2-D cameras. Examples of 1-D camera systems include the Optotrak Certus (Northern Digital) [Nolt 95] and FlashPoint systems (Stryker, Freiburg, Germany) [Tebo 96]. Laser-based systems also exist (laserBIRD 2, Ascension Technology), but these have lower accuracy of 0.7 mm [Asce 04].

Static cameras can track moving targets in an "outside-in" configuration. Here, the position of the targets can be triangulated well, depending on the length of the base-line between the cameras. Orientation of targets, however, is less precise than position and depends on the size of the targets. In contrast, it is possible to use a single, moving camera in an "inside-out" configuration with fixed targets [Hoff 00, Vogt 02]. Here, the orientation of the camera can be determined with very good accuracy, at the price of lower position accuracy. This is desirable in certain cases, where the orientation of a moving object is more important than position. For example, the view direction needs to be known precisely in the case of head-mounted displays for medical augmented reality applications [Trau 08].

An interesting variant of optical tracking involves retro-grate reflectors and moire patterns for 6-D visual tracking, yielding high orientation accuracy of $0.04°$ (2.6') [Arms 07, Arms 11]. Such patterns need to have a visible footprint of 60×60 pixels, which means that with a marker sizes of 65×65 mm and a 1.3 Mega-pixel camera, a tracking volume of approximately $1 \times 1 \times 1.5$ m is usable. A higher camera resolution enables a smaller minimum marker size, a larger tracking volume, or a combination of these two [Wein 10].

Optical tracking systems may have a pre-configured relative camera geometry, which allows factory calibration and a guaranteed accuracy during operation. Thus, such systems are usually favoured in medical applications. For other applications like motion capture, flexibility or a larger number of cameras may be more important, and thus there are other products (ARTtrack3, Advanced Realtime Tracking), where a calibration of the camera set-up by the user is required.
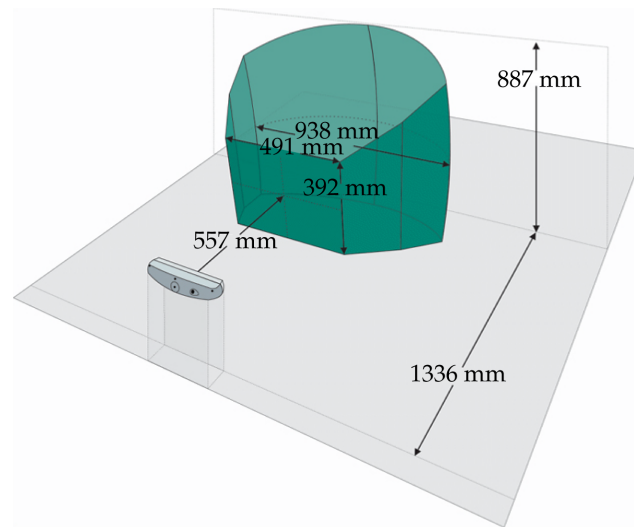
FIGURE 2.2.: **Tracking volume of Northern Digital Polaris Vicra optical tracking system. Image courtesy of Northern Digital.**

Properties: In comparison to other tracking technologies, optical tracking offers a reasonably large working volume of typically one cubic metre and more (cf. Figure 2.2) and sub-millimetre accuracy. Typical volumetric accuracies for optical tracking systems are 0.2 mm for position and 0.4° for orientation [Wile 04]. From the visibility of markers and from measures like roundness of segmented marker images, instantaneous feedback about the quality of tracking can be provided by the tracking system. From previous knowledge about the segmentation uncertainty and the camera set-up geometry, target registration errors can be estimated in real-time [Baue 07, Siel 07], and targets can be optimised for tracking accuracy [West 04]. Targets can typically be sterilised, and if a reference target fixed to the patient or operating room bed is used, the camera set-up may be moved around freely, and the tracking system integrates well into the clinical workflow.

Drawbacks of optical tracking are that tracking targets are rather large (ten centimetres and more in diameter) and that there is a need for a constant unobstructed line of sight. If the point of interest is the tip of a rigid, laparoscopic instrument, which is inside the patient during minimally invasive surgery, an optical tracking target can be mounted at the shaft of the instrument outside the body, and optical tracking is still possible.

2.2. Electromagnetic Tracking

The clinical relevance of electromagnetic (EM) tracking is high for endoscopic applications [Hayh 09, Abda 09], including colonoscopy [Chin 10], neuroendoscopy [Hayh 09], bronchoscopy [Abda 09], and for catheter navigation [Erik 09, Khay 11]. Besides EM tracking, there is not yet a general solution for tracking of *flexible* instruments within the human body. However, EM tracking systems in general do not yet provide the same level of accuracy as optical tracking systems and are susceptible to distortions from secondary EM fields due to metallic objects in the vicinity.
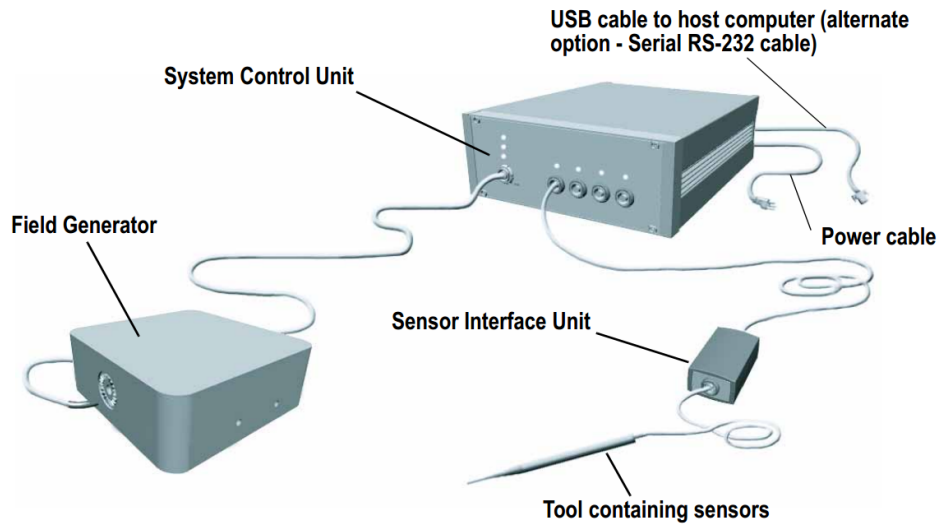
FIGURE 2.3.: **Aurora electromagnetic tracking system. Image courtesy of Northern Digital.**

As part of an electromagnetic (EM) tracking system a field generator, also called transmitter, creates an EM field with spatially and temporarily variable field strength. Sensors measure the EM field strength or magnetic flux, and from multiple measurements the position and orientation of each sensor relative to the field generator can be computed. For a complete illustration of the EM tracking set-up, please refer to Figure 2.3.

Technology: In earlier publications, e.g. by Raab *et al.* [Raab 77, Raab 79] or Kuipers [Kuip 80], three inductive coils in the field generator as well as in each sensor were proposed. In three time phases, each field generator coil in turn is switched on to create an EM field, which is measured by all sensor coils. Thus, each sensor measures the field strength one dimension at a time, and from these 3×3 measurements per sensor, all six degrees of freedom for position and orientation of the sensor can be computed [Egli 81, Raab 82]. Other sensing techniques, which are suitable for static fields, include Hall effect sensors or fluxgate magnetometers.

Later designs arrange six or nine coils in a tetrahedral configuration in the field generator [Seil 00, Kirs 03] (cf. Figure 2.4), since then it is possible to determine five degrees of freedom from the 6×1 or 9×1 measurements of a single sensor coil – the rotation around the sensor coil's axis is undetermined. Thus, sensors may consist of only a single coil each and be much smaller. For tracking of all six degrees of freedom, two 5-D sensors are combined in a non-parallel manner, and then the missing degree of freedom can be determined as well.

Variations: Alternatively, an EM field may be generated using an ensemble of six patches with coils, which are placed on the skin all around the patient, as in the commercially available "Ensite NavX" catheter tracking system (Endocardial Solutions, St. Paul, MN, USA) [Krum 05]. Two opposite patches each define one of three approximately orthogonal
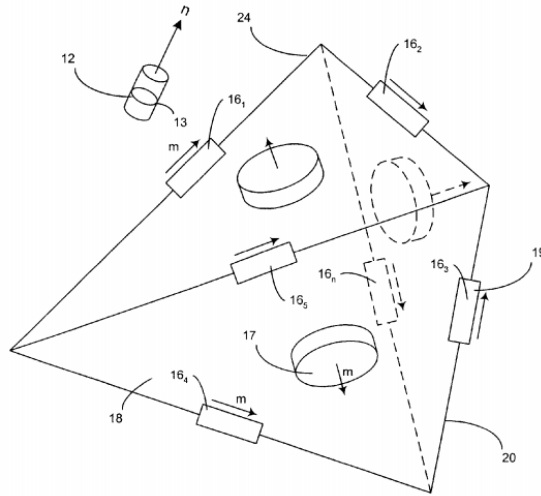
FIGURE 2.4.: **Electromagnetic tracking field generator with tetrahedral configuration. There is one coil on each of the six edges of the tetrahedron, and one each on the three upper faces [Kirs 03].**

axes, which are then used as a 3-D coordinate system for tracking.

Following the same physical principles, the motion of transmitters integrated into an endoscope can be tracked relative to fixed receivers outside the patient (ScopeGuide, Olympus Optical, Tokyo, Japan), or in another system an implanted permanent magnet can be localised by sensors outside the body [Shim 05].

A wireless system is the "GPS for the Body" localisation system (Calypso, Seattle, WA, USA). With this system, a set of three transponders (8.5 mm length) is used to track a single target's position. For example, the transponders may be implanted into an organ through a 14-gauge needle (i.e. 1.6 mm inner diameter) and registered. The measurement volume is rather small with $150 \times 150 \times 270$ mm, the update rate is 10 Hz, and the system is only able to track a single target. For real-time organ tracking for prostate radiotherapy an error of 2.0 mm or better was determined [Balt 05, Will 06, Kupe 07], and integration into an augmented reality system was proposed [Naka 08b].

Properties: Electromagnetic (EM) tracking sensors can be miniaturised, as shown in Figure 2.5. Sensors are commercially available with an outer diameter of 0.3 mm (5-D sensors) or 0.9 mm (6-D sensors). This provides high potential for integration into probes or other tools, even needles or catheters. Theoretically, an arbitrary number of sensors may be tracked in close proximity at the same time, since sensors do not interfere with each other. In practice, most EM tracking systems are limited to four 6-D or eight 5-D sensors.

EM tracking systems do not need a line of sight between field generator and sensors, since the human body is transparent for EM fields in the applied frequency range [Gabr 96]. This makes EM tracking the most generally applicable method for the tracking of flexible instruments in minimally invasive applications.

EM tracking systems have best accuracy close to the field generator, since the strength
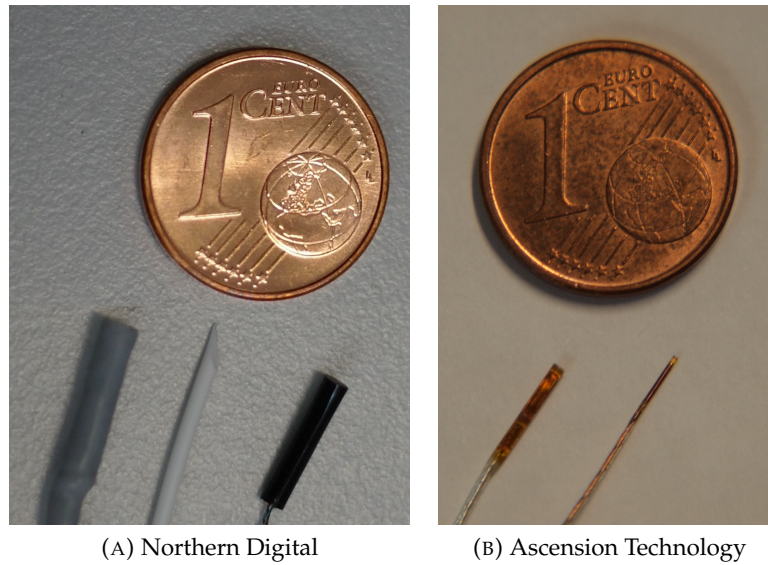
(A) Northern Digital   (B) Ascension Technology

FIGURE 2.5.: **Electromagnetic tracking sensors, from left to right: 2.5a) Northern Digital 6-D cable tool, 6-D catheter, 6-D sensor; 2.5b) Ascension Technology model 90 6-D sensor, model 30 5-D sensor.**

of the EM field decreases with greater distance. However, the closer to the field generator, the more inhomogeneous the EM field. Also, a 5-D sensor's accuracy strongly depends on its orientation, with the worst accuracy in the case, when the sensor is pointing towards the field generator, or away from it [Fran 03, Shen 08].

EM tracking systems typically provide an accuracy of 1.5 mm for position and $0.4°$ for orientation [Fran 03], which is lower than the accuracy of optical tracking systems. However, EM tracking may be used without a line of sight, e.g. with flexible endoscopes or catheters, which are completely inside the patient patient and where the position of the tip can no longer be related to parts on the outside.

Since EM tracking sensors, due to their small form factor, can be integrated close to the point of interest, tracking error for this point may actually be lower than with optical tracking. Typical volumetric accuracies for optical tracking systems are 0.2 mm for position and $0.4°$ for orientation [Wile 04]. For example, if the distance between the optical tracking target and the point of interest is 300 mm, the orientation uncertainty results in approximately $\sin(0.4°) \cdot 300 \approx 2.1$ mm of additional position uncertainty. In contrast, the EM tracking sensor may be placed only few millimetres from the point of interest, which results in smaller total error.

Tracking volume is smaller than for optical tracking, typically $50 \times 50 \times 50$ cm as shown in Figure 2.6. Also, the detection of tracking errors is not as straightforward as for optical tracking systems. Most EM tracking systems provide a "quality" measure or another indication of tracking accuracy, which may be derived e.g. from consistency between the measurements of the two 5-D sub-sensors contained in a 6-D sensor.

As with optical tracking systems, the target tracking error (TTE) may be estimated from
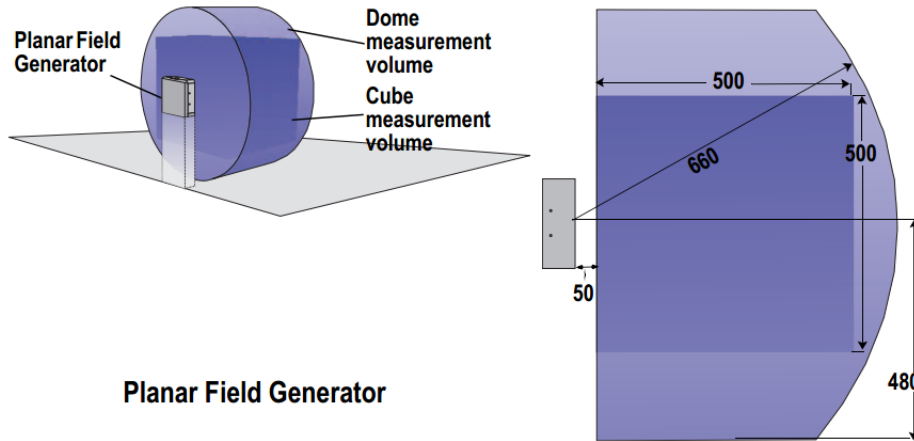
FIGURE 2.6.: **Tracking volume of Northern Digital Aurora electromagnetic tracking system. Image courtesy of Northern Digital.**

fiducial location error (FLE) for EM tracking systems [Wile 10]. Assuming (simplified) isotropic error and linear error propagation, methods for tool design from optical tracking systems [West 04] have also been applied for EM tracking systems [Tang 03, Fisc 05a, Fisc 05b], i.e. how to distribute multiple sensors in a single tool.

There is a trade-off between tracking accuracy and tracking volume. For example, Northern Digital's standard Aurora field generator is capable of switching between two pre-configured working volumes, which either provide a larger volume, or better accuracy. In principle, arbitrary realisations of this trade-off are possible in the form of custom-calibrated tracking volumes.

Distortions of the Electromagnetic Field: A considerable problem in clinical applications of EM tracking is the possibility of distortions of the EM tracking field. Such distortions may be caused by metallic or electronic components in the vicinity of the tracking volume, e.g. surgical instruments, operating room (OR) tables, or imaging devices like C-arms. In medical imaging settings, errors of up to 7 mm have been reported [Poul 02, Wils 07, Yani 09], with significant variations between different OR set-ups and devices – compared to 1-2 mm in distortion-free environments. Clinical studies, however, mention that interferences from metal objects in the magnetic field were rarely seen intra-operatively [Wagn 02, Masc 05]. In general, the performance of EM tracking systems strongly depends on a carefully controlled environment.

From theoretical considerations Raab *et al.* [Raab 79] derived the rule of thumb that a metallic object, whose distance from the field generator is at least twice the distance between field generator and sensor, has an influence of less than one percent on the magnitude of the EM field. Nixon *et al.* [Nixo 98] presented a detailed prediction that e.g. metal effects on EM tracking systems decrease as the third power of field generator-metal separation and the third power of sensor-metal separation.

Distortions may be due to ferromagnetic materials (iron, cobalt, nickel, and others, cf. Figure 2.7) in the environment, or due to eddy currents, which are induced in conductive

(A) Non-ferromagnetic material   (B) Ferromagnetic material
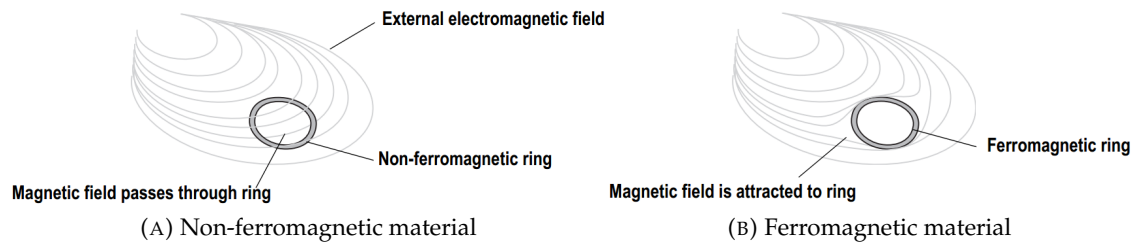
FIGURE 2.7.: **Effects of ferromagnetic materials on a static electromagnetic field. 2.7a) Non-ferromagnetic materials do not influence a static electromagnetic field. 2.7b) Ferromagnetic materials do distort the static electromagnetic field. Images courtesy of Northern Digital.**
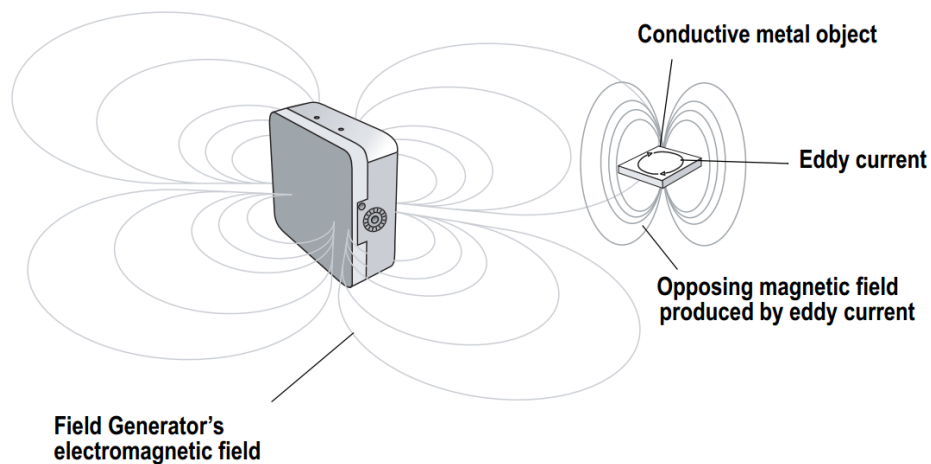

FIGURE 2.8.: **Effect of eddy currents on changing magnetic field. The changing magnetic field induces eddy currents, which in turn lead to secondary electromagnetic fields. Image courtesy of Northern Digital.**

metals (e.g. copper or aluminium, cf. Figure 2.8) by a changing EM field. Eddy currents in particular affect AC tracking systems like the Aurora (Northern Digital). Metals with high electrical conductivity or high magnetic permeability affect tracking systems more than metals with low conductivity and low permeability, such as 300 series stainless steel, or titanium [Leot 97]. DC tracking systems like the 3D Guidance medSAFE (Ascension Technology) avoid this source of distortions by employing quasi-static magnetic fields and estimating the steady state values, i.e. after eddy currents die out [Das 85]. This provides higher robustness against distortions from conductive metals, but in turn leads to a higher sensitivity against static distortions, e.g. from ferromagnetic materials. In the last years, the robustness of EM tracking systems against distortions has significantly been improved [Kirs 06, Schn 10, Niem 11]. "Table-top field generators" may contain shielding made of materials with high magnetic permeability, but low conductivity, e.g. ferrite or mu-metal, on top of a conductive plate, e.g. aluminium. This combination effectively blocks distortion from metallic objects below the field generator, e.g. from an operating room table [Ashe 01, Ashe 03]. Such table-top field generators are available for both the Aurora (Northern Digital) and 3DGuidance medSAFE systems (Ascension Technology).

To improve accuracy there have been numerous approaches towards the compensation of static errors [Kind 00], but these require a lengthy calibration procedure and do not hold up in a highly dynamic environment like an operating room (OR). Other approaches towards dynamic error compensation employ other sources of information like segmentation [Gerg 10], image registration [Mori 05], or hybrid tracking and models of instrument motion [Feue 09]. In any case, these approaches are highly application-specific, rely on static pre-operative images, or are not yet feasible in real-time.

Static Error Compensation: In order to compensate for *static* distortions of the field, it is possible to determine in a calibration procedure the distortion at each point in space, using other tracking systems as ground truth, e.g. optical tracking. Intra-operatively, corrected values are then derived from the distorted measurements by look-up tables or via polynomial interpolation [Kind 00, Bors 04, Chun 04, Fisc 05a, Naka 08a]. Commonly, an extensive and well-defined set of distorted and undistorted measurements is needed. Unfortunately, this procedure is extremely time-consuming and may only be used with static distortions, i.e. an non-dynamic set-up, where neither the location of the EM field generator, nor the causes of distortion are moved after calibration. If any of these change, the calibration procedure has to be repeated.

In addition, the amount of distortion depends on sensor orientation [Shen 08]. Thus, a complete correction model would need to consider at least five degrees of freedom, and the resulting sample size would be prohibitive. Even for coarse grids, 8640 measures for a single calibration procedure have been reported [Day 00]. During operation the compensated value needs to be determined from the corrupted measurement, so the mapping needs to be bijective. Thus, this compensation is not applicable for larger errors, i.e. when measurements at multiple different locations yield the same corrupted values.

Dynamic Error Detection: First steps towards detection of dynamic errors were presented [Birk 98a, Much 06], using the measurements from two sensors, which were fixed relative to each other. The distance between both sensors is known, so inter-operatively

this known distance may be monitored for changes, which indicate tracking errors possibly due to distortions of the EM tracking field. Since all six degrees of freedom are fixed between the two sensors, even all of them could be monitored, instead of a single distance measurement.

2.3. Mechanical tracking

Mechanical arms with joint encoders or potentiometers, e.g. FARO Gage (FARO, Korntal-Münchingen, Germany), can compute the precise position and orientation of their end effector via forward kinematics, i.e. from their joint angles and the known geometry of the segments. Such systems offer unsurpassed accuracy of typically up to 25 μm. Before other, contact-free technologies like optical or electromagnetic tracking became available, mechanical tracking was used for image-guided interventions, e.g. for intra-operative tracking of ultrasound probes [Come 98].

However, a mechanical arm restricts motion, it has considerable inertia due to its weight (9.1 kilograms for the FARO Gage), can track only one object, and needs continuous mechanical contact. In addition, sterilisation is difficult, and thus mechanical tracking is far less prevalent in clinical use than optical and electromagnetic tracking.

Of course, when robotic surgery systems like the "da Vinci" surgical system (Intuitive Surgical, Sunnyvale, CA, USA) are used, position measurements from these may be used as well [Leve 05].

2.4. Other and Novel Tracking Technologies

Besides optical, electromagnetic, and mechanical tracking, other technologies may not have gained clinical acceptance yet (or may haven fallen out of favour again), but are worth a short description.

Ultrasound Tracking: Via time of flight the distance between ultrasound emitters and receivers can be computed. Multiple emitters and receivers in known configuration enable the determination of relative position and orientation. Position accuracy, when combined with inertial sensors, is typically 2-3 mm (IS-900, InterSense, Billerica MA, USA) and thus lower than optical or electromagnetic tracking. Like optical tracking, ultrasound tracking needs a free line of sight between emitters and receivers, and accuracy varies with the speed of sound, which depends on temperature, humidity, and pressure (in air) [Ghaz 95], or material properties (in tissue) [Ande 00].

Prototypes for real-time ultrasound catheter localisation have been reported with accuracy of 2-3 mm [Mung 11] with an internal ultrasound pulser and an external array of sensors.

Inertial Tracking: There are different kinds of gyroscopes, which may be used for inertial tracking. In a MEMS (Micro Electro-Mechanical System) sensor, the Coriolis effect is used to measure angular velocity, and integration then yields angular change. However, due to integration of measurements, even small errors lead to a strong drift, which needs

intermittent correction. For example, the earth's magnetic field may be used to correct drift within the horizontal plane, like a compass. Inertial sensors may be very small, like electromagnetic tracking sensors, and can be unobtrusively integrated in instruments. Inertial tracking was used for endoscopic image re-orientation [Holl 09], 3-D ultrasound tracking [Hous 08], or for touch-less, non-intrusive intra-operative gesture recognition [Bigd 12].

RFID Localisation: For the tracking of radio frequency identification (RFID) tags relative to the receiver, commercially available products currently have an accuracy of one metre (Mojix STAR, Mojix, Los Angeles, CA, USA). However, similar to the Calypso system described above, new developments enable millimetre accuracy localisation of RFID tags using phase difference [Heki 10, Will 11]. A localisation accuracy of 2 mm seems to be possible today, and due to its wireless nature, the inherent identification capability, and the extremely small size of RFID tags, this technology is very promising.

Fibre-Optic Tracking: Owing to modern optics, it is possible to measure strain and temperature quasi-continuously along an optical fibre. With a technology called "coherent optical fibre frequency domain reflectometry", a laser signal is sent into an optical fibre and the frequency spectrum of the backscattered interference signal can be used as a stable "fingerprint" of the fibre. This fingerprint is caused by local imperfections in the fibre, and each location in the optical fibre corresponds to a certain frequency in this spectrum. Commercially available reflectometers (Luna Technologies, Blacksburg, VA, USA) can measure 7 million data points along a 70 m long fibre, which corresponds to a spatial resolution of 10 μm.

Temperature changes or axial displacement causes shifts of the fingerprint in the frequency domain, and thus temperature or strain can be measured. The combination of multiple fibres enables determination of curvature, and integration then enables determination of position and orientation for each point along the fibre. This technology is extremely promising, but not yet generally available.

The commercially available "ShapeTape" device (Measurand, Fredericton, Canada) operates on a different principle, where light is lost along short "loss zones" on the side of the fibre on a beryllium-copper substrate, and transmission varies linear with curvature [Dani 99b]. The ShapeTape device has already been used to track a 2-D ultrasound probe for freehand 3-D ultrasound [Pago 00, Hous 07], for endoscopic 3-D ultrasound systems [Koiz 02], or for measurement of body-seat interface shape [Li 04], but accuracy was determined to be too low to be useful [Koiz 02, Bail 03a].

Optical Flow Sensors: For application-specific tasks, highly specific alternative tracking solutions may be devised. Just as an example, in order to measure movement of a flexible instrument at the insertion point, optical flow sensors (as in computer mice) have been proposed [Corn 11, Luo 11]. This may give information about insertion depth or rotation, but needs to be fused with other sources of information for completeness. For example, such information could be fused with models of valid endoscope shapes within the body [Kuku 02], in order to infer information about the position of the endoscope tip.

Computer Vision: Of course, there is also a huge body of work on tracking in computer vision. Image-based tracking, i.e. based on segmentation of intra-operative images, has been proposed for interventions, where tools are already required to be constantly observed via imaging systems. Examples include ultrasound-guided needle biopsy [Ding 03], or catheter tracking in fluoroscopy [Paul 10]. The recently released Prime-Sense/Kinect depth camera has triggered huge interest in applications like gesture recognition and others.

Similar to optical tracking it is possible to detect implanted fiducial markers in fluoroscopy [Fall 10a, Fall 10b], or to locate a single radioactivity source with collimated, moving detectors and triangulation [Shch 10]. There have been markers proposed for recognition of instruments in ultrasound images [Stol 05].

However, often techniques based on computer vision are highly application-specific and may not readily be transferred to tracking of other objects or in other environments. Due to the broadness of computer vision methods, which may be applied to intra-operative tracking, a full discussion is beyond the scope of this work.

2.5. Tracking System Benchmarking

When considering accuracy, this measure needs to be defined first: "Accuracy" is typically used as a synonym of "trueness", i.e. the expected deviation of a measurement from the true reference value:

$$\mu_e = \sum_{i=1}^{n} \frac{x_i - \hat{x}}{n}, \tag{2.1}$$

where x_i is the i-th measurement of a fiducial, and $\hat{x}$ is the fiducial's "forever unknown" [Fitz 98] true position. In contrast, "precision" (or jitter, noise, repeatability, ...) designates a measure of the spread of the samples around their mean, and the variance is an appropriate measure here:

$$\delta_e^2 = \sum_{i=1}^{n} \frac{(x_i - \bar{x})^2}{n - 1}, \qquad \text{where} \qquad \bar{x} = \sum_{i=1}^{n} \frac{x_i}{n}. \tag{2.2}$$

The distinction between accuracy (2.9a) and precision (2.9b) is visualised again in Figure 2.9. It should be noted, that while measurements in one dimension may indeed be normally distributed, *errors* definitely do not follow a normal distribution (e.g. they are always positive), and rules of thumb do not hold, e.g. equating the interval $\mu \pm 2\sigma$ with the 95% confidence interval. One measure, which combines both accuracy and precision, is the root mean square error (RMS), which is defined as

$$\epsilon_e = \sqrt{\sum_{i=1}^{n} \frac{(x_i - \hat{x})^2}{n}} \approx \sqrt{\mu_e^2 + \delta_e^2}. \tag{2.3}$$

It is a hard problem to appropriately define ground truth, since the true location of, for example, an electromagnetic (EM) tracking sensor is unknown. EM tracking measurements are often compared to optical tracking [Fran 03, Schn 07] or robotic measurements
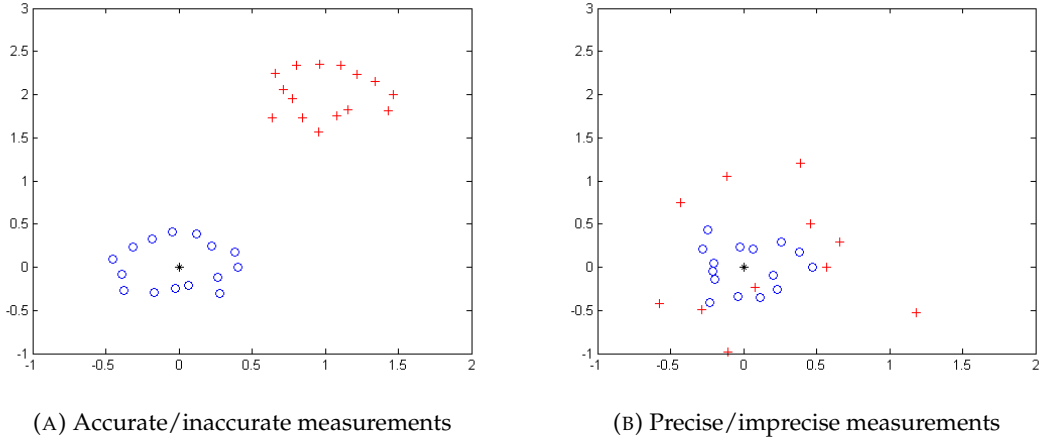
(A) Accurate/inaccurate measurements   (B) Precise/imprecise measurements

FIGURE 2.9.: **2.9a) Accurate measurements (blue circles) with low deviation from the true value (black asterisk), and inaccurate measurements (red crosses) with large deviation from the true value. 2.9b) Precise measurements (blue circles) with small spread, and imprecise measurements (red crosses) with large spread.**

[Tang 03, Gerg 12]. In some cases, precision-manufactured phantoms were used as ground truth [Humm 05, Humm 06].

In several experiments, the distances between measurements were compared to known distances [Rous 02, Humm 05, Humm 06]. However, this reduces a six-dimensional error to a single dimension, and may be less meaningful than the comparison to a reference measurement. Other consistency measures may be used as well, e.g. during pivoting [Schm 01]. In some approaches, sensors were moved across a plane [Chas 98, Schm 01, Nafi 06, Nafi 08], or moved along a planar trajectory [Humm 09]. Then, a mathematical plane was fit to the measurements and the deviation from this plane was computed. However, this only provides a 1-D measure, underestimates the actual error due to projection of ground truth to the plane of minimal error, and does not allow an assessment of orientation accuracy.

Within the scope of this thesis, we will consider transformations as rigid-body transformations with six degrees of freedom, consisting of a 3×3 rotation matrix $\mathbf{R}$ and a 3×1 translation vector $\vec{\mathbf{t}}$. Unless otherwise specified, we will use homogeneous coordinates, since this representation allows combination by matrix multiplication:

$$\mathbf{p}_D = \begin{bmatrix} x_D \\ y_D \\ z_D \\ 1 \end{bmatrix} = \begin{bmatrix} r_{11} & r_{12} & r_{13} & t_x \\ r_{21} & r_{22} & r_{23} & t_y \\ r_{31} & r_{32} & r_{33} & t_z \\ 0 & 0 & 0 & 1 \end{bmatrix} \cdot \begin{bmatrix} x_S \\ y_S \\ z_S \\ 1 \end{bmatrix} = \begin{bmatrix} \mathbf{R} & \vec{\mathbf{t}} \\ \vec{0} & 1 \end{bmatrix} \cdot \mathbf{p}_S = {}^D\mathbf{T}_S \cdot \mathbf{p}_S, \quad (2.4)$$

For simplicity, we use the norm in its non-projective meaning $\|\mathbf{p}\| := \sqrt{x^2 + y^2 + z^2}$, i.e. ignoring the last, projective component. Later, we will also use quaternions $\mathbf{q} = (q_1, q_2, q_3, q_4)$

for orientation, since they offer a compact and singularity-free representation, which lends itself better to interpolation than rotation matrices.

It is straightforward to compute a rigid transformation $^{G}\mathbf{T}_{T}$ mapping coordinates $\mathbf{p}_{T,i}$ from the tracking system to coordinates $\mathbf{p}_{G,i}$ in the ground truth coordinate frame (e.g. optical tracking), by minimising distances between ground truth coordinates and mapped coordinates:

$$\underset{^{G}\mathbf{T}_{T}}{\arg\min}\left[\frac{1}{N}\sum_{i=1}^{N}\left\|\mathbf{p}_{G,i}-{}^{G}\mathbf{T}_{T}\cdot\mathbf{p}_{T,i}\right\|^{2}\right] \qquad (2.5)$$

Such a point-based registration is often done [Fran 03, Schn 07, Shen 08, Gerg 12] for comparison to ground truth data. However, it is worth noting that this does not have a physical meaning. The underlying assumption is that both measurements were taken at exactly the same location, which they were not. However, if the relative orientation between the two measurement coordinate frames does not change, this error is a simple translation and will be contained in $^{G}\mathbf{T}_{T}$ after computation of the point-based registration. Thus, the result can be used to evaluate local skew, distortions, or noise.

When evaluating tracking systems for image-guided surgery, the final endpoint will be, whether or not a tracking system contributes to a better outcome for the patient. However, the definition of quantitative measures is a "significant challenge for medicine as a whole" [Dari 03]. In clinical routine, other factors need to be considered as well, like ease of use, additional time required for set-up and calibration, or economic impact. From an engineering point of view, there are even problems when reducing tracking accuracy to only a few numbers [Fran 04]. Thus, finding the "best" tracking systems is a highly application-specific task.

3. Calibration and Registration

For the fusion of tracking systems with intra-operative imaging devices or pre-operative imaging data, all spatial relations need to be precisely determined. In this chapter we will present methods for calibration of cameras and ultrasound imaging, temporal calibration, spatial relations via hand-eye calibration, and methods for patient registration.

Calibration is the process of measuring certain aspects of system performance. In general, the operation of a tracking system or imaging device is described by a certain model and the parameters of this model. During calibration, the device's expected operation is compared to actual measurements, and discrepancies are minimised by optimisation of these parameters [Stro 08].

3.1. Camera Calibration

Camera operation is described by the pin-hole camera model. According to this model, the projection of a point (x_w, y_w, z_w) in world coordinates to a point (x_i, y_i) in the camera image is described as

$$\begin{bmatrix} x_i \\ y_i \\ 1 \end{bmatrix} \propto \begin{bmatrix} \lambda x_i \\ \lambda y_i \\ \lambda \end{bmatrix} = \underbrace{\begin{bmatrix} K \mid \vec{0} \end{bmatrix}}_{3 \times 4 \text{ projection}} \cdot {}^{C}\mathbf{T}_W \cdot \begin{bmatrix} x_w \\ y_w \\ z_w \\ 1 \end{bmatrix}, \tag{3.1}$$

where

$$K = \begin{pmatrix} af & s & p_x \\ 0 & f & p_y \\ 0 & 0 & 1 \end{pmatrix}. \tag{3.2}$$

${}^{C}\mathbf{T}_W$ is the transformation from the world to the camera coordinate system and represents the *extrinsic parameters*. f is the camera's focal length, and a is the aspect ratio. (p_x, p_y) are the coordinates of the principal point, s is a skew factor, which is usually assumed to be zero, and λ is an arbitrary scale factor. The parameters of K are called *intrinsic parameters*.

Equation 3.1 does not yet describe radial distortion, due to spherical aberration, and tangential distortion, due to non-collinear mounting of multiple lenses. Such distortions can be severe for endoscopic systems with wide-angle optics. Thus, after projection, another non-linear mapping may be applied, in which usually two parameters each are sufficient for radial and tangential distortion [Heik 97].

For camera calibration, high-contrast patterns with known geometry are used, from which features are extracted, as shown in Figure 3.1. Usually, an estimate of the intrinsic parameters is computed first, using a closed-form solution, and then all parameters, including distortion, are optimised using an iterative technique.
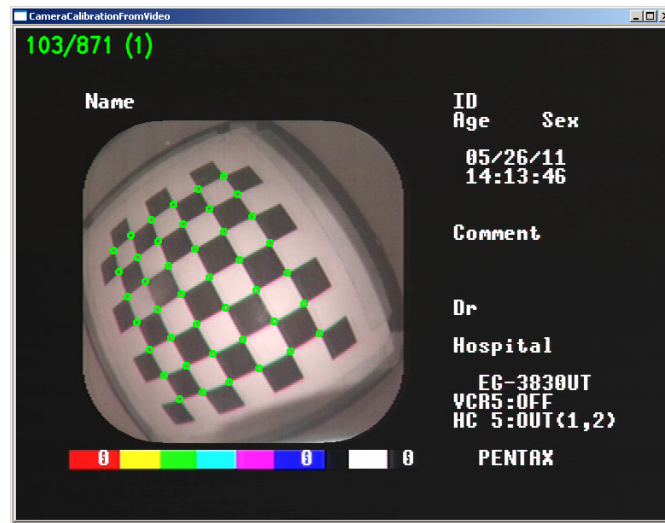
FIGURE 3.1.: **Camera calibration screenshot with segmented inner corners of calibration pattern. Please note the strong barrel distortion, or "fisheye" effect.**

Commonly used techniques have been introduced by Tsai [Tsai 87], Heikkilä [Heik 00], and Zhang [Zhan 99, Zhan 00], and calibration methods specifically for endoscopes were presented by Shahidi *et al.* [Shah 02] and by Wengert *et al.* [Weng 06].

Similar to video cameras, X-ray devices like fluoroscopes may be calibrated and tracked as well [Hofs 99, Nava 09].

3.2. Ultrasound Calibration

Ultrasound imaging may be tracked by equipping the ultrasound transducer with a positioning sensor or tracking target. Calibration determines the location of each pixel in the ultrasound image relative to the positioning sensor or tracking target.

Different approaches and phantoms have been proposed for ultrasound calibration. Approaches may be distinguished into three groups: first, detection of geometric primitives in multiple images, and determination of calibration parameters from the whole set of measurements; second, determination of the ultrasound transducer pose from a single image; and third, phantom-free approaches, where consistency between multiple acquired images is optimised.

In the first group, various geometric primitives have been proposed, which may be segmented in ultrasound images: points [Amin 01, Mura 01], points on one or more lines [Boct 03, Lind 03a, Lind 03b, Kham 05], spheres [Pago 98, Bren 04], cubes [Poon 05], and others. Usually, every image yields only limited information, e.g. in the form of a single row in a linear equation system, but given enough independent measurements (i.e. different locations, different perspectives, etc.), the equation system can be solved.

In the second group, phantoms enable an unambiguous determination of transducer pose relative to the phantom from a single image. One example of such phantoms is the Z- or N-phantom [Come 98, Pago 01, Lind 03b, Chen 06]. Multiple features are detected at once, and from distance ratios between 2-D features, the 3-D locations of these features
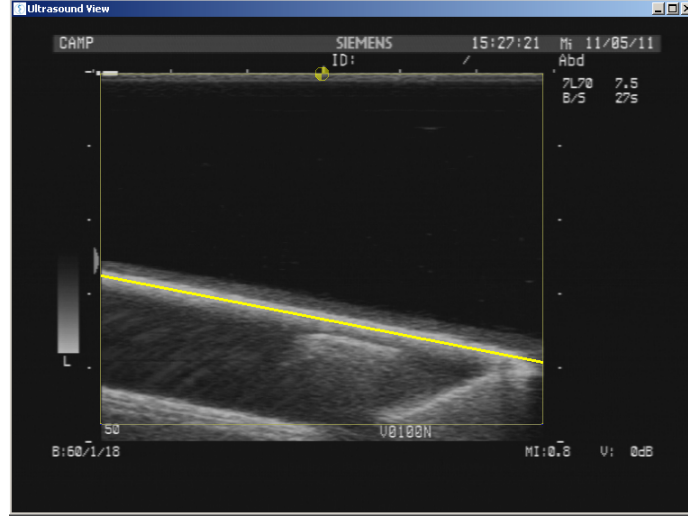
FIGURE 3.2.: **Ultrasound calibration screenshot with automatically segmented nylon membrane.**

can be computed. Given at least three 3-D features in a single image, the pose can be unambiguously determined.

In the third group, there are phantom-free image-based calibration methods, where consistency of multiple acquired images or sequences is optimised via image similarity [Blac 00, Ma 08, Wein 08].

The most simple phantom is probably used with single-wall calibration [Lang 00]: A nylon membrane, e.g. nylon stockings, is put over a planar frame and scanned in a water bath. Phantoms may be built in almost any size, and due to the knitted and quasi-rough structure, the membrane is clearly visible in ultrasound images, as shown in Figure 3.2. Pixel locations (x_U, y_U) in the ultrasound image are linearly related to physical positions (x_P, y_P) on the phantom as [Prag 98b]

$$
\begin{bmatrix} x_P \\ y_P \\ 0 \\ 1 \end{bmatrix} = \underbrace{{}^P\mathbf{T}_W}_{\text{phantom}} \cdot \underbrace{{}^W\mathbf{T}_S}_{\text{tracking}} \cdot \underbrace{{}^S\mathbf{T}_U}_{\text{calibration}} \cdot \begin{bmatrix} s_x \cdot x_U \\ s_y \cdot y_U \\ 0 \\ 1 \end{bmatrix},
\tag{3.3}
$$

where s_x and s_y are pixel scaling factors, and ${}^S\mathbf{T}_U$ is the unknown, desired transformation from the ultrasound plane to the positioning sensor or target. ${}^W\mathbf{T}_S$ is the measured transformation from the positioning sensor or target to the world coordinate frame, and ${}^P\mathbf{T}_W$ is the unknown location of the phantom plane with respect to the world coordinate frame.

There are eleven unknowns: the two scaling factors, six degrees of freedom for ${}^S\mathbf{T}_U$, and three degrees of freedom for the plane in ${}^P\mathbf{T}_W$. The zero component of equation 3.3 gives one equation in the unknown parameters. However, the line segmented in the B-scan images has two degrees of freedom, so we can write the equation for two points on this line. If the probe is then moved through all possible motions (three degrees of freedom for translation and orientation each), we have at least 12 equations, and this linear equation system can be solved using standard methods. The result for ${}^P\mathbf{T}_W$ is not needed further

FIGURE 3.3.: **Close-up picture of Olympus GF UTC140-AL5 endoscopic ultrasound probe with ultrasound transducer (U) and video camera (C). Image courtesy of Karsten Gadow.**

and can be discarded.

Originally, it was proposed to scan the bottom of a water bath. In order to avoid problems due to specular reflection, the "Cambridge phantom" was developed [Prag 98a, Prag 98b], which provides a virtual wall phantom. However, the nylon membrane phantom provides both acceptable image quality (compared to the bottom of the water bath) and simplicity of construction (compared to the Cambridge phantom).

All mentioned methods yield the transformation between the ultrasound image and the positioning sensor or tracking target, and the two-dimensional pixel size. For sterilisation and usability, compact phantoms in water-filled enclosures with attached optical tracking targets have been developed [Chen 09, Pete 10].

3.2.1. Direct Co-Calibration of Ultrasound and Video

Most endoscopic ultrasound probes also contain a video camera, as demonstrated in Figure 3.3. Since navigation by ultrasound alone is impossible in bronchoscopy, endo-bronchial ultrasound probes are guided to towards the region of interest using video. In other applications like gastroscopic examinations, ultrasound and video images are used in sequence.

If a positioning sensor is used, then both the transformations ${}^{C}\mathbf{T}_{S}$ between the tracking sensor and the camera, and ${}^{S}\mathbf{T}_{U}$ between the ultrasound transducer and the tracking sensor can be determined, as illustrated in Figure 3.4. However, if both transformations are combined to the transformation ${}^{C}\mathbf{T}_{U} = {}^{C}\mathbf{T}_{S} \cdot {}^{S}\mathbf{T}_{U}$, errors will also be accumulated. Thus, it is beneficial in terms of accuracy and robustness, to have a method for direct co-calibration of video and ultrasound [Dres 10].

A combined video-ultrasound phantom consists of an optical pattern for calibration of the video camera, and a Z-fiducial configuration of elastic rubber tubes for configuration of the ultrasound image plane, as shown in Figure 3.5. The geometric properties of the phantom can be measured using a highly accurate optical tracking system, or it may even be precision-manufactured in the future. From a single video image the transformation ${}^{C}\mathbf{T}_{P}$
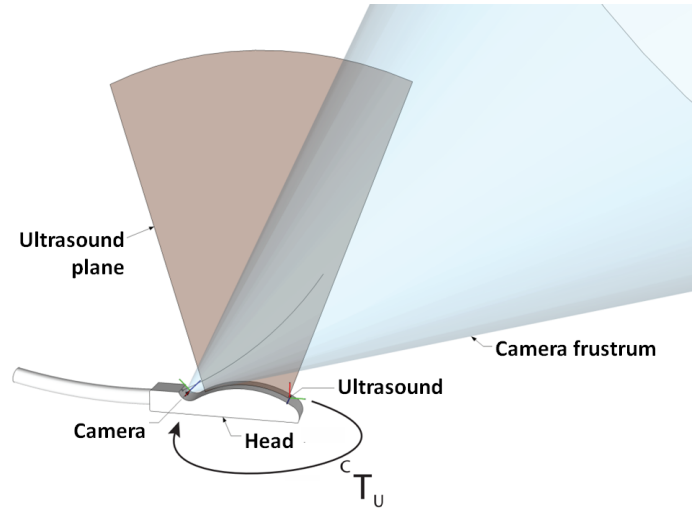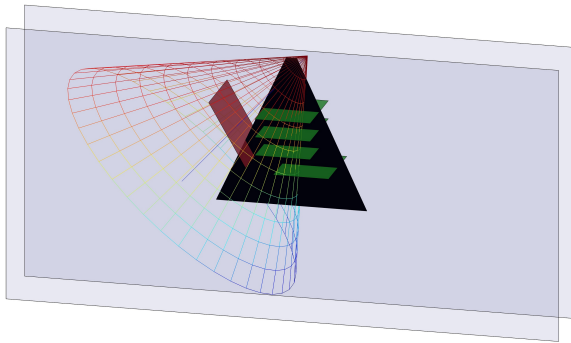
FIGURE 3.4.: **Endobronchial ultrasound system. The camera frustum and ultrasound plane are shown in their approximate spatial relation, described by the transformation $^C\mathbf{T}_U$. Image courtesy of Dressel *et al.* [Dres 10].**

(A) Phantom model
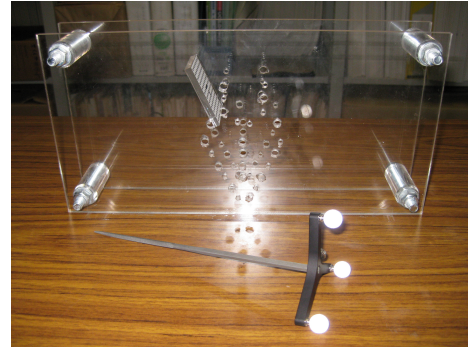
(B) Constructed phantom

FIGURE 3.5.: **Endobronchial ultrasound and video calibration phantom. 3.5a) Camera frustum (cone) and ultrasound plane (black trapezoid); planes mark Z-fiducial layers (green), optical pattern (red) and supporting structure (grey). 3.5b) Constructed phantom with optically tracked pointer; Z-fiducial tubes removed for measurements. Images courtesy of Dressel *et al.* [Dres 10].**

between the phantom and the camera can be determined, and from a single ultrasound image the transformation $^{P}\mathbf{T}_{U}$ between the ultrasound transducer and the phantom can be determined. Thus, the combined transformation $^{C}\mathbf{T}_{U} = {}^{C}\mathbf{T}_{P} \cdot {}^{P}\mathbf{T}_{U}$ can be determined without including tracking error twice. For numerical stability several pairs of images can be used.

Camera parameters change with the surrounding medium, and a submersion under water causes a magnification of the image, since the refractive index of water is different from the one of air. The intrinsic parameters need to be determined in air, since this will be the environment during application. However, for simultaneous video-ultrasound calibration underwater, the magnification needs to be compensated. Following Lavest *et al.* [Lave 00], the focal length of the camera may be adjusted by the ratio r of the refractive indices of water (1.333) and air (1.000). In order to use the distortion model with parameters determined in air, we may undo the effects of the underwater submersion (as proven sufficient by Lavest *et al.* [Lave 00]) by shrinking the image according to

$$\mathbf{p}_{a} = \alpha + \frac{\mathbf{p}_{w} - \alpha}{r} \tag{3.4}$$

where α is the camera's principal point, $\mathbf{p}_{a}$ are each point's coordinates in air, and $\mathbf{p}_{w}$ are each point's coordinates in water.

For camera pose estimation, a dot pattern [Weng 06] was printed on a decal, and the decal was attached to an acrylic glass plate. The method of Wengert *et al.* [Weng 06] was employed for determination of the camera's intrinsic parameters and $^{C}\mathbf{T}_{P}$, with adaptations in the pre-processing, in order to account for the underwater environment and the strongly inhomogeneous illumination from the endoscope's light source.

For ultrasound plane estimation, a Z-fiducial set-up similar to Comeau *et al.* [Come 98] was used. The topmost n triplets in the B-mode image correspond to the n topmost Z-fiducials. The coordinates of the intersection points are then computed in 3-D relative to the phantom, and $^{P}\mathbf{T}_{U}$ can be determined.

During calibration, the poses $^{P}\mathbf{T}_{C}$ and $^{P}\mathbf{T}_{U}$ of video camera and ultrasound transducer are computed, and their spatial relation is computed as $^{C}\mathbf{T}_{U} = {}^{P}\mathbf{T}_{C}{}^{-1} \cdot {}^{P}\mathbf{T}_{U}$. For a screen shot of the user interface during calibration, please refer to Figure 3.6.

3.3. Hand-Eye Calibration

In order to relate the camera image to other objects and, for example, provide overlays of virtual objects at the correct location within the camera image, the position of the camera centre needs to be known with respect to these objects. The same holds the other way around, if information from camera images should be used for other purposes like reconstruction. In order to track movement of the camera, it may be equipped with a position and orientation tracking system. However, the transformation between the tracked coordinate frame (tracking sensor, optical marker, robot hand, or similar) and the camera coordinate system needs to be determined. This problem originated in robotics, where this transformation has to be determined for a robot-mounted camera, and thus the process was called *hand-eye calibration* [Shiu 89, Tsai 89]. For an illustration, please refer to Figure 3.7. Hand-eye calibration can also be used to co-calibrate tracking systems in a
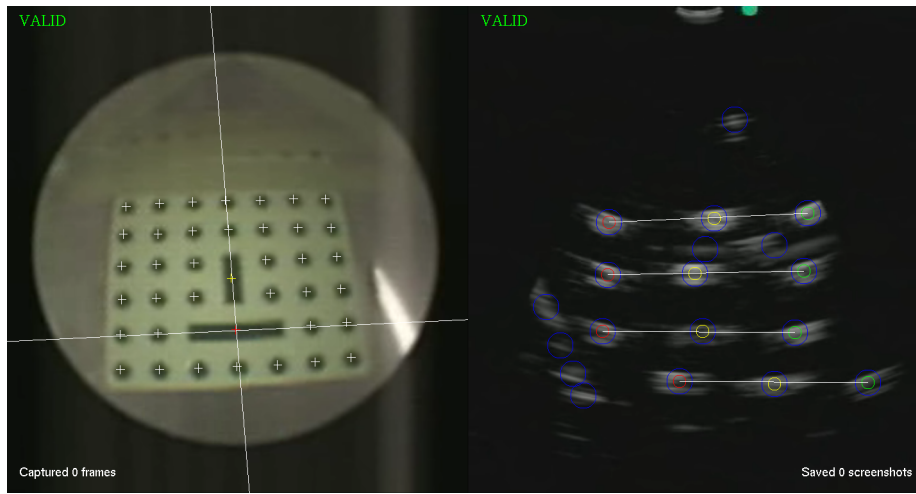
FIGURE 3.6.: **User interface during endobronchial ultrasound and video calibration, with camera image of calibration pattern (left), and ultrasound image of Z-fiducials (right). Image courtesy of Dressel *et al.* [Dres 10].**

FIGURE 3.7.: **Hand-eye calibration and fundamental relations. The robot hand performs motion A, the optical tracking target moves according to B, and the fixed, unknown relation between them is X. All three are related as $AX = XB$.**

process, which may be called "tracker alignment" [Bail 03b].

The co-calibration of electromagnetic and optical tracking systems has been proposed before [Birk 98b]. If the spatial relation between both tracking systems is fixed, t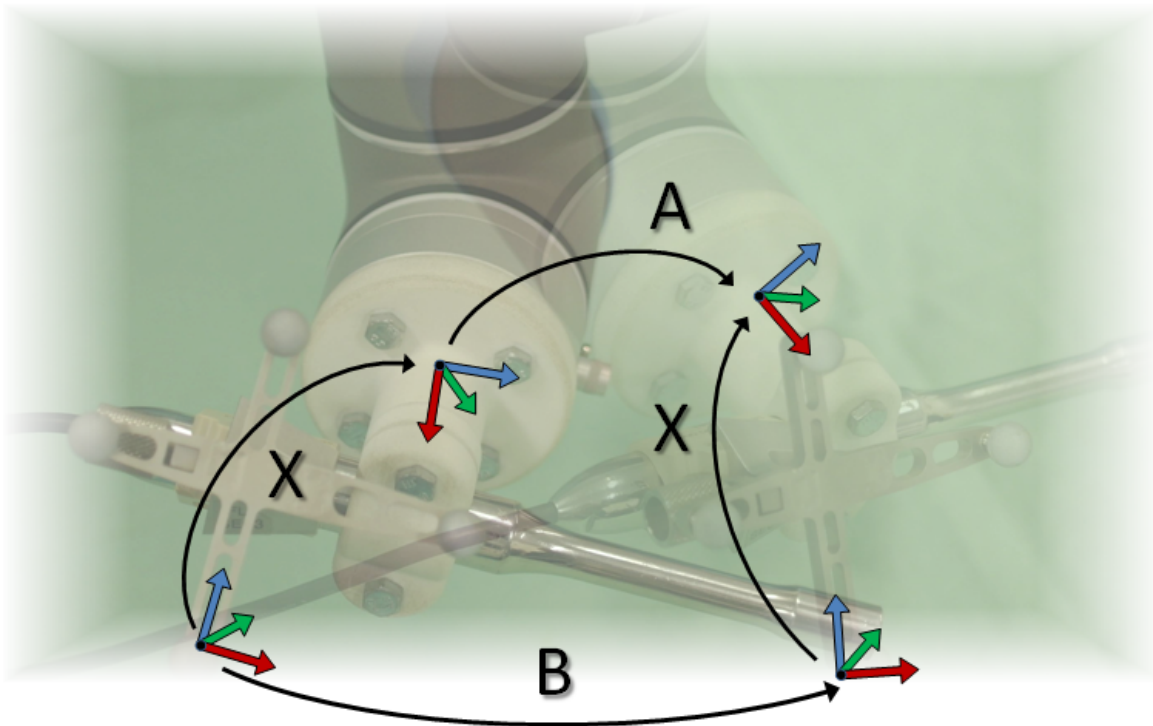hen a point-based registration may be used to relate the position measurements of both systems by a hybrid, calibrated probe, reporting the same location for both tracking systems.

For a dynamic relocation ability of the field generator, it needs to be tracked itself by optical tracking. While a co-calibration of both tracking systems is possible using a more complex point-based registration approach [Naka 00] or via precision-manufactured fixtures and divots for both tracking systems [Fisc 05a, Fisc 05b], hand-eye calibration provides a more elegant approach with fewer measurements needed. An excellent tutorial for hand-eye calibration, including tracker alignment, was provided by Martin Bauer *et al.* [Baue 04].

As shown in Figure 3.7, one motion A between two poses of the robot hand results in another motion B of the optical tracking target. These two are related to the unknown transformation X as $AX = XB$, which may be decoupled as

$$\mathbf{R}_A \cdot \mathbf{R}_X = \mathbf{R}_X \cdot \mathbf{R}_B \qquad (3.5)$$

for rotation, and

$$(\mathbf{R}_A - I)\,\vec{\mathbf{t}}_X = \mathbf{R}_X \vec{\mathbf{t}}_B - \vec{\mathbf{t}}_A \qquad (3.6)$$

for translation. At least two motions with non-parallel rotation axes are needed to solve for rotation first [Tsai 89], and then for translation. Alternative solutions for the $AX = XB$ problem have been presented, using dual quaternions [Dani 99a].

In detail, when moving an optical target using a robot, the robot hand moves between poses $\boldsymbol{H}_i$, which are described by the transformation ${}^B\mathbf{T}_H$ between the robot hand and base coordinate systems. Analogously, the poses $\boldsymbol{E}_i$ of the optical tracking target ("eye") are described by the measured transformation ${}^W\mathbf{T}_T$ from the tracking target to the optical tracking (world) coordinate system. Motions between poses i and j may be computed as

$$\boldsymbol{H}_{j\leftarrow i} = (\boldsymbol{H}_j)^{-1} \cdot \boldsymbol{H}_i \qquad \text{and} \qquad \boldsymbol{E}_{j\leftarrow i} = (\boldsymbol{E}_j)^{-1} \cdot \boldsymbol{E}_i, \qquad (3.7)$$

and then $\boldsymbol{H}_{j\leftarrow i}X = X\boldsymbol{E}_{j\leftarrow i}$ holds. This equation system can be solved for $X = {}^H\mathbf{T}_T$. Via the dual equation, where hand and eye poses are inverted, we get

$$\hat{\boldsymbol{H}}_{j\leftarrow i} = \boldsymbol{H}_j \cdot (\boldsymbol{H}_i)^{-1} \qquad \text{and} \qquad \hat{\boldsymbol{E}}_{j\leftarrow i} = \boldsymbol{E}_j \cdot (\boldsymbol{E}_i)^{-1}, \qquad (3.8)$$

and $\hat{\boldsymbol{E}}_{j\leftarrow i}Y = Y\hat{\boldsymbol{H}}_{j\leftarrow i}$ holds. Thus, the transformation $Y = {}^W\mathbf{T}_B$ between the robot base and the tracking (world) coordinate system can be determined as well. This enables e.g. the co-calibration of optical and electromagnetic tracking systems, where the electromagnetic field generator is tracked by an optical system [Feue 09]. An example of such an optically tracked electromagnetic field generator is shown in Figure 3.8.

Hand-eye calibration is applicable to any situation, where a single object is tracked by two distinct tracking systems, including cameras visually tracking a calibration pattern or other suitable imaging modalities. This method may even be applied to ultrasound calibration. The ultrasound phantom is only used for guided alignment of the ultrasound probe with several pre-defined poses, and then the transformation ${}^T\mathbf{T}_{US}$ from the ultrasound coordinate system to the tracking coordinate system is computed using an $AX = XB$ approach [Visw 04].
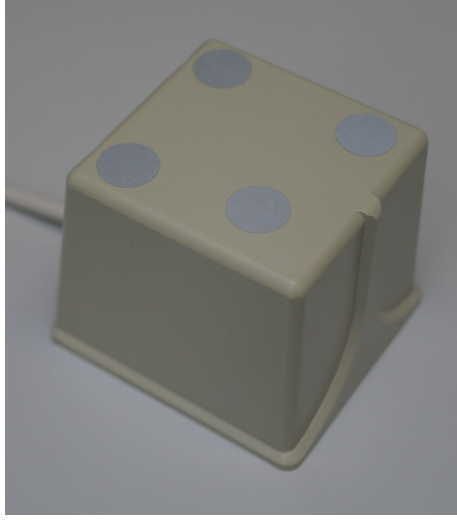
FIGURE 3.8.: **Electromagnetic tracking field generator with optical tracking markers.**

3.4. Temporal Calibration

In most cases, ultrasound or video images are formed on hardware, which is distinct from the visualisation hardware. Thus, there may be certain differences between the time of capturing the image and the time, when the image is available for further processing. We assume that this difference is constant and thus can be calibrated.

For temporal calibration, or synchronisation, a one-dimensional signal y_A and y_B is extracted from both data streams. In the case of tracking data, this may be the motion along the main direction of movement, as determined after Principal Component Analysis (PCA). In the case of image data, this may be the segmented location of certain features within the captured image, e.g. the bottom of a water bath in ultrasound images.

Thus, if the tracked object is moved back and forth along one approximately fixed direction of movement, then the one-dimensional signals from both modalities may be normalised to the range $[0, 1]$, as shown in Figure 3.9a. The correlation between the two signals, or a difference measure $\epsilon(l)$ (e.g. the mean absolute difference), may then be optimised by adjusting the latency l between both signals as

$$\epsilon(l) = \sum_t |y_A(t) - y_B(t + l)| \tag{3.9}$$

As shown in Figure 3.9b, there is a clear minimum for this difference measure. The time shift l corresponding to the minimum difference between the signals can be used to correct the timestamps, as proposed by Treece *et al.* [Tree 03].

3.5. Patient Registration

In order to relate pre-operative images, e.g. computed tomography (CT) data, to physical locations with respect to the patient in the operating room, intra-operative *image-to-physical*
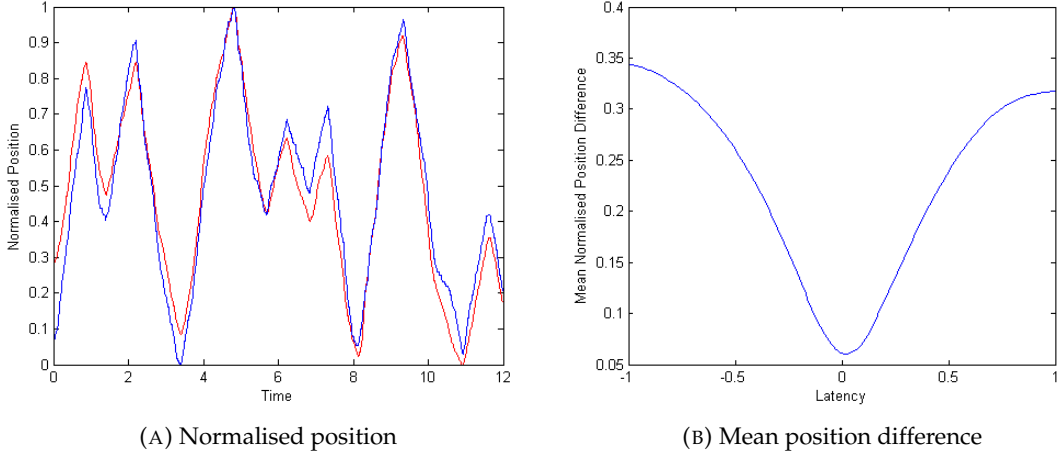
(A) Normalised position   (B) Mean position difference

FIGURE 3.9.: **Temporal alignment. 3.9a) Normalised position determined for both position measurements. 3.9b) Mean of absolute normalised position differences between both signals in relation to latency, with clear minimum.**

registration to the tracking system coordinate space is required. Therefore, a certain number of position and orientation measurements from the tracking system need to be matched to the imaging data. Due to the low amount measurements, which may reasonably be collected in the operating room, such a registration is usually rigid, i.e. no deformation is assumed.

Point-Based Registration: For point-based registration the location of a set of well-defined landmarks is determined *a priori* in the image, found again on the patient, and measured with the tracking system. These may be additional fiducials for robust, possibly automatic detection in the image, or anatomical landmarks. After the correspondences between both sets of coordinates are determined, the optimal 4×4 transformation ${}^{D}\mathbf{T}_{S}$ may be computed, which maps any 3-D point $\mathbf{p}_{S,i}$ in the source coordinate system to its corresponding 3-D point $\mathbf{p}_{D,i}$ in the destination coordinate system:

$$\operatorname*{arg\,min}_{{}^{D}\mathbf{T}_{S}} \left[\frac{1}{N} \sum_{i=1}^{N} \left\| \mathbf{p}_{D,i} - {}^{D}\mathbf{T}_{S} \cdot \mathbf{p}_{S,i} \right\|^{2} \right] \tag{3.10}$$

Given the two point sets, there are various closed-form solutions to the least-squares optimisation of the transformation ${}^{D}\mathbf{T}_{S}$, including singular value decomposition (SVD) [Arun 87, Umey 91] or eigen-decomposition [Horn 87, Horn 88, Walk 91].

Using natural landmarks is the least intrusive approach, both for patient and clinical workflow, but in certain applications landmarks may not be distinctive, or their localisation may be error-prone. External fiducials with precisely known geometry may offer superior detection up to sub-pixel accuracy, but need to be in place already for the acquisition of the pre-operative image. Until intra-operative measurement these fiducials need to remain fixed at their location, or reliable methods for precise re-positioning are required.

These markers need to be suitable for robust localisation in both the pre-operative image and with the tracking system. Many such "dual-modality" markers have been devised, including ring CT markers, which serve as printing templates for visual marks [Nico 09], CT/MRI (Magnetic Resonance Imaging) markers, which are switched to localisation divots intra-operatively [Maur 97], or the visual detection of CT markers [Feue 08a].

Shape-Based Registration: In certain applications it may be impractical to precisely define and intra-operatively localise natural landmarks, or impossible to include additional fiducials *a priori* for pre-operative imaging. Therefore, intra-operative data may be acquired *a posteriori* without explicit point correspondence to the imaging data. Volumetric approaches are usually impractical in the operating room, which leaves surface-based approaches as the dominant solution.

Surfaces may be extracted from pre-operative data, using algorithms like "marching cubes" [Lore 87]. Intra-operatively, surfaces may be acquired with tracked probes or pointers, various types of laser scanners, depth imaging via structured light, or depth cameras.

Since point correspondences are unknown, many approaches employ the Iterative Closest Point (ICP) algorithm [Besl 92] or variants thereof [Maur 98, Degu 07]. Application-specific distance measures are also used. For example, in bronchoscopy, it is known that the bronchoscope moves only within the airways. Thus, the spatial relation of a recorded trajectory through the airways may be optimised with respect to a segmentation of the airways [Klei 07, Feue 10].

With such approaches, there is usually more data available than with the localisation of only few landmarks, and errors may be minimised further.

4. Hybrid Tracking

Hybrid tracking systems may be used to overcome limitations of single tracking systems, and leverage their advantages. We focus on optimisation of electromagnetic tracking accuracy, since this is the dominant technology for the tracking of flexible instruments within the human body.

For example, combined optical and electromagnetic tracking may use either tracking modality in case of dysfunctions like obstructed line of sight for optical tracking or metallic distortions for electromagnetic tracking [Birk 98b, Hans 98]. Alternatively, in the case of distortions of the electromagnetic tracking field, the field generator may be relocated freely [Naka 00, Fran 11]. However, the real power of hybrid tracking systems is not just the availability of multiple options, or the chaining of tracking systems, but the use of redundant information for error detection and correction.

4.1. Redundant Tracking for Reliability

An important quality of a tracking system is reliability or robustness, and due to the safety requirements in a clinical setting this may be even more important than accuracy. Redundant tracking information can be modelled for detection and correction of dynamic, transient errors of electromagnetic tracking systems.

Reliability is improved, when errors can be compensated for. If no error compensation is possible, an appropriate warning to the users is needed, in order not to rely on erroneous tracking information. For error detection, the consistency between multiple pose estimates can be monitored during tracking, and checked against a pre-defined threshold. For error compensation, there are various ways to fuse multiple pose estimates.

Tracking uncertainty may be described through the covariances of the tracking data, which contains for all pairs of dimensions i and j both the standard deviations σ_i and σ_j and the correlation $\rho_{i,j}$ of measurements in dimensions i and j:

$$\Sigma_{ij} = \text{cov}(X_i, X_j) = \text{E}\left[(X_i - \mu_i)(X_j - \mu_j)\right] = \sigma_i \cdot \sigma_j \cdot \rho_{i,j} \tag{4.1}$$

Then multiple estimates may be combined using a weighted sum, where weights are determined by the covariance matrices of each tracking estimate [Hoff 00]. Alternatively, multiple estimates may be fused by filtering, e.g. Kalman filters [Kalm 60], or particle filters [Arul 02]. Finally, consistency of multiple estimates can be optimised numerically, i.e. minimising the discrepancy from all estimates simultaneously. This approach is the most flexible, since arbitrary cost functions may be used for optimisations.

Laparoscopic Ultrasound: As an example for both error detection and correction using redundant tracking, we are going to present a laparoscopic ultrasound transducer with a flexible tip, which is tracked by both optical and electromagnetic tracking. The proximal part of the instrument, i.e. the shaft, remains outside the patient body during surgery and may be tracked using an optical system. The distal part, however, i.e. the tip with the ultrasound transducer, is inside the patient, and there is a flexible region next to the tip. Thus, the tip needs to be separately tracked by an electromagnetic system. Redundant, complementary tracking information enables tracking error detection and error correction.

An important property of the flexible tip is that its motion can almost completely be described by two degrees of freedom. Two levers at the shaft are used to bend the tip in the up-down or left-right directions. In addition, the tip yields to external forces, but this again is constrained by limited flexibility in the bending region. Thus, position measurements for both parts of the ultrasound probe are correlated and contain redundant information.

Laparoscopic ultrasound is valuable, e.g. for the staging of hepatic cancer, gallbladder and bile duct tumours, as well as pancreatic tumours [Rau 02, Gang 06, Jaki 06]. However, due to the small field of view and indirect handling of the laparoscopic transducer through a pivot point, it is difficult to mentally align the ultrasound plane to patient anatomy, in particular for novices. Also, the tip of the ultrasound probe needs to be constantly monitored using laparoscopic video, since looking at the ultrasound image alone may cause inadvertent injury to the patient [Gang 06]. Since video images are already used for navigation, one possible assistance to surgeons is overlaying the current ultrasound image onto the video image, in order to visualise the spatial relation to patient anatomy [Hild 08, Lang 08, Solb 09]. For correct overlay, accurate tracking of the ultrasound transducer tip within the patient body is mandatory and needs to consider the flexibility of the tip as well as the possibility of adverse influences.

Hardware Set-up: We use a flexible laparoscopic LAP8-4 linear array transducer (5 MHz, 10 mm diameter) with a Sonoline Omnia ultrasound system (Siemens Medical Solutions, Mountain View, CA, USA), a laparoscopic camera with a forward-oblique 30° HOPKINS telescope (Karl Storz, Tuttlingen, Germany), an optical tracking system (ARTtrack2, Advanced Realtime Tracking, Weilheim, Germany), and an electromagnetic tracking system (3D Guidance, Ascension Technology, Burlington, VT, USA) with a mid-range field generator and 1.3 mm sensors with vinyl tubing, which have a total diameter of 1.7 mm. Temporal synchronisation of all data streams and visualisation were provided by our medical augmented reality software framework CAMPAR [Siel 06]. The full set-up is presented in Figure 4.1a.

The laparoscopic ultrasound probe is tracked using both the optical and the electromagnetic tracking systems. Intra-operatively, part of the shaft of the probe remains outside the patient and can thus be tracked by the optical tracking (OT) system. However, since the ultrasound probe features a flexible bending region, optical tracking is not sufficient for tracking of the probe tip inside the patient. Two electromagnetic (EM) tracking sensors were fixed to the probe both proximal and distal of the bending region, with a distance of approximately 7 cm (cf. Figure 4.1b). Since there are now two tracking systems for the rigid probe shaft, OT and EM tracking, the redundant tracking information may be used to detect and correct tracking errors, e.g. from distortions of the EM field. Additionally, for
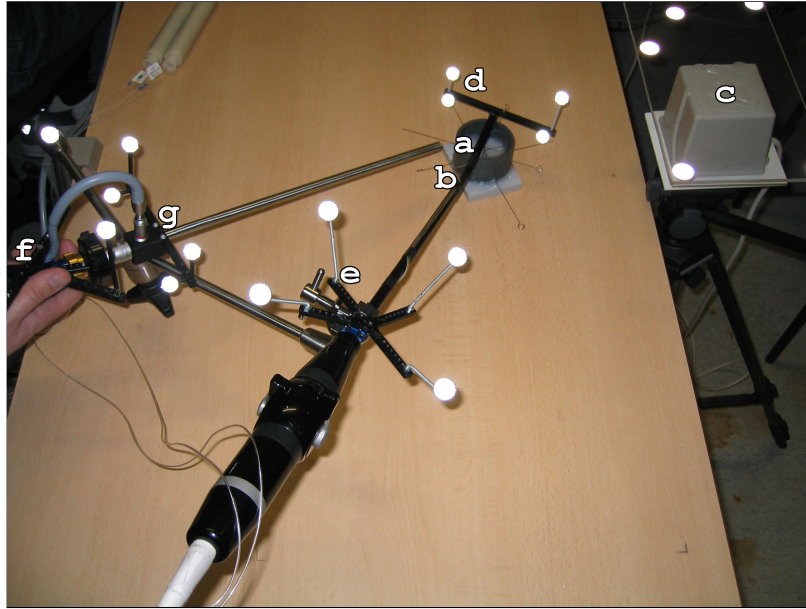
(A) System set-up

(B) Transducer tip close-up

FIGURE 4.1.: **System set-up used for laparoscopic ultrasound tracking. 4.1a) Two magnetic tracking sensors were attached to the laparoscopic ultrasound transducer, one to the flexible tip (a) and to the rigid shaft (b). The magnetic tracking field generator (c) is tracked by an optical tracking system. Two optical tracking targets are attached to the ultrasound transducer, one (for evaluation only) to the flexible tip (d) and another target to the rigid shaft (e). Additionally, the laparoscope (f) and its telescope (g) are tracked by an optical tracking system. 4.1b) Close-up of (a) and (b).**
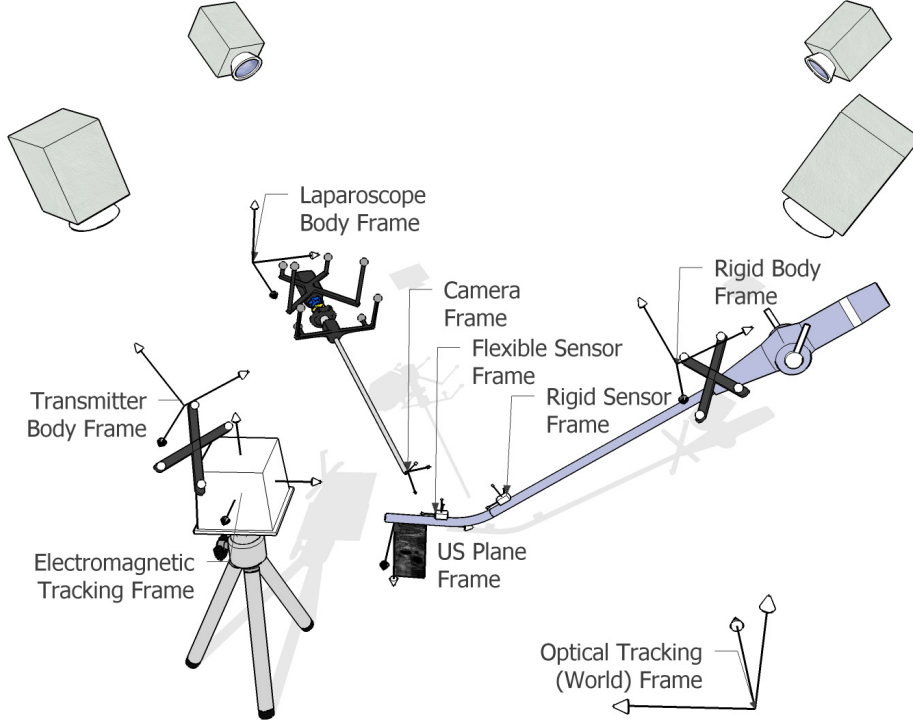
FIGURE 4.2.: **Coordinate frames in laparoscope tracking set-up.**

co-registration of both tracking systems, an OT target was fixed to the EM field generator, and two more targets were fixed to the laparoscope – one target on the laparoscope head, and one target on the telescope, in order to account for rotations of the telescope. For an overview of all tracked objects and coordinate systems involved, please refer to Figure 4.2.

Due to the multitude of coordinate systems involved in the rest of this section, we will shortly clarify the notation used for transformations: Electromagnetic tracking sensors will be denoted "magnetic sensors" (MS), optical tracking targets will be denoted "optical markers" (OM).

Laparoscopic Camera Calibration: For calibration of the intrinsic and extrinsic parameters of the laparoscopic camera, standard methods are used (cf. section 3.1). Among other parameters, the transformation $^{OM_{lap}}\mathbf{T}_C$ from the camera centre coordinate system to the optical tracking target on the camera head is obtained.

For calibration of the forward-oblique scope rotation, the method presented by Yamaguchi *et al.* [Yama 04] was used. However, instead of a rotary encoder a second optical tracking target was used, and the relative orientation of both tracking targets was measured, as proposed by De Buck *et al.* [De B 07]. For a more detailed description of this calibration step in our set-up, please see Feuerstein *et al.* [Feue 08a].

Laparoscopic Ultrasound Calibration: We need to estimate the pixel scaling of the ultrasound scan plane, and the spatial location of the ultrasound scan plane relative to the EM tracking sensor at the probe tip, i.e. the transformation $^{MS_{tip}}\mathbf{T}_{US}$. Single-wall ultrasound

calibration was performed as described in section 3.2.

Tracking Systems Co-Registration: For co-registration of the two tracking system coordinate frames hand-eye calibration was performed as outlined in section 3.3.

We need to determine the spatial relationships between the EM field generator and its OT target. Using such an OT target on the EM field generator allows re-location of the field generator, in contrast to the method by Birkfellner *et al.* [Birk 98b]. Also, the spatial relation between the OT target on the ultrasound probe shaft and the EM sensor proximal of the bending region needs to be determined, which is fixed relative to the OT target.

The laparoscopic ultrasound probe is moved to at least four poses, and at each pose, measurements from both the electromagnetic as well as the optical tracking system were recorded: the transformation $^{\mathrm{EMT}}\mathbf{T}_{\mathrm{MS_{shaft}}}$ from the magnetic sensor (MS) at the shaft to the EM tracking system (EMT), and the transformation $^{\mathrm{OT}}\mathbf{T}_{\mathrm{OM_{shaft}}}$ from the optical tracking target (OM) at the shaft to the optical tracking system (OT).

For all pairs of stations k and l the motion of the optical tracking target

$$\mathbf{T}_{\mathrm{OM_{shaft}}(l\leftarrow k)} = {}^{\mathrm{OM_{shaft}}(l)}\mathbf{T}_{\mathrm{OT}} \cdot {}^{\mathrm{OT}}\mathbf{T}_{\mathrm{OM_{shaft}}(k)} = \left({}^{\mathrm{OT}}\mathbf{T}_{\mathrm{OM_{shaft}}(l)}\right)^{-1} \cdot {}^{\mathrm{OT}}\mathbf{T}_{\mathrm{OM_{shaft}}(k)} \qquad (4.2)$$

was computed, as well as the motion of the electromagnetic tracking sensor

$$\mathbf{T}_{\mathrm{MS_{shaft}}(l\leftarrow k)} = {}^{\mathrm{MS_{shaft}}(l)}\mathbf{T}_{\mathrm{EMT}} \cdot {}^{\mathrm{EMT}}\mathbf{T}_{\mathrm{MS_{shaft}}(k)} = \left({}^{\mathrm{EMT}}\mathbf{T}_{\mathrm{MS_{shaft}}(l)}\right)^{-1} \cdot {}^{\mathrm{EMT}}\mathbf{T}_{\mathrm{MS_{shaft}}(k)}. \qquad (4.3)$$

For all pairs of stations then,

$$\underbrace{\mathbf{T}_{\mathrm{OM_{shaft}}(l\leftarrow k)}}_{A} \cdot \underbrace{{}^{OM_{\mathrm{shaft}}}\mathbf{T}_{\mathrm{MS_{shaft}}}}_{X} = \underbrace{{}^{OM_{\mathrm{shaft}}}\mathbf{T}_{\mathrm{MS_{shaft}}}}_{X} \cdot \underbrace{\mathbf{T}_{\mathrm{MS_{shaft}}(l\leftarrow k)}}_{B} \qquad (4.4)$$

holds, i.e. $AX = XB$ (cf. Figure 4.3).

By suitably switching the input transformations, the transformation $^{\mathrm{EMT}}\mathbf{T}_{\mathrm{OM_{EMT}}}$ from the optical tracking target on the EM tracking field generator to the EM tracking coordinate system can be computed from the same data. Further details can be found in our previous work [Reic 07], including a derivation of the exact transformations used.

In an additional numerical optimisation step using the Levenberg-Marquardt method [Leve 44], the results of the closed-form solution [Dani 99a] for $^{\mathrm{EMT}}\mathbf{T}_{\mathrm{OM_{EMT}}}$ and $^{\mathrm{OM_{shaft}}}\mathbf{T}_{\mathrm{MS_{shaft}}}$ were further improved. For all recorded poses the error measure

$$\mathbf{T}_\delta = {}^{\mathrm{MS_{shaft}}}\mathbf{T}_{\mathrm{EMT}} \cdot {}^{\mathrm{EMT}}\mathbf{T}_{\mathrm{OM_{EMT}}} \cdot {}^{\mathrm{OM_{EMT}}}\mathbf{T}_{\mathrm{OT}} \cdot {}^{\mathrm{OT}}\mathbf{T}_{\mathrm{OM_{shaft}}} \cdot {}^{\mathrm{OM_{shaft}}}\mathbf{T}_{\mathrm{MS_{shaft}}} \qquad (4.5)$$

was optimised. This corresponds to a closed loop from shaft EM sensor to shaft OT target, to the OT coordinate system, to the EM field generator OT target, to the EM tracking coordinate system, and to the shaft EM sensor – ideally, this would yield an identity transform, and thus the difference from identity corresponds to the accumulated tracking and calibration errors.

The combined translation and rotation error δ was computed with a weighting of 1:3 of translation errors in millimetres and rotation errors in degrees. This ratio was derived from the stated accuracy of the tracking systems, as provided independently by both manufacturers, i.e. 0.4 mm and 0.12° for the OT system, and 1.4 mm and 0.5° for the EM tracking
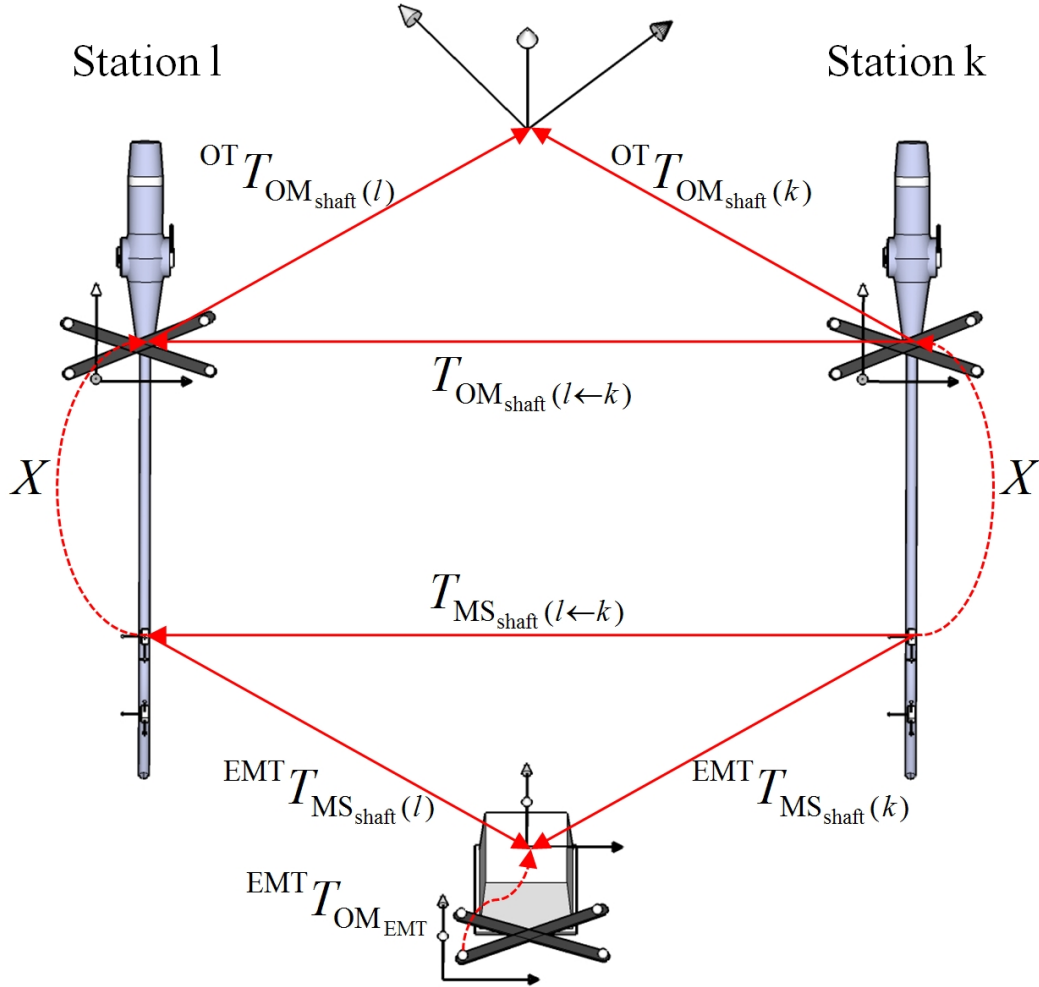
FIGURE 4.3.: **Hand-eye calibration for magneto-optic tracking systems co-calibration. We compute the unknown transformations X and $^{\text{EMT}}\text{T}_{\text{OM}_{\text{EMT}}}$ (dashed lines). For multiple transducer poses (two poses k and l shown here), the motions $\text{T}_{\text{OM}_{\text{shaft}}(l\leftarrow k)}$ and $\text{T}_{\text{MS}_{\text{shaft}}(l\leftarrow k)}$ of the optical marker and the magnetic sensor are computed. From these motion pairs, we can generate an overdetermined system of linear equations to solve for both desired transformations. Image courtesy of Feuerstein *et al.* [Feue 09].**

system. As additional reasoning for this weighting, when we have information about the noise levels in both position and translation (i.e. the standard deviations σ_t and σ_θ), then in joint distance measures for 6-D poses, the scaling of translation and rotation can be set to $\lambda = \sigma_t/\sigma_\theta$ [Penn 98].

Since we have a good initial estimate, run-time of the numerical optimisation is negligible. The maximum error δ_{max} after optimisation over all poses was used as quality estimate for the calibration.

4.1.1. Redundancy Modelling

The limited motion of the ultrasound transducer tip and the redundant tracking information can be captured in a model of the physical motion of the tip, i.e. of the behaviour of the bending region. This enables electromagnetic tracking error detection and correction.

Transducer Axes Calibration: The most basic parameters of the probe geometry are the axis of the transducer shaft and the axis of the transducer tip.

Each axis is described by one 3-D base point $\mathbf{b}$, and one unit direction vector $\vec{\mathbf{d}}$. Both of them may be determined using the same method: A tightly fitting plastic cylinder was constructed, with an additional electromagnetic (EM) tracking sensor in one end. This cylinder is put over the probe tip and rotated by 360 degrees, flipped, and rotated again, as demonstrated in Figure 4.4. During each rotation, the trajectory of the additional EM tracking sensor is recorded with respect to the EM tracking sensor fixed to the probe tip. The complete point cloud $\mathbf{p}_{i=1...n}$ is then fitted to a cylinder with radius r around the transducer axis, defined by $\mathbf{b}$ and $\vec{\mathbf{d}}$. The following cost is minimised:

$$\sum_{i=1}^{n} \left| r - \left\| \vec{\mathbf{d}} \times (\mathbf{b} - \mathbf{p}_i) \right\| \right| \tag{4.6}$$

After optimisation, $\mathbf{b}$ is normalised to be the point on the axis closest to the EM tracking sensor on the probe tip. The calibration of the probe shaft axis is performed analogously.

Probe Tip Motion Model: The relative position and orientation between the two electromagnetic (EM) tracking sensors next to the bending region can be measured with six degrees of freedom. However, since the probe tip has only two degrees of freedom corresponding to the two steering levers, the redundancy contained in the additional four degrees of freedom may be used for error detection and correction.

The probe tip does not bend at a single joint, but instead has a bending region with multiple links over approximately three centimetres, similar to the structure shown in Figure 4.5. The two levers may be put into seven different positions each, yielding a total of 49 user selectable combinations. However, since the tip can also yield to external force or gravity, we chose a continuous surface to represent all possible poses of the probe tip. All links may be assumed to be bent by the same angle.

So far the model only describes the bending region, and for connection to the EM tracking sensors more transformations are needed. In total, a chain of transformations is used, as shown in Figure 4.6. First, the coordinate frame of the EM tracking sensor at the probe tip is transformed into the "link frame" by $^{\text{Link}}\mathbf{T}_{\text{MS}_{\text{tip}}}$. Since the precise mounting of the
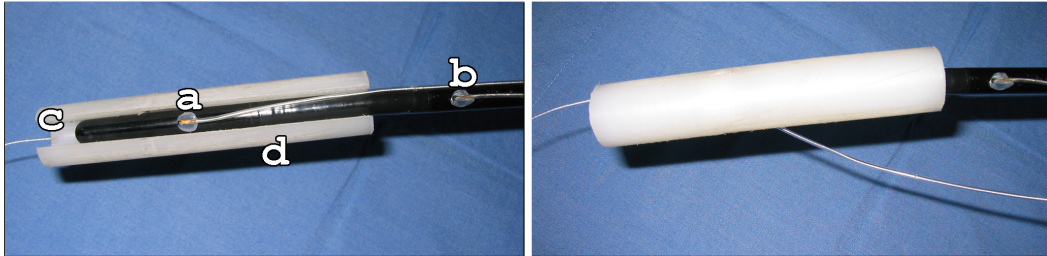
FIGURE 4.4.: **Transducer axis calibration. The transducer axis is calibrated both in relation to the local coordinate system of the magnetic sensor attached to the tip (a) and, in a second step not shown here, in relation to the coordinate system of the magnetic sensor on the shaft (b). To do this, a plastic cylinder (d) is put over the transducer tip with an additionally attached sensor (c) on the left end. The plastic cylinder is rotated at least 360 degrees, flipped, and rotated another 360 degrees or more.**
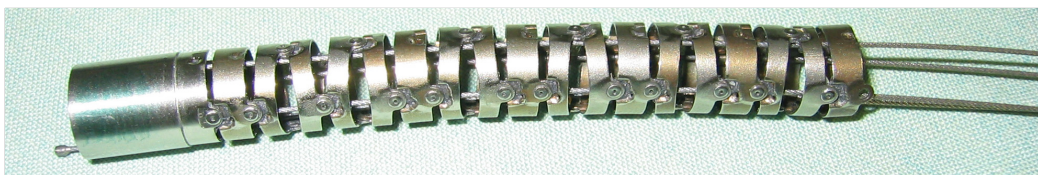
FIGURE 4.5.: **Typical bending region of endoscopic instruments. Four Bowden cables are pairwise and alternately connected to every second link of the bending region. They are often controlled by steering levers, where each pair of cables is connected to the same lever.**
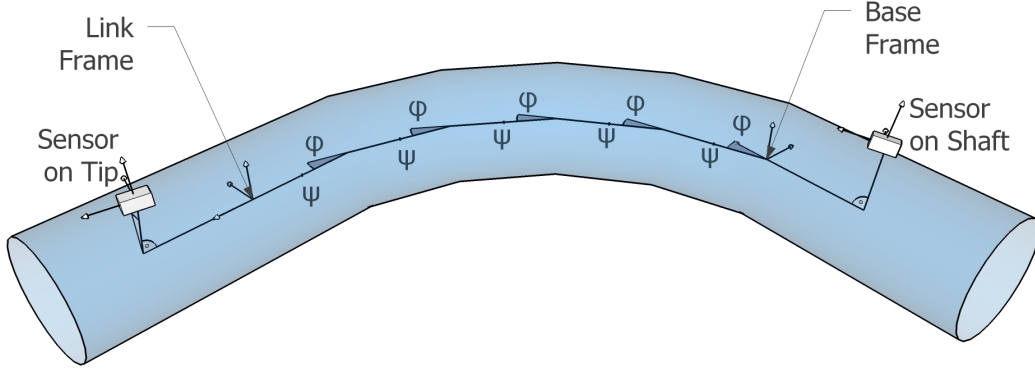
FIGURE 4.6.: **Mathematical model of flexible ultrasound probe tip – only the rotation ϕ about the x axis is visualised here, the rotation ψ about the y axis is zero.**

sensor with respect to the probe tip is unknown, this transformation has full six degrees of freedom, some parameters of which are initialised from the tip calibration.

Then n links follow, with links alternately rotating by ψ about the y axis or by ϕ about the x axis. No rotation about the z axis is assumed, and each link incorporates a small translation t_z along the z axis. Thus, $^{\mathrm{Base}}\mathbf{T}_{\mathrm{Link}}$ in total has four degrees of freedom: ψ, ϕ, t_z, and the number of links n. The alternating rotation about the x and y axes was derived from the real structure of the bending region (cf. Figure 4.5), where four Bowden cables are connected to the steering levers, and are pairwise and alternately connected to every second link. At the end of the bending region, another transformation $^{\mathrm{MS_{shaft}}}\mathbf{T}_{\mathrm{Base}}$ transforms the base coordinate frame to the EM tracking sensor at the probe shaft, some parameters of which are again initialised from the tip calibration.

The full transformation chain of the motion model is (cf. Figure 4.6)

$$^{\mathrm{MS_{shaft}}}\mathbf{T}_{\mathrm{MS_{tip}}} = {}^{\mathrm{MS_{shaft}}}\mathbf{T}_{\mathrm{Base}} \cdot {}^{\mathrm{Base}}\mathbf{T}_{\mathrm{Link}} \cdot {}^{\mathrm{Link}}\mathbf{T}_{\mathrm{MS_{tip}}} \tag{4.7}$$

where

$$^{\mathrm{Base}}\mathbf{T}_{\mathrm{Link}} = \underbrace{\mathbf{T}_{\mathrm{Link}}(\phi)}_{1} \cdot \underbrace{\mathbf{T}_{\mathrm{Link}}(\psi)}_{2} \cdot \underbrace{\mathbf{T}_{\mathrm{Link}}(\phi)}_{3} \cdot \ldots \tag{4.8}$$

$$\underbrace{\qquad\qquad\qquad\qquad\qquad}_{n \text{ times}}$$

and

$$\mathbf{T}_{\mathrm{Link}}(\phi) = \begin{pmatrix} 1 & 0 & 0 & 0 \\ 0 & \cos(\phi) & -\sin(\phi) & 0 \\ 0 & \sin(\phi) & \cos(\phi) & t_z \\ 0 & 0 & 0 & 1 \end{pmatrix} \tag{4.9}$$

$$\mathbf{T}_{\mathrm{Link}}(\psi) = \begin{pmatrix} \cos(\psi) & 0 & \sin(\psi) & 0 \\ 0 & 1 & 0 & 0 \\ -\sin(\psi) & 0 & \cos(\psi) & t_z \\ 0 & 0 & 0 & 1 \end{pmatrix} \tag{4.10}$$

The probe tip motion model is actually anchored at the probe shaft OT target by adding the (static) transformation $^{\mathrm{OM_{shaft}}}\mathbf{T}_{\mathrm{MS_{shaft}}}$ as

$$^{\mathrm{OM_{shaft}}}\mathbf{T}_{\mathrm{MS_{tip}}} = {}^{\mathrm{OM_{shaft}}}\mathbf{T}_{\mathrm{MS_{shaft}}} \cdot {}^{\mathrm{MS_{shaft}}}\mathbf{T}_{\mathrm{MS_{tip}}} \tag{4.11}$$

Due to anchoring at the OT target instead of the EM sensor, the model is not influenced by any distortions of the EM tracking field, and only static parameters are needed for optimisation of the two bending angles ϕ and ψ.

4.1.2. Error Detection and Correction

Electromagnetic (EM) tracking errors can be detected using discrepancies between the optical and EM tracking systems. The probe tip motion model enables real-time tracking error detection and correction with high sensitivity and specificity.

After calibration, we know the fixed transformations $^{OM_{shaft}}\mathbf{T}_{MS_{shaft}}$ from the EM tracking sensor (MS) at the shaft to the optical tracking target (OM) at the shaft, and $^{EMT}\mathbf{T}_{OM_{EMT}}$ from the optical tracking target at the EM tracking field generator to the EM tracking coordinate system. In a first approach we use the redundancy between the EM and optical tracking systems for error detection and correction in a *tracking redundancy-based* approach.

After modelling the motion of the ultrasound probe bending region, in a second approach we employ the redundancy between both EM tracking sensors in a *model-based* approach.

Tracking Redundancy-Based Error Detection: Intra-operatively, the tracking error for the EM sensor mounted at the probe shaft is estimated using equation 4.5 (page 37). This estimate largely depends on EM tracking error, since OT is more accurate and robust. If the tracking error is bigger than a pre-defined threshold, e.g. δ_{max} from calibration, then surgical staff is automatically warned. Such errors may be due to quick movement and tracking artefacts, or static or dynamic distortions of the EM field.

This is similar to the approach of Birkfellner *et al.* [Birk 98a] and Mucha *et al.* [Much 06], who use two EM tracking sensors mounted in a rigid configuration. Deviations of their distance (or their relative orientation) from the previously determined true distance indicate distortions of the magnetic field. However, this assumes that both sensors are affected differently, and that this difference correlates with actual error. In our set-up, we do not use two EM sensors, but one EM sensor and an optical tracking system, both attached to the probe shaft. Thus, we are able to detect any kind of distortion of the EM field.

Tracking Redundancy-Based Error Correction: Every approach to correction of static distortions of the EM tracking field, which is based on hybrid (and thus redundant) tracking [Naka 00] may be used to detect tracking errors. However, magneto-optical tracking alone is not applicable to the tip of the laparoscopic ultrasound probe due to the missing line of sight and the flexible bending region.

A reference pose of the EM tracking sensor mounted at the probe shaft is computed from the current optical tracking (OT) measurement $^{OT}\mathbf{T}_{OM_{shaft}}$, and from the transformation $^{OM_{shaft}}\mathbf{T}_{MS_{shaft}}$, determined through hand-eye calibration, as

$$^{OT}\mathbf{T}_{MS_{shaft}(calib)} = {}^{OT}\mathbf{T}_{OM_{shaft}} \cdot {}^{OM_{shaft}}\mathbf{T}_{MS_{shaft}} \tag{4.12}$$

The current pose of the EM tracking sensor is computed from the current EM tracking measurement, and from the transformation $^{EMT}\mathbf{T}_{OM_{EMT}}$, determined through tracker align-

ment, as

$$^{OT}\mathbf{T}_{MS_{shaft}(meas)} = {}^{OT}\mathbf{T}_{OM_{EMT}} \cdot \left({}^{EMT}\mathbf{T}_{OM_{EMT}}\right)^{-1} \cdot {}^{EMT}\mathbf{T}_{MS_{shaft}} \tag{4.13}$$

Then, the deviation may be inverted and applied to the pose analogously measured for the EM tracking sensor at the probe tip:

$$^{OT}\mathbf{R}_{MS_{tip}(corr)} = \left({}^{OT}\mathbf{R}_{MS_{shaft}(meas)}\right)^{-1} \cdot {}^{OT}\mathbf{R}_{MS_{shaft}(calib)} \cdot {}^{OT}\mathbf{R}_{MS_{tip}(meas)} \tag{4.14}$$

$$^{OT}\vec{\mathbf{t}}_{MS_{tip}(corr)} = -{}^{OT}\vec{\mathbf{t}}_{MS_{shaft}(meas)} + {}^{OT}\vec{\mathbf{t}}_{MS_{shaft}(calib)} + {}^{OT}\vec{\mathbf{t}}_{MS_{tip}(meas)} \tag{4.15}$$

However, distortions of the EM field are complex and may not be shift invariant, i.e. the two sensors are likely to be affected differently by the distortion, even when placed close to each other. This is the reasoning behind the error detection approach by Birkfellner *et al.* [Birk 98a] and Mucha *et al.* [Much 06], and this necessitates more sophisticated error detection and correction methods.

Motion Model-Based Error Detection: We have modelled the possible movement of the EM tracking sensor mounted at the probe tip, with respect to the OT target mounted at the probe shaft. Now we use this model for error detection. Intra-operatively, the two degrees of freedom ϕ and ψ of the model are optimised in order to yield the closest possible pose to the current EM tracking measurement (cf. equation 4.7 on page 41). Due to the low number of degrees of freedom, this optimisation is possible in real-time. As long as there are no distortions of the EM tracking field, there will be a solution close to the currently measured pose. If there are distortions of the EM tracking field, there will likely be inconsistencies and the model cannot be fully matched to the current measurements.

If the discrepancy between the optimised pose and the real pose is greater than a predefined threshold, surgical staff is automatically warned. Since the measured pose relative to the OT target at the shaft has six degrees of freedom, whereas the model only has two, we can use the redundancy contained in the remaining four degrees of freedom, in order to detect inconsistencies.

Motion Model-Based Error Correction: For error correction, we simply use the result of the optimisation step mentioned above instead of the EM sensor tracking measurement, i.e. we use the pose compliant to the possible probe tip movement, and closest to the current, distorted EM sensor measurement.

Evaluation of Error Detection: For evaluation, we attach a temporary optical tracking target to the tip of the laparoscopic ultrasound transducer (cf. Figure 4.1 on page 35). Then we determine the transformation $^{OM_{tip}}\mathbf{T}_{MS_{tip}}$ between the EM tracking sensor at the tip and this additional optical tracking target. Thus, we are able to compute a reference pose for this EM sensor via optical tracking.

For error detection, a "distrust value" can be computed via different approaches and checked against a threshold – either via the redundancy-based approach, or via the model-based approach. Two types of error are then possible: Tracking may actually be erroneous,

while being predicted as correct (false-negative), or tracking may be correct, while being predicted as erroneous (false-positive).

There is a trade-off between both types of errors, which is determined by the threshold for prediction. For any given threshold, the sensitivity and specificity of the prediction can be determined, i.e. the robustness against false-negative errors and false-positive errors. However, instead of picking only a few specific thresholds for evaluation, we compute the Receiver Operating Characteristic (ROC) curves (Figure 4.7), which contain complete information about this trade-off.

Each point on the curve represents the performance of a certain threshold, i.e. sensitivity and specificity. We considered the value with maximum Youden index [Youd 50] to be the optimal choice for a threshold. The Youden index J for a given threshold is defined as follows:

$$J = \frac{tp \cdot tn - fp \cdot fn}{(tp + fn)(fp + tn)} = \underbrace{\frac{tp}{tp + fn}}_{\text{sensitivity}} + \underbrace{\frac{tn}{fp + tn}}_{\text{specificity}} - 1 \tag{4.16}$$

where tp is the fraction of true positives, fn the fraction of false negatives, fp the fraction of false positives, and tn the fraction of true negatives. The possible range of values is from zero to one inclusive.

For predicting an error of 2.5 mm or greater, the redundancy-based error prediction was able to correctly predict 50% of errors (sensitivity) and correctly predict 75% of absence of error (specificity). In comparison, the model-based error prediction achieved a sensitivity of 91% and a specificity of 79%. For predicting an error of 5.0 mm or greater, sensitivity and specificity would have been 62% and 75% (redundancy-based) versus 91% and 93% (model-based). Figure 4.7 confirms that the model-based error detection is superior to the tracking redundancy-based approach.

4.2. Hybrid Tracking with Feature-Based Video Tracking

In this section, we present a computer vision method for detection of the ultrasound transducer in laparoscopic videos, and for correction of the transducer's relative pose. This enables correction of all accumulated errors at once and optimises overlay accuracy, which matters most for intra-operative augmented reality.

Intra-operatively, the laparoscopic ultrasound probe tip needs to be constantly observed with the laparoscope camera, in order to avoid injury to the patient [Gang 06]. Thus, at every point during its use, the laparoscopic video images of the ultrasound probe tip are readily available. In addition, the intrinsic and extrinsic parameters of the laparoscope camera are known, and thus the images enable automatic detection and correction of tracking errors.

We follow approaches, which have already been developed for minimally invasive surgery. Similar to Climent and Marés [Clim 04] and Voros *et al.* [Voro 06] we use an edge detection filter and a Hough transformation [Houg 62] to extract edges from laparoscopic images. Furthermore, we use previous knowledge about the geometry of the probe tip, in order to select edges belonging to the probe tip.
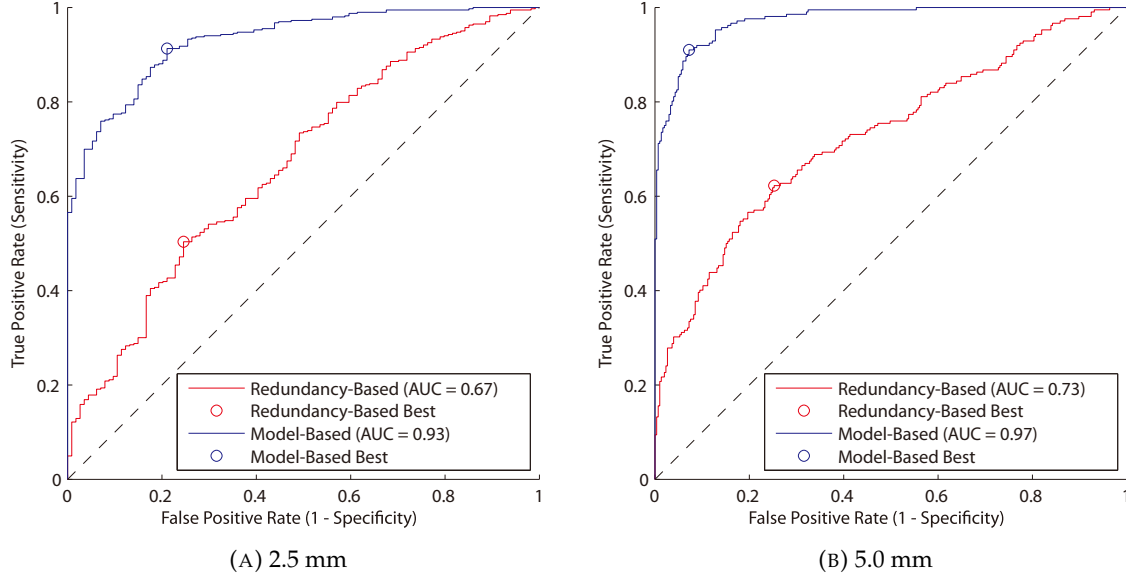
(A) 2.5 mm   (B) 5.0 mm

FIGURE 4.7.: **Receiver operating characteristic (ROC) curves for prediction of tracking errors of at least 2.5 or 5.0 mm. The point with the highest sum of sensitivity and specificity (highest Youden index) represents the optimal threshold for each approach.**

Voros *et al.* [Voro 06] and Doignon *et al.* [Doig 06] use information about the insertion points of laparoscopic instruments. These are fixed during the intervention and may be used to support segmentation, since edges of the rigid instruments are always aligned with the insertion points. In our case, however, due to bending of the probe tip, its edges will in general no longer be aligned with the insertion point. Thus, we use tracking data of the tip instead – of course, this approach may be combined with other error correction approaches like the model-based approach outlined above. The results of our probe tip axis segmentation are shown in Figure 4.8.

The laparoscope camera is tracked by optical tracking (OT). First, the transducer tip axis, defined by base point $\mathbf{b}$ and unit direction vector $\vec{\mathbf{d}}$ (cf. section 4.1.1), is transformed from the electromagnetic sensor (MS) coordinate system into camera coordinates (C) as

$$\begin{bmatrix} \mathbf{b}_C \\ 1 \end{bmatrix} = {}^{C}\mathbf{T}_{MS_{tip}} \begin{bmatrix} \mathbf{b}_{MS_{tip}} \\ 1 \end{bmatrix} \quad \text{and} \quad \begin{bmatrix} \vec{\mathbf{d}}_C \\ 1 \end{bmatrix} = {}^{C}\mathbf{T}_{MS_{tip}} \begin{bmatrix} \vec{\mathbf{d}}_{MS_{tip}} \\ 1 \end{bmatrix}, \qquad (4.17)$$

where

$$ {}^{C}\mathbf{T}_{MS_{tip}} = {}^{C}\mathbf{T}_{OM_{lap}} \cdot {}^{OM_{lap}}\mathbf{T}_{OT} \cdot {}^{OT}\mathbf{T}_{OM_{EMT}} \cdot {}^{OM_{EMT}}\mathbf{T}_{EMT} \cdot {}^{EMT}\mathbf{T}_{MS_{tip}}, \qquad (4.18)$$

and ${}^{C}\mathbf{T}_{OM_{lap}}$ is the transformation from the laparoscope OT target (OM) to the camera centre (as determined by camera calibration), ${}^{OM_{lap}}\mathbf{T}_{OT}$ is the transformation from the OT coordinate system to the laparoscope OT target, and ${}^{OT}\mathbf{T}_{OM_{EMT}}$ is the transformation from the EM tracking field generator OT target to the OT coordinate system (as measured by the tracking system).
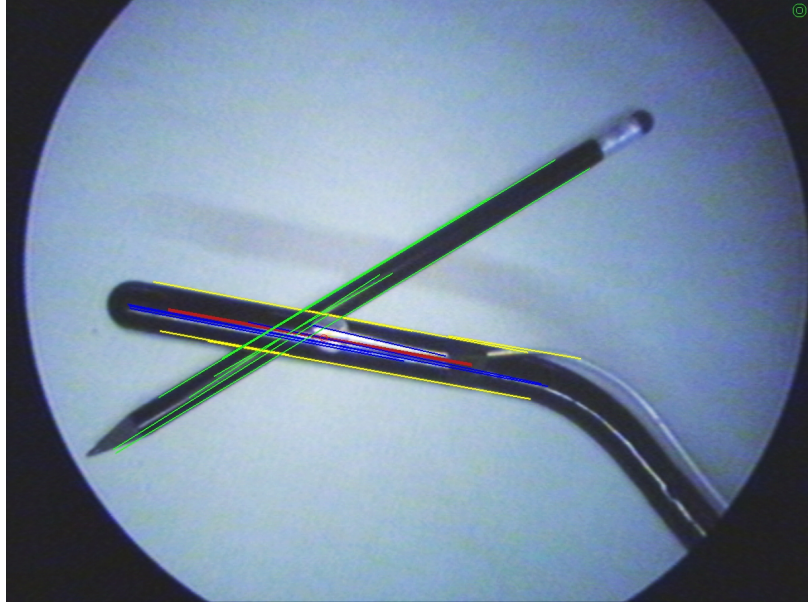
FIGURE 4.8.: **Results of transducer axis segmentation. Lines classified as belonging to the transducer tip edges are automatically colored yellow, lines belonging to the transducer (but not to the edges) are colored blue, the corrected transducer axis is thick red. Lines belonging to the pencil are rejected (colored green), because they do not match the measured transducer axis rotation.**

In order to automatically segment the probe tip in endoscopic video images, we use the "Open Source Computer Vision Library" (OpenCV) to first apply the Canny edge detection algorithm [Cann 86], which provides a binary mask of edges in the video image. This is then fed into a Hough transform [Houg 62], in order to gain a set of lines in the image.

In order to match these lines to the transducer tip axis, each line is first back-projected into space, i.e. its two endpoints $\mathbf{x}_{C1}$ and $\mathbf{x}_{C2}$ are projected from 2-D coordinates (x_i, y_i) to 3-D coordinates (x_C, y_C, z_C) in the image plane as

$$\mathbf{x}_C = \begin{bmatrix} x_C \\ y_C \\ 1 \end{bmatrix} \propto \begin{bmatrix} \lambda x_C \\ \lambda y_C \\ \lambda \end{bmatrix} = K^{-1} \begin{bmatrix} x_i \\ y_i \\ 1 \end{bmatrix} \tag{4.19}$$

Here K is the camera calibration matrix (cf. section 3.1), including the principal point and focal length [Hart 03], and $\mathbf{x}_C$ is on the image plane, i.e. without restriction of generality $z_C = 1$. Together with the camera centre $(0, 0, 0)$, these two end points $\mathbf{x}_{C1}$ and $\mathbf{x}_{C2}$ define a plane, which may completely be described by (in addition to the camera centre) its normal $\vec{\mathbf{n}}$ (cf. Figure 4.9 on page 48):

$$\vec{\mathbf{n}} = \frac{\mathbf{x}_{C1} \times \mathbf{x}_{C2}}{\|\mathbf{x}_{C1} \times \mathbf{x}_{C2}\|} \tag{4.20}$$

Since the order of the end points of each line is arbitrary, the normals $\vec{\mathbf{n}}$ may point in either direction. We obtain a unified representation of the plane normals, by inverting them, if $\vec{\mathbf{n}} \cdot (\vec{\mathbf{d}}_C \times \mathbf{b}_C) < 0$. Thus, all normals will point into the same direction as the cross

product of $\vec{\mathbf{d}}_C$ and $\mathbf{b}_C$ (cf. Figure 4.10). Then, the angle α between the transducer tip axis, as given by tracking, and each back-projection plane can be determined as

$$\alpha = \arcsin(\vec{\mathbf{n}} \cdot \vec{\mathbf{d}}_C). \tag{4.21}$$

The distance d between the base point $\mathbf{b}_C$ of the measured transducer tip axis, i.e. the point closest to the EM tracking sensor, and the plane is described by

$$d = \vec{\mathbf{n}} \cdot \mathbf{b}_C \tag{4.22}$$

Depending on whether d is positive, negative, or zero, $\mathbf{b}_C$ will be above (in the half-space, which the normal is pointing to), beneath, or on the plane. For each line, $|\alpha|$ and $|d|$ are checked against thresholds, and if both thresholds are matched, then we may assume that the line corresponds to an edge segment of the transducer tip.

These lines are then combined in a voting approach. Iterating over all previously selected edge segments, we identify the maximum and minimum values of d, i.e. $d_{\max}$ and $d_{\min}$. Since d may be positive or negative, both extrema correspond to the outermost segmented edge segments on both sides of the probe tip. In the ideal case, the difference $d_{\max} - d_{\min}$ is equal to the known probe tip diameter. Thus, the difference between measured and true probe tip diameter may be used for verification of our segmentation. In order to reject lines on the transducer itself, in contrast to actual edges, we reject all lines, which are more than a certain threshold distance from the outermost edge segments. Such falsely segmented lines might be due to e.g. specular reflections on the probe tip.

From the remaining edges $1 \ldots m$, the mean of the plane normals

$$\vec{\mathbf{n}}_{\text{mean}} = \frac{\sum_{i=1}^{m} \vec{\mathbf{n}}_i}{\|\sum_{i=1}^{m} \vec{\mathbf{n}}_i\|}, \tag{4.23}$$

and the mean angle

$$\alpha_{\text{mean}} = \frac{\sum_{i=1}^{m} \alpha_i}{m} \tag{4.24}$$

between transducer tip axis and plane are computed. The estimated distance d_{est} between the segmented, correct transducer axis and electromagnetically measured transducer axis can then be computed as the mean of minimum and maximum distances $d_{est} = (d_{max} + d_{min})/2$.

The correction transform is then computed as one translation and one rotation: The measured probe tip axis is translated along the mean plane normal $\vec{\mathbf{n}}_{\text{mean}}$ by the estimated distance d_{est}, i.e. $d_{\text{est}} \cdot \vec{\mathbf{n}}_{\text{mean}}$, such that the axis origin will be in the middle of the segmented probe tip. Then, the measured probe tip axis is rotated, such that it coincides with the segmented axis. Since the axis of rotation is orthogonal to both the mean plane normal as well as the measured tip axis direction, it can be computed as $\vec{\mathbf{r}} = \vec{\mathbf{n}}_{\text{mean}} \times \vec{\mathbf{d}}_C$. Finally, the rotation can be computed from $\vec{\mathbf{r}}$ and the mean angle α_{mean} using Rodrigues' rotation formula [Murr 94]. This transforms the electromagnetically measured tip axis to a pose, from where it will be projected onto the image plane in such a way that it is exactly aligned with the segmented probe tip axis.

Please note that while this image-feature based approach may be combined with other error correction methods, this is optional, and the image-feature based method only relies on video images and some previous knowledge about the probe tip geometry.
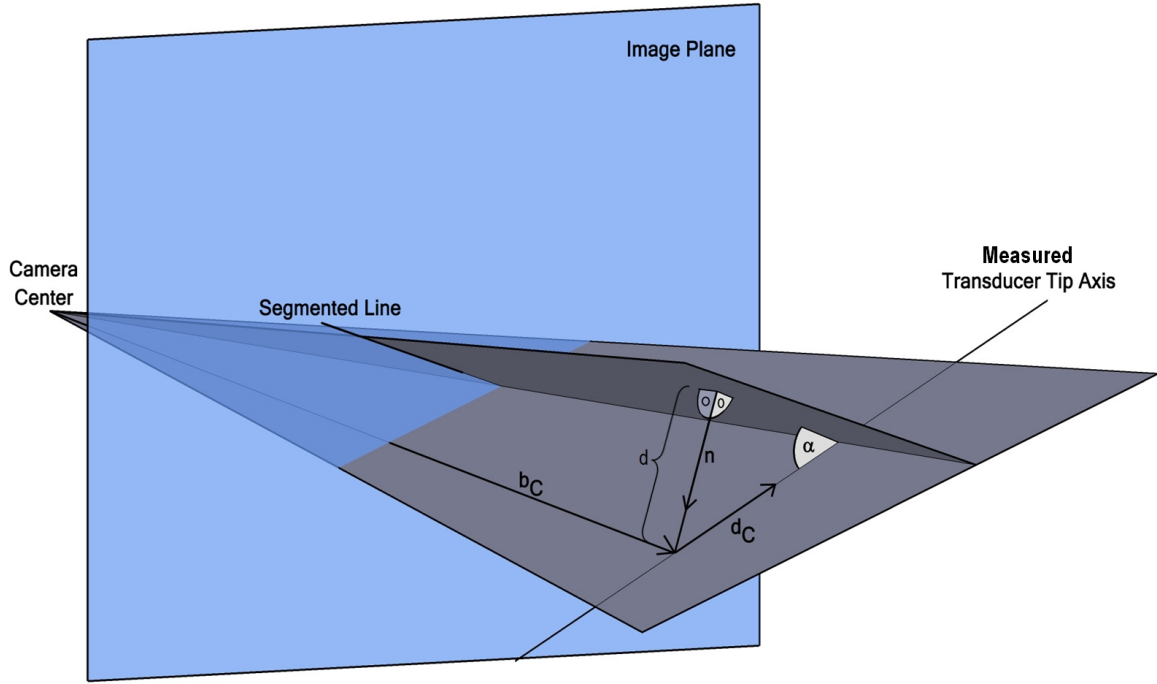
FIGURE 4.9.: **Back-projection of a segmented ultrasound transducer edge and its comparison to the transducer tip axis measured by electromagnetic tracking.**
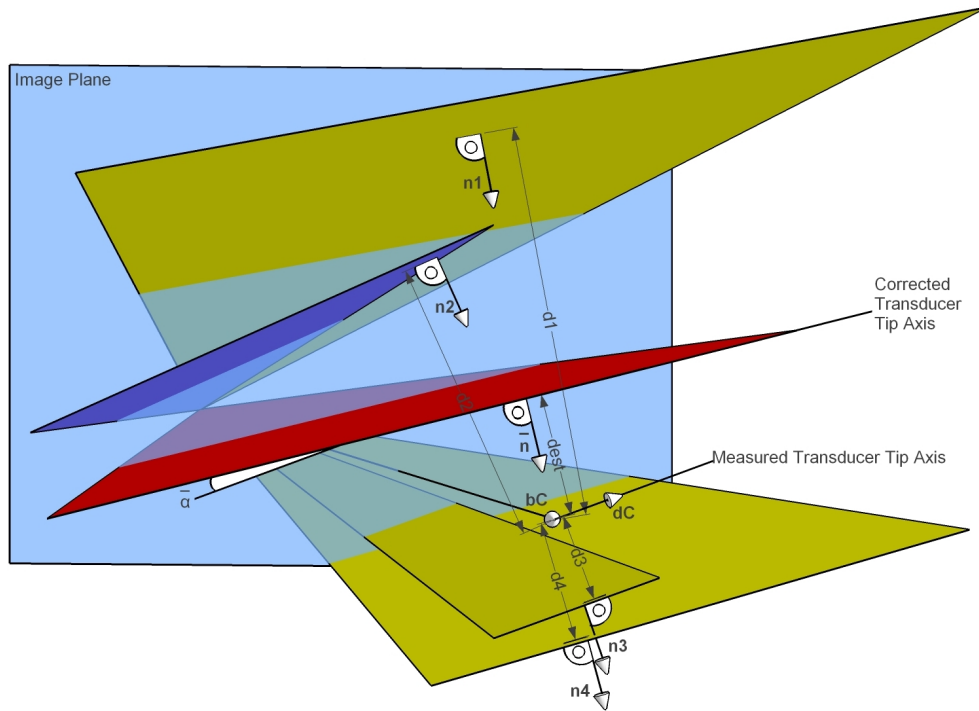

FIGURE 4.10.: **Back-projection of four segmented transducer edges, which generates four planes and their corresponding normals. Image courtesy of Feuerstein *et al.* [Feue 08b].**
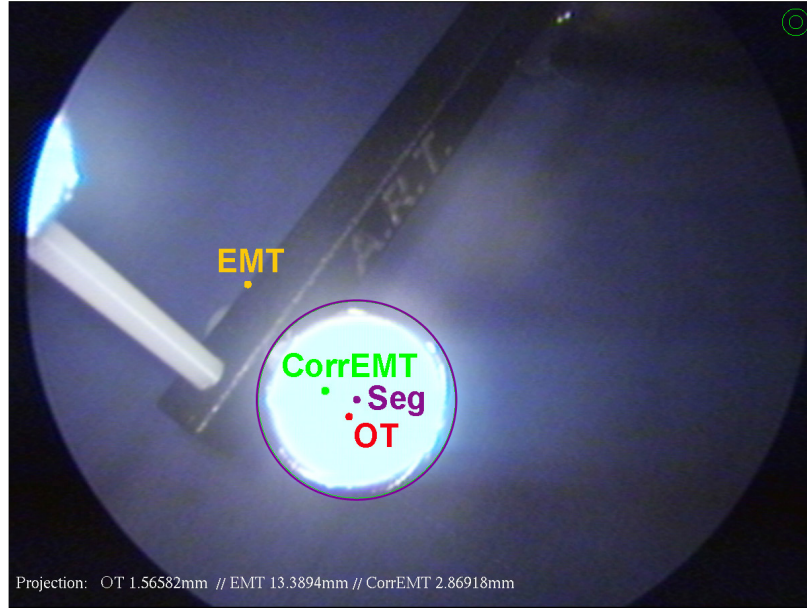
Projection: OT 1.56582mm // EMT 13.3894mm // CorrEMT 2.86918mm

FIGURE 4.11.: **2-D overlay accuracy evaluation by segmentation. "Seg" denotes the segmented position of the sphere (ground truth), "OT" is the projection of the optical marker positing, "EMT" is the projection of the uncorrected EM tracking sensor measurement, and "CorrEMT" is the projection of a corrected EM tracking sensor position.**

Evaluation of Feature-Based Video Tracking: The feature-based error correction minimises overlay error within the image plane. Thus, for evaluation of image plane error we need to provide other features in the image plane. We can use the temporary optical tracking target at the tip of the laparoscopic ultrasound transducer (cf. Figure 4.1), as well as the transformation $^{OM_{tip}}\mathbf{T}_{MS_{tip}}$ between the electromagnetic tracking sensor at the tip and the new optical tracking target.

Due to the laparoscope camera's own light source, tracking markers appear as bright spheres in the video image and can be segmented by simple thresholding. Uncorrected and corrected positions of the EM tracking sensor can be transformed to the optical tracking target's positing using $^{OM_{tip}}\mathbf{T}_{MS_{tip}}$, and projected into the image plane, the location of which is known from camera calibration. Then the projected positions can be compared to the segmented ground truth, as shown in Figure 4.11. The performance of different error correction methods is shown in Figure 4.12.

4.3. Hybrid Tracking with Image Registration

In endoscopic procedures, live video images are available and intensity-based registration of the 2-D video image and a pre-operative 3-D computed tomography (CT) volume can be used for tracking. Hybrid electromagnetic and image-based tracking employs electromagnetic tracking for initialisation and image registration for accuracy.
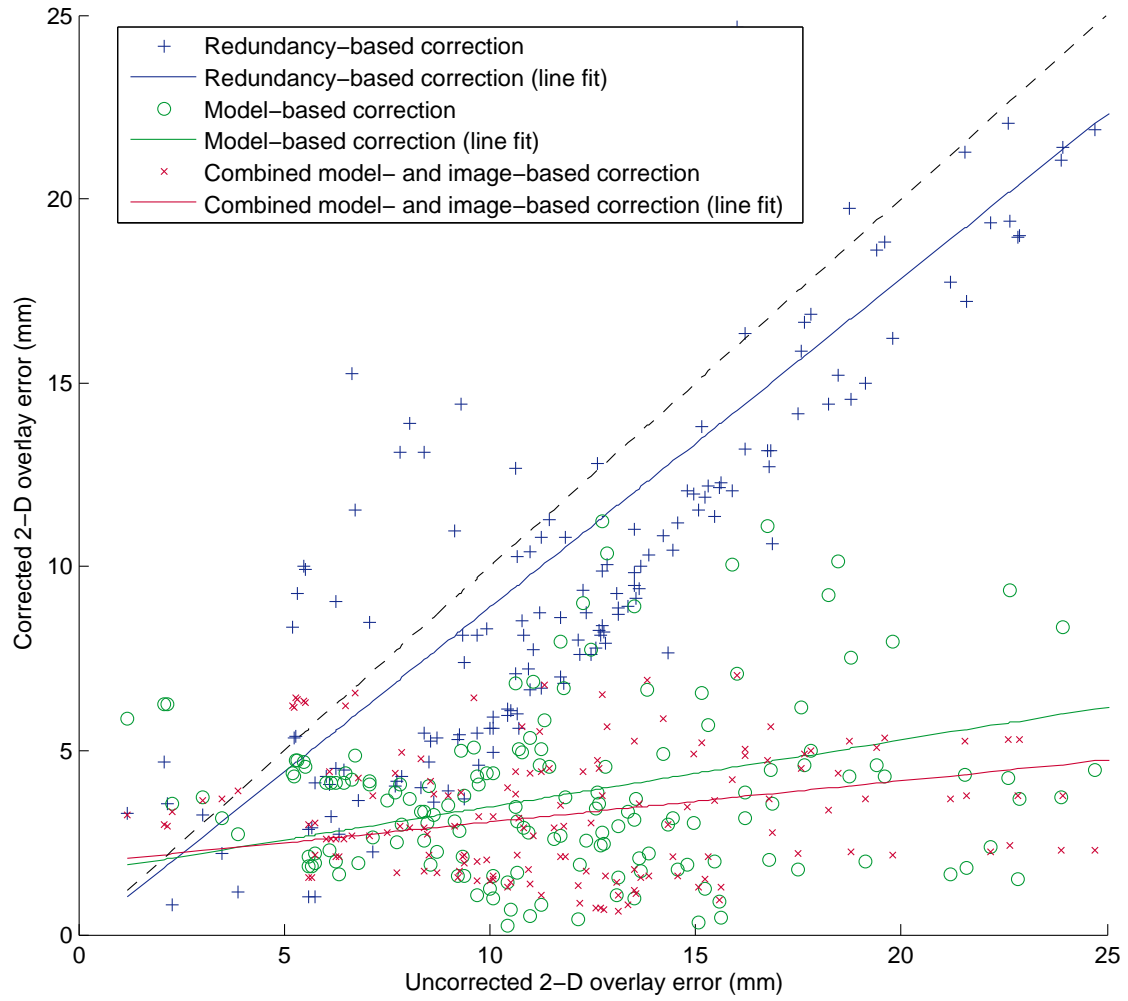
FIGURE 4.12.: **2-D overlay error correction performance of different methods. The error remaining after each correction is plotted against uncorrected error. For visual comparison, the dashed line represents the original error without correction.**

For the tracking of flexible endoscopes within patients, there is only little correlation between those parts, which can be observed outside the body, and the actual tip of the endoscope. Thus, tracking is more challenging than for rigid instruments. However, navigation systems still promise benefits through visualisation of additional information from pre-operative planning, e.g. the precise location of biopsy target sites.

Since endoscopy is an inherently monitor-based procedure, augmentation of intra-operative video images with guidance or targeting information is straightforward and promises high clinical acceptance due to smooth integration into the clinical workflow. Visual indications of otherwise invisible targets will enable a more precise guidance. For such overlays, accurate tracking information about the position and orientation of the endoscope camera relative to the patient is required.

For example, flexible bronchoscopy is a widespread clinical procedure for diagnosis and treatment of lung diseases, and one of its most common applications is transbronchial biopsy – in particular of lung cancer, which is the most common cause of cancer-related death in men and women worldwide [Park 05]. Bronchoscope tracking by electromagnetic (EM) tracking systems has been known for more than a decade [Solo 98, Gild 06, Schw 06]. However, patients are breathing, occasionally coughing and choking, and the insertion of the bronchoscope may cause additional deformation of the lung. Thus, motion correction for tracking is necessary, and complementary information is required.

It is possible to constrain the assumed position of the tracked endoscope to follow the airways [Vett 07, Gerg 10], as defined by segmentation of the CT volume. However, for bronchoscopes, image-based tracking enables more precise location.

Image-Based Tracking: Where imaging data is already available, an image-based tracking approach does not introduce any additional hardware or changes in the clinical workflow. Image-based tracking has been proposed for interventions, where tools are already required to be constantly observed via imaging systems. Examples include ultrasound-guided needle biopsy [Ding 03], or catheter tracking in fluoroscopy [Paul 10]. In the case of flexible endoscopy, video imaging is available all the time.

If the navigation system involves AR overlays, errors may accumulated over patient registration, EM tracking, and camera calibration. However, image-based is complementary to EM tracking, since it allows to refine precisely the position and orientation of the endoscope camera relative to the patient. This is exactly the spatial relation, which is most important for augmentation.

Tracking based on the image sequence only has been proposed [Wu 04], but if the video images are combined with pre-operative imaging data like CT volumes, then more information is available. Such data is routinely available in clinical practice, since often it was an original finding in the CT image, which indicated the endoscopic follow-up examination or biopsy. Most image-based endoscope tracking approaches have been described for bronchoscopy, since here the anatomy is comparatively stable between pre-operative CT imaging and intra-operative video imaging, in contrast to gastroscopy, or colonoscopy. There have been approaches to tracking of endoscopes by using image features [Wu 04], in contrast to image intensity. However, the environment in bronchoscopy is mostly texture-less, and texture information is not available from e.g. CT data. This leaves intensity-based registration of the 2-D video image and the 3-D CT volume as the primary approach to
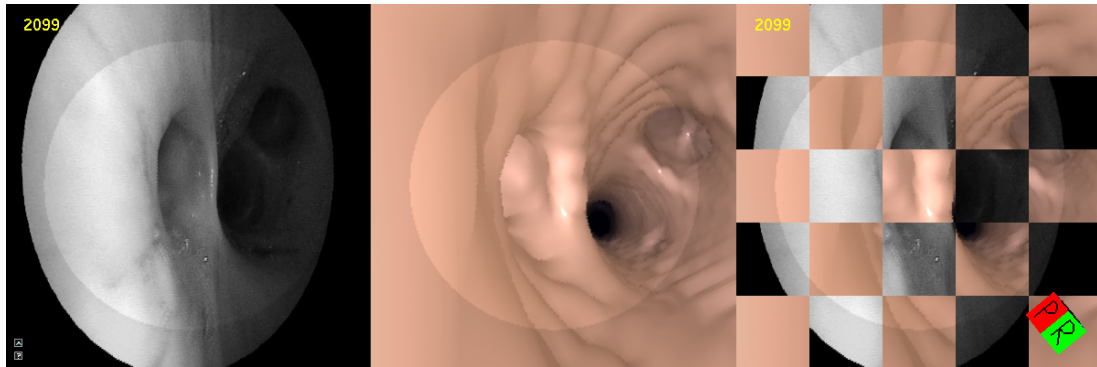
FIGURE 4.13.: **Navigated bronchoscopy user interface with real bronchoscopic image (left), virtual bronchoscopic image rendered at current position and orientation (centre), and chequerboard overlay (right).**

image-based endoscope tracking.

There has been a large body of work on 2-D/3-D registration, mostly considering registration of 3-D CT or Magnetic Resonance Imaging (MRI) data to intra-operative 2-D X-ray imaging. Please refer to Markelj *et al.* [Mark 10] for an excellent review of methods. For bronchoscopy, so-called *virtual bronchoscopy* has been proposed, and may be used for 2-D/3-D registration.

Virtual Bronchoscopy: In order to improve visualisation of 3-D CT images, the rendering of 2-D images similar to a bronchoscopic examination was proposed [Bric 98, Engl 98]. Such a method may be extended to include other modalities like Positron Emission Tomography (PET) [Seem 07], if combined PET/CT images are available. Virtual bronchoscopy was found useful, but only as complement to real fibre-optic bronchoscopy [Flei 97, De W 05]. For a comparison of real and virtual bronchoscopy images, please see Figure 4.13.

For image-based tracking, virtual bronchoscopy is a representation of the CT volume, which enables registration to the video image. Besides providing the same dimensionality for comparison, via simulation of one modality (2-D video) from another (3-D CT) we are essentially turning a multi-modal registration in a mono-modal one. The appearance of the virtual bronchoscopy image is supposed to be close to the real bronchoscopy image, and thus image similarity measures like Normalised Cross Correlation (NCC) can be used, rather than the more complex measures like Mutual Information [Viol 97]. However, a CT image describes volumetric X-ray absorption, while video describes optical surface properties. There are straightforward methods for volume-rendering of CT images, producing images similar to video, but properties like colour, reflectance, etc. need to be tuned, and due to the different imaging principles and resolutions, a perfect match cannot be achieved. Still, similarity measures like NCC are mostly used, in order to achieve computational efficiency.

Image-Based Bronchoscope Tracking: Bronchoscope tracking by only image registration with virtual bronchoscopy was proposed [Sher 00, Helf 01, Mori 02]. As such, this method

does not yet require any additional tracking hardware. Also, since only the relative position within the patient airways is relevant, it does not yet have to consider deformation of the lung. During breathing motion the bronchoscope moves together with the surrounding bronchi, so its position relative to the patient anatomy does not change.

Computational efficiency strongly depends on the comparatively costly rendering of the virtual bronchoscopy image for each evaluation of the cost function. This rendering step also impedes analytical description of the cost function gradient. Gradients, if needed, have to be estimated using finite differences during numerical optimisation. In order to improve convergence of the image registration step, similarity measures have been improved by selecting only blocks with "characteristic structure" [Degu 03]. Alternatively, fast estimates based on the real images only have been proposed using epipolar geometry [Mori 01], texture mapping [Shoj 01], or depth warping [Rama 99, Rai 08].

Image registration alone can only provide incremental tracking due to the overall self-similarity of the airways. Thus, if tracking is interrupted due to quick motion, or if the endoscope is moved, while the view is obscured, tracking has to be re-initialised again. While global search methods for image-based bronchoscope tracking have been proposed [Khar 10, Khar 11], these are still limited by the size of the search space. Also, due to the overall cylindrical shape of the airway branches, rotation around the bronchoscope's viewing direction is difficult to capture. During bronchoscopy, manual rotation of the endoscope is constantly required for steering.

Thus, image-based tracking was extended to hybrid electromagnetic and image-based tracking [Mori 05, Degu 06, Sope 10]. Here, the position and orientation given by electromagnetic tracking are used as initialisation for image registration. This can be further extended with motion prediction [Naga 04, Mori 06].

Shape-Based Matching: One weakness of bronchoscope tracking by intensity-based registration of images is that the position accuracy is worse along the view direction than laterally. Translations along the view direction result in only small changes in the image similarity, and this is obscured further by the remaining, unavoidable discrepancies between the pre-operative CT volume and the intra-operative video.

In the future, tracking of flexible endoscopes might be improved by matching 3-D data to the 3-D CT volume. "Shape from shading" [Rash 92, Okat 97] has been applied to bronchoscope tracking [Bric 98, Deli 04, Sute 04], and registration of 3-D point clouds to 3-D surfaces from CT data has been proposed for image-based tracking [Miro 09]. Such approaches do not depend on a photo-realistic rendering sub-step, but the shape-from-shading sub-step in turn is affected by specularities and mucus on the airway surface.

Evaluation of Bronchoscope Tracking: In previous works, tracking of bronchoscopic video relative to CT data was usually evaluated via the duration of successful tracking [Mori 05], the fraction of "correctly matched frames" [Luo 10b], distance to airway centreline [Wegn 08], fraction of positions within airways [Klei 07], or distance between successive result positions [Gerg 10]. Such criteria are either strongly dependent on data sets and a subjective definition of "successful tracking", or biased if the very same criteria have been optimised before. The ground truth data problem was explained in details by Mountney *et al.* [Moun 10].

As an extension of the "manual registration" approach by Soper *et al.* [Sope 10] we proposed [Reic 11] an evaluation based on expert-provided ground truth data. A direct deduction of clinical relevance is possible, and from the agreement within experts and between multiple experts the limits of image-based methods can be learned.

Ground truth data is independently and repeatedly collected by multiple experts, preferably medical or scientific experts. Recording is started from the first frame in each video sequence and a neutral, approximately correct position for the first frame. For each real image the position and orientation of the virtual bronchoscopic image are manually adjusted, until both images match as closely as possible. Adjustment may be done using mouse and keyboard, or more ergonomically with 6-D input devices like the SpaceNavigator (3Dconnexion, München, Germany) or PHANTOM Omni (Sensable, Wilmington, MA, USA). Each expert is blinded to the other experts' results, as well as to his own results from previous sessions. Since this process is extremely time-consuming, only a subset of frames may be matched, evenly distributed over the full image sequence.

For analysis, pose data from multiple sessions is first averaged per expert, then these intermediate results are averaged between all experts. Intra-expert agreement and inter-expert agreement are computed as mean standard deviation of selected poses and averaged over all poses, either for each single expert's poses, or for all experts. These agreement values can then be used to indicate general limits for approaches based on registration of real and virtual bronchoscopy images. For example, in our own experiments we found an inter-expert agreement of 1.26 mm and 4.78° [Reic 11].

4.3.1. Tracking with Smooth Output

When electromagnetic tracking is used as an initialisation for image registration, small changes in the initialisation may lead to different local minima, and noise is amplified by hybrid tracking. By modelling the output as continuous and using splines for interpolation, smoothness is greatly improved. [1]

While accuracy and computational speed are clearly important for real-time applications like intra-operative navigation, smoothness of the output is no less relevant. Less jitter of augmented reality overlays increases operator comfort and acceptance. Smooth output may provide benefits when further processing the output for motion models, or for temporal and spatial synchronisation of multiple video sequences in the case of repeat examinations or clinical studies.

An ongoing challenge is compensation of dynamic tracking errors, which can be due to patient movement, breathing motion, or cardiac motion, as well as errors from EM tracking artefacts due to quick movements of sensors. With hybrid EM and image-based tracking methods small changes in the EM measurements can lead to large jumps between local minima after image-based registration. Such jumps in the tracked endoscope position and orientation in turn affect where augmented reality overlays are placed, leading to a shaky visualisation. A new approach to this problem is modelling the true trajectory as continuous. This will yield a more consistent, physically plausible, and clinically acceptable tracking result.

---

[1]For a revised version of this section, please refer to the subsequent publication. [Reic 13b]

A continuous description of bronchoscope pose at time t is given by its position $\mathbf{p}(t)$ and orientation $\mathbf{q}(t)$. Since both the real movement of the bronchoscope and the movement of anatomy (breathing, heartbeat, etc.) are spatially smooth over time, movement of the bronchoscope relative to patient anatomy is smooth as well.

Control points are assigned to frames with regular time spacing s and initialised with the original EM tracking measurements. For interpolation of position we use Catmull-Rom splines [Catm 74], a special class of cubic Hermite splines, where tangents are continuous over multiple segments. The resulting curve is continuously differentiable and passes directly through the control points:

$$\mathbf{p}(t) = \frac{1}{2} \begin{pmatrix} 1 & u & u^2 & u^3 \end{pmatrix} \begin{pmatrix} 0 & 2 & 0 & 0 \\ -1 & 0 & 1 & 0 \\ 2 & -5 & 4 & -1 \\ -1 & 3 & -3 & 1 \end{pmatrix} \begin{pmatrix} \mathbf{p}_{i-1} \\ \mathbf{p}_i \\ \mathbf{p}_{i+1} \\ \mathbf{p}_{i+2} \end{pmatrix}, \tag{4.25}$$

where $\mathbf{p}_{i-1\ldots i+2}$ are positions of consecutive control points, $i = \lfloor t/s \rfloor$ is a control point index, and $u = t/s - \lfloor t/s \rfloor$ is the interpolation ratio between control points $\mathbf{p}_i$ and $\mathbf{p}_{i+1}$.

For orientation we use quaternions, because they allow a continuous representation without gimbal lock. Then, for interpolation between quaternions we use spherical linear interpolation (SLERP) [Shoe 85], which provides "smooth and natural" motion:

$$\mathbf{q}(t) = \mathbf{q}_i \, (\mathbf{q}_i^{-1} \, \mathbf{q}_{i+1})^u = \frac{\sin(1-u)\theta}{\sin\theta} \, \mathbf{q}_i + \frac{\sin u\theta}{\sin\theta} \, \mathbf{q}_{i+1}, \tag{4.26}$$

where θ is the rotation difference between $\mathbf{q}_i$ and $\mathbf{q}_{i-1}$. Initial parameters $\mathbf{p}_k$ and $\mathbf{q}_k$ for all control points are taken directly from the EM tracking measurements.

Then, each for each control point i its position $\mathbf{p}_i$ and orientation $\mathbf{q}_i$ are optimised with respect to a cost function $E(\mathbf{p}, \mathbf{q})$. For the matching between bronchoscope images and CT image, we employ as an intermediate step virtual bronchoscopic images $I_V(\mathbf{p}_k, \mathbf{q}_k)$, where the CT image is rendered for a camera with position $\mathbf{p}_k$ and orientation $\mathbf{q}_k$. Also, where information about airway structure is available, e.g. in the form of a distance map, we include this as well. Adding regularisers incorporating EM tracking measurements and bending forces along the trajectory, we seek to maximise

$$E(\mathbf{p}, \mathbf{q}) = \underbrace{S(\mathbf{p}, \mathbf{q})}_{\text{similarity}} - \underbrace{\lambda_1 \cdot D(\mathbf{p})}_{\text{structure}} - \underbrace{\lambda_2 \cdot R_T(\mathbf{p}, \mathbf{q})}_{\text{displacement}} - \underbrace{\lambda_3 \cdot R_B(\mathbf{p})}_{\text{bending}}, \tag{4.27}$$

where $\lambda_{1\ldots3}$ are weighting parameters.

Image Similarity: The similarity $S(\mathbf{p}, \mathbf{q})$ between real and virtual images is computed via the Local Normalized Cross Correlation (LNCC)

$$S(\mathbf{p}, \mathbf{q}) = \sum_k \text{LNCC}(I_R(t_k), I_V(\mathbf{p}_k, \mathbf{q}_k)), \tag{4.28}$$

where k is an image index in the neighbourhood of the current control point, $I_R(t_k)$ is the real image at time t_k, and $I_V(\mathbf{p}_k, \mathbf{q}_k)$ is the virtual bronchoscopic image. The patch size for LNCC was set to 11 pixels. The gradient of $S(\mathbf{p}, \mathbf{q})$ for movement for each single

control point i can be approximated from the frames in its support $(i - 2, i + 2)$ via finite differences. This is closely related to bundle adjustment, where multiple images are registered together e.g. for fibre-optic video mosaicing [Atas 08]. Frames outside its support are not influenced by movement of this control point, so gradient computation can be decoupled for each control point. In addition, since the total number of frames is constant, the total computational effort does not depend on the number of control points.

Airway Structure: $D(\mathbf{p})$ is the Euclidean distance from each position $\mathbf{p}$ to the nearest airway voxel. Segmentation of airways can be performed using an iterative region growing approach [Gerg 10], and for computational efficiency a distance map can be computed. All positions inside the airways have a distance of zero.

   Since the bronchoscope does not necessarily move close to the bronchus centrelines, the effect of $D(\mathbf{p})$ is similar to a maximisation of the number of measurements which are inside the airways [Klei 07]. Since the continuous-by-definition trajectory is an even stronger consistency condition than e.g. a particle filter, we do not need to match the measurements to the nearest bronchus. Such a projection could match the position into the wrong bronchus. Instead, jumping between neighbouring bronchi is prevented by the uniqueness of the spline curve.

Displacement from EM measurements: According to Hooke's law, spring force is proportional to displacement, so we model tension, the cost of distance from the EM tracking measurements, as

$$R_T(\mathbf{p}, \mathbf{q}) = \sum_k \left[\alpha \cdot \| \mathbf{p}_k - \mathbf{p}_{k,0} \| + \theta(\mathbf{q}_k, \mathbf{q}_{k,0}) \right], \tag{4.29}$$

   where $\mathbf{p}_{k,0}$ and $\mathbf{q}_{k,0}$ are the position and orientation measured by EM tracking at time t_k, and the rotation difference $\theta(\mathbf{q}_k, \mathbf{q}_{k,0})$ is computed as the angular component of the difference quaternion. α is the ratio between rotational and translational spring constants and was set to $3.10°/\text{mm}$, since this was the ratio of errors observed with the human experts when recording ground truth data.

Bending: In addition to the inherent smoothness of the spline curve, another term penalises large translations between control points. According to Euler–Bernoulli beam theory, the bending moment of the trajectory is proportional to its curvature, so we choose analogously

$$R_B(\mathbf{p}) = \sum_k \left\| \nabla_k^2 \mathbf{p}_k \right\|. \tag{4.30}$$

Optimisation: We iteratively estimate the optimal parameters for $E(\mathbf{p}, \mathbf{q})$ by gradient descent. The updated parameters $\mathbf{p}_u, \mathbf{q}_u$ are given by

$$\nabla E(\mathbf{p}, \mathbf{q}) = \nabla S(\mathbf{p}, \mathbf{q}) - \lambda_1 \cdot \nabla D(\mathbf{p}) - \lambda_2 \cdot \nabla R_T(\mathbf{p}, \mathbf{q}) - \lambda_3 \cdot \nabla R_B(\mathbf{p}, \mathbf{q}) \tag{4.31}$$

$$(\mathbf{p}_u, \mathbf{q}_u) \leftarrow sign(\nabla E(\mathbf{p}, \mathbf{q})) \cdot min(\tau \cdot \| \nabla E(\mathbf{p}, \mathbf{q}) \|, \delta), \tag{4.32}$$
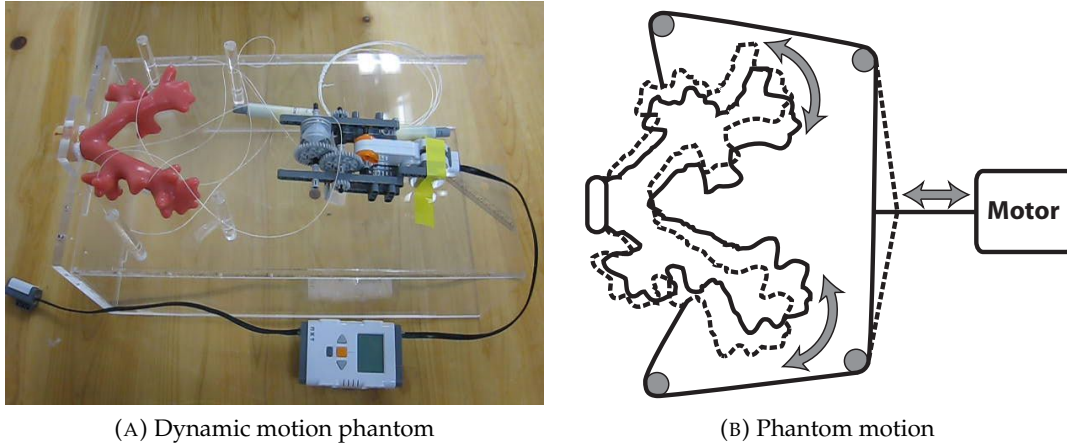
(A) Dynamic motion phantom

(B) Phantom motion

FIGURE 4.14.: **Dynamic motion phantom (4.14a) and phantom motion (4.14b).**

where τ is a magnitude control parameter, and δ is the maximum step width.

The gradient is approximated via finite differences, and the framework is extensible to include other measures, similar to inclusion of a distance map or image similarity, where a closed form description of the gradient might not be available.

During optimisation, only data for a neighbourhood of frames needs to be available, so frames can be processed in sequence like with previous approaches. With real-time implementations, obviously only frames up to the current time may be considered. However, with off-line applications all data is available, so the optimisation might "look ahead" for additional motion compensation.

Registration Refinement: For each control point, the original EM tracking measurements and a corrected position are available. Thus, after a trajectory has been processed once, it is possible to compute the optimal Euclidean transform between both point sets, i.e. between original and corrected positions. This is similar to an update step of the Iterative Closest Point (ICP) algorithm [Besl 92]. A visual inspection of all accessible branches is commonly recommended my medical guidelines prior to a bronchoscopic procedure [Haus 04], and the refined and approved registration can then be used for subsequent navigation and visualisation, well integrated into the clinical workflow.

Evaluation Set-Up: We use a 3D Guidance EM tracking system (Ascension Technology, Burlington, VT, USA) with flat-bed field generator and model 130 sensors, and a BF-P260F flexible fibre-optic bronchoscope (Olympus, Tokyo, Japan). One EM tracking sensor was fixed inside the bronchoscope working channel.

The dynamic phantom is a CLA 9 (CLA, Coburg, Germany), which was chosen due to its closely human-mimicking surface. It was connected to a motor (Lego, Billund, Denmark) via nylon threads (cf. Figure 4.14). Four data sets consisting of video sequences and EM tracking data recordings were acquired with different amplitudes of simulated breathing motion between 7.48 and 23.65 mm, which corresponds to motion amplitudes determined for humans [Hanl 99].

(A) EM tracked endoscope
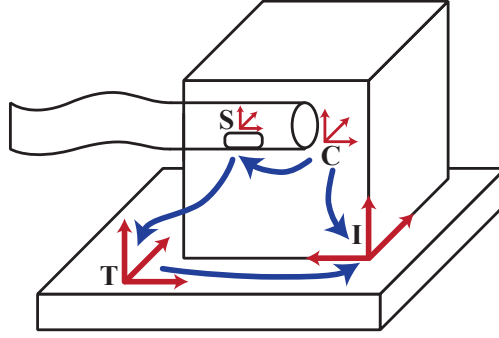
(B) Coordinate systems

FIGURE 4.15.: **Bronchoscope with embedded electromagnetic tracking sensor (4.15a) and coordinate systems (4.15b): bronchoscope camera (C), CT image (I), electromagnetic tracking (T), and tracking sensor (S) coordinate frames. The transformation $^T\mathbf{T}_S$ is measured, the transformations $^S\mathbf{T}_C$ and $^I\mathbf{T}_T$ are calibrated, and the transformation $^I\mathbf{T}_C$ is optimised for each frame.**

A CT scan of the phantom was acquired with 0.5 mm slice thickness. The broncho-scope and the different coordinate systems and transformations are shown in Figure 4.15. For point-based registration between CT and EM tracking coordinate systems, 29 external landmarks were used, average residual error was 0.92 mm. Camera intrinsics, deformation, and hand-eye calibration were performed as described in section 3.1.

Both video sequence and CT data were stored in graphics processing unit (GPU) memory, and virtual bronchoscopic image rendering as well as similarity were computed on GPU using OpenGL. Experiments were conducted on a standard workstation with Windows XP, an Intel Core Duo T9400 CPU, 4 GB RAM, and an NVidia Quadro FX 770M GPU.

Ground Truth Data: Following the evaluation approach outlined in section 4.3, ground truth data was independently and repeatedly collected by two experts, one expert bron-choscopist (A) and one scientist (B). For each real image, the position and orientation of the virtual bronchoscopic image were manually adjusted, until both images matched as closely as possible.

Intra-expert agreement (mean standard deviation) was 1.66 mm and 5.80° (A) and 1.44 mm and 3.94° (B). Inter-expert agreement was 1.26 mm and 4.78°. The ratio between intra- and inter-expert agreement indicates considerable overlap between the experts' results. These margins might indicate a limit for any approach based on registration of real and virtual bronchoscopy images.

Results and Comparison: We compare the proposed method to our own implementations of four previously published approaches: bronchoscope tracking by EM tracking only [Solo 00], intensity-based registration (IBR) with direct initialization from EM tracking [Mori 05], IBR with dynamic initialisation from EM tracking [Luo 10a], and IBR with a

	Accuracy	Smoothness
Solomon *et al.* [Solo 00]	5.87 ± 2.67 mm $10.55 \pm 6.16°$	3.20 ± 1.68 mm $3.40 \pm 9.22°$
Mori *et al.* [Mori 05]	5.59 ± 2.91 mm $10.55 \pm 6.37°$	3.72 ± 2.23 mm $4.98 \pm 10.89°$
Luo *et al.* [Luo 10a]	5.17 ± 3.29 mm $10.75 \pm 6.79°$	3.24 ± 2.24 mm $4.57 \pm 10.57°$
Luo *et al.* [Luo 10b]	4.52 ± 3.08 mm $10.62 \pm 6.14°$	2.77 ± 2.08 mm $3.46 \pm 9.46°$
Proposed Method	4.91 ± 2.57 mm $11.48 \pm 6.09°$	**1.24 ± 0.82 mm** $3.00 \pm 8.36°$
Expert agreement	1.26 mm $4.78°$	– –

FIGURE 4.16.: **Hybrid image-based and electromagnetic tracking errors and smoothness. In middle column, mean error and standard deviation with respect to ground truth are given for translation and rotation. Accuracy is equivalent with regard to expert agreement. In right column, mean inter-frame distance and standard deviation are given for translation as well as rotation. Smoothness is significantly improved by the proposed method.**

Sequential Monte Carlo sampler based on EM tracking [Luo 10b]. Quantitative results for the accuracy relative to ground truth, and smoothness of the output in terms of inter-frame distances are given in Table 4.16. Accuracy was evaluated relative to expert-provided data, and the accuracy of the proposed method is equivalent to previous approaches with regard to expert agreement. In addition, our results for previous methods agree with Soper *et al.* [Sope 10], who reported mean distances of 2.37 mm and $8.46°$.

The main result is that the proposed method shows significantly better smoothness. In order to also visualise the difference, two output trajectories are shown in Figure 4.17. The close-up view shows significantly less jitter in the output of the proposed method than of the previous approach. We attribute most of the remaining inter-frame distance to the real bronchoscope motion. Due to the smoothness constraint, our method by design provides a more realistic and physically plausible solution to the tracking problem, which has significantly less jitter. Video output is much more consistent and robust [Reic 11], with fewer occasions of tracking loss or unexpected movement. The filtering effect removes noise from the input, but can also lead to some loss of detail, if e.g. the direction of motion changes. These results were confirmed by an evaluation using the ArtiChest thorax phantom (PROdesign, Heiligkreuzsteinach, Germany) with an ex-vivo porcine lung explant, cf. Figure 4.18 [Reic 12].

Computation time is 0.98 seconds per frame, i.e. between 12.8 and 14.9 minutes for the 781 to 911 frames of our video sequences. For other methods a run time between 0.75 and 2.5 seconds [Mori 05, Luo 10a, Luo 10b, Sope 10] per frame is reported, so our computation speed is equivalent to previous approaches.

We expect our method to be robust against transient artefacts occurring in real clinical images, like specular reflections or bubbles, since groups of frames are matched and
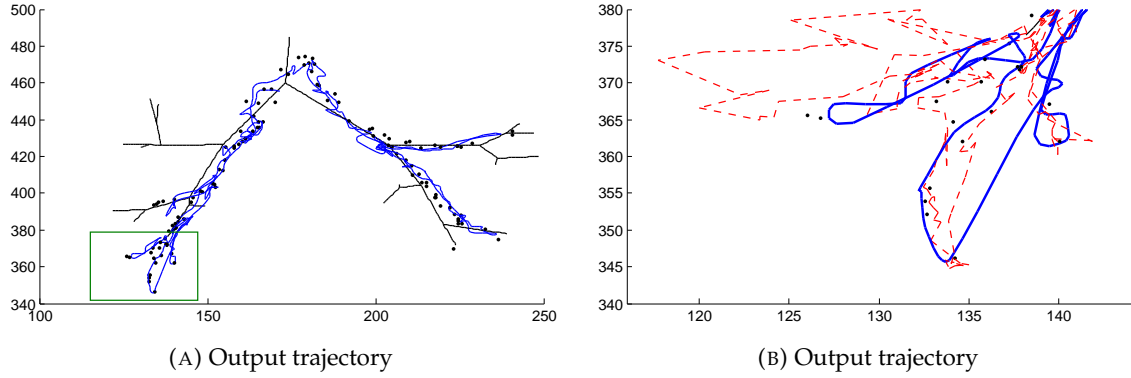
(A) Output trajectory

(B) Output trajectory

FIGURE 4.17.: **4.17a) Airway structure, trajectory from proposed method (solid blue), and ground truth positions (black dots). Close-up region is indicated as green rectangle. 4.17b) Close-up view of trajectories from previous approach [Luo 10b] (dashed red) and proposed method (solid blue), showing much smoother output of the latter.**
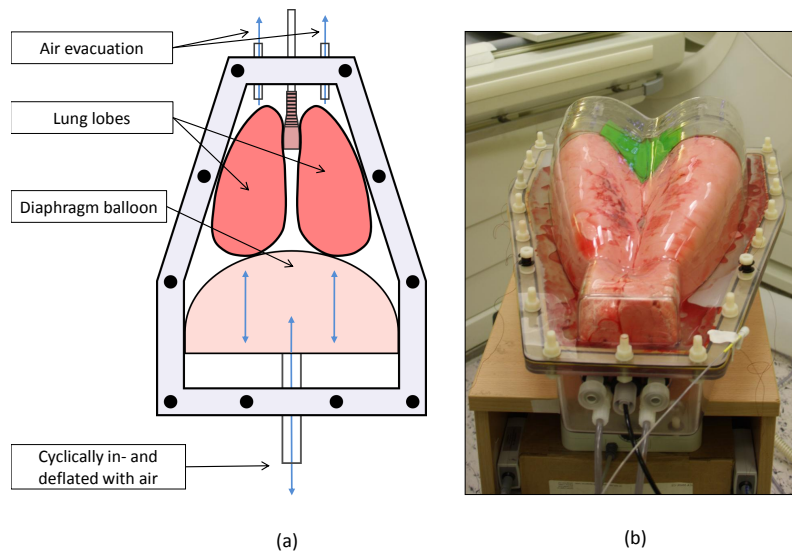

FIGURE 4.18.: **ArtiChest thorax phantom: a) schematic of design and operation, and b) setup with inflated lung and bronchoscope inserted through trachea.**

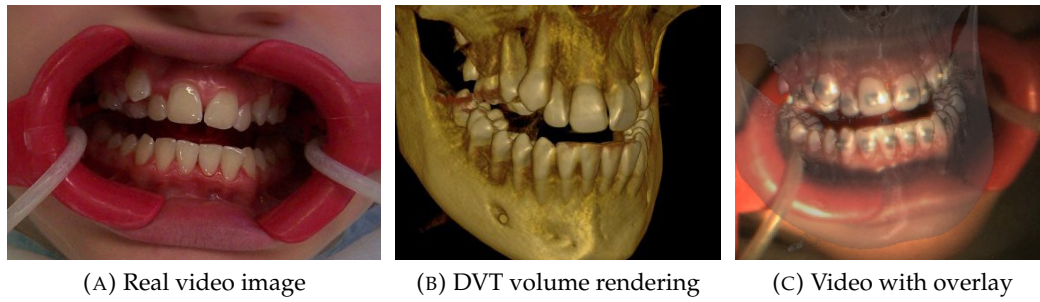(A) Real video image   (B) DVT volume rendering   (C) Video with overlay

FIGURE 4.19.: **Real video image of a prepared patient (4.19a), a high-quality volume rendering of the jaw from a DVT volume of the same patient (4.19b), and rendering of the DVT volume overlaid on the real image (4.19c).**

smoothness is enforced. Also, our method does not impose any assumptions on the breathing motion, which can be irregular and interrupted by coughing or choking, depending on the degree of patient sedation. Thus, data acquisition can be brought to the operating room with minimal interruption to the surgical workflow.

4.3.2. Advanced Image Registration

Conflicting requirements of robustness, speed, and accuracy for image-based tracking may not be met using a single approach. Thus, advanced application-specific image rendering and registration techniques are introduced, which approach these requirements in a complementary process.

In the following we outline an application-specific solution for image-based tracking by registration of video images with computed tomography (CT) data [Aich 12].

Up to now, orthodontic applications like bracket placement rely solely on the dentist's experience, but in the future Augmented Reality (AR) applications might help planning optimal placement and executing such procedures. A light-weight head-mounted display can be used for this. External tracking systems could be used, but integrating them into clinical routine and workflow requires significant effort. In addition, the multitude of calibrations involved (patient-tracking, tracking-visualisation, etc.) would quickly accumulate error. In contrast, tracking the pose of the patient relative to the surgeon directly in the video image elegantly avoids the accumulation of errors and the need for an external tracking system. This yields a light-weight solution, which can be integrated quickly into clinical routine, without the need for a full-scale medical AR set-up. Low-dose X-ray Digital Volume Tomography (DVT) images are usually available, so the video images may be registered to these and overlays displayed, as shown in Figure 4.19. There are conflicting requirements of robustness (large capture range), speed, and accuracy. It is not possible to meet all these requirements in a single approach, so two complementary methods were devised.

The scene is mostly texture-less, and for the sake of integration into the workflow, it is not desirable to augment the scene with artificial markers. This leaves edge-based registration [Klei 06] as the method of choice for the first step. Since the most dominant and stable
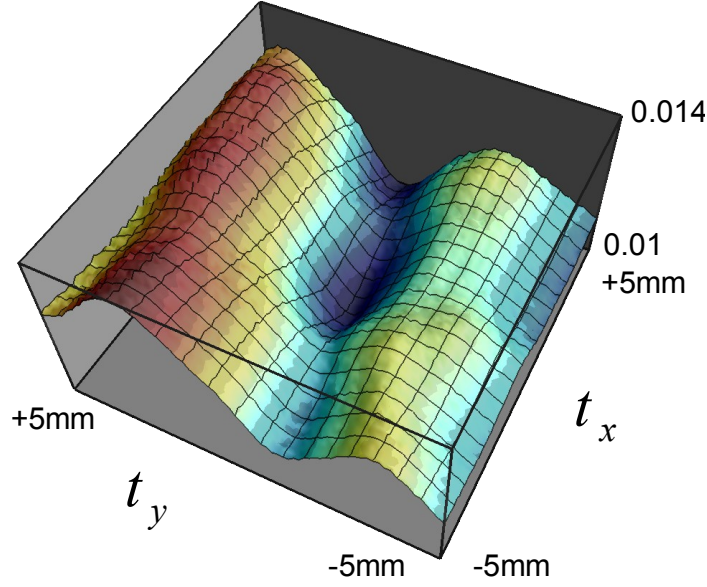
FIGURE 4.20.: **Plot of the edge-based distance metric** d **for translations parallel to the image plane with a clear minimum for perfect visual alignment at the centre.**

edges in the video image are those of the teeth and gum-line, i.e. the objects of interest themselves, a two-step dual iso-surface rendering algorithm was developed for the DVT images, which distinguishes between teeth surfaces covered by gum or not [Aich 12]. For the registration of a single frame, the video image is subjected once to a Canny edge filter [Cann 86], and a distance map is computed. Then, in a numerical optimisation loop the virtual image is rendered, the image gradient is computed, and via a fast look-up into the distance map the distance to the closest edge is computed. The distance measure in the edge-based registration is

$$d = \frac{\sum\limits_{x,y} [d(x,y) \cdot g(x,y)]}{\sum\limits_{x,y} g(x,y)} \tag{4.33}$$

where $d(x,y)$ is the distance map of the video edges, and $g(x,y) = \left\| \nabla_{(x,y)} J \right\|^2$ is the squared image gradient magnitude of the dual iso-surface rendering J at pixel coordinates (x,y). This approach provides accurate results, as shown by a plot of the distance metric in the neighbourhood of the true optimum (Figure 4.20). However, due to the invocation of a rendering step for each evaluation of the cost function, the edge-based registration step is not feasible in real-time. Also, it is desirable to increase the capture range, in order to compensate for quick motions.

Thus, a second texture-based approach was devised, where the video image is projected onto the iso-surface rendered from the DVT volume before. The registration now becomes a mono-modal problem, and a simple, fast similarity measure like the sum of absolute differences (SAD) can be used. This approach is fast and provides a large capture range. The texture-based approach is susceptible to the so-called "template update
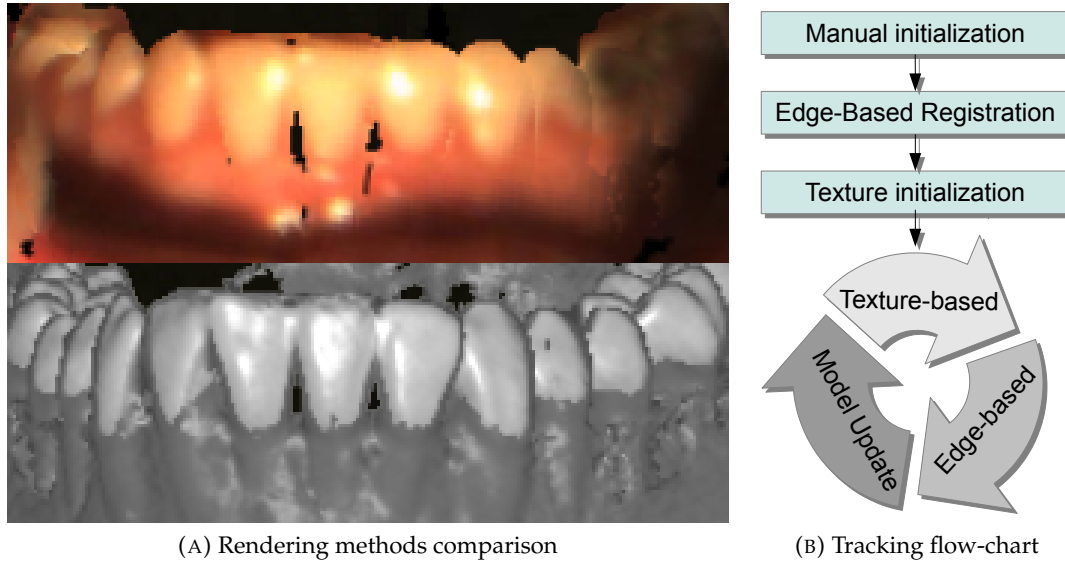
(A) Rendering methods comparison　　　　(B) Tracking flow-chart

FIGURE 4.21.: **Texture-based and iso-surface rendering methods (4.21a), and flow-chart of initialisation and tracking procedure (4.21b).**

problem" [Matt 04], which may lead to accumulation of errors and drift, so the texture is re-initialised from the edge-based approach, when necessary. For a comparison of both rendering methods, and a flow-chart of the complete tracking system, please refer to Figure 4.21.

4.4. Electromagnetic Servoing – A New Automated Tracking Paradigm

In this section we present a novel tracking paradigm, where we keep the electromagnetic tracking sensor always close to the centre of the tracking volume, in order to minimise errors. This is the first general solution providing uniform accuracy throughout the tracking volume, improving accuracy by a factor of two, and at the same time extending the tracking volume up to the reach of the robot. [2]

Non-Uniform Accuracy: The accuracy of electromagnetic (EM) tracking is not uniform throughout the tracking volume, as shown in Figure 4.22a. In previous tracking system benchmarks the accuracy has already been recognised as usually being highest close to the centre of the tracking volume, as shown in Figure 4.22b. This is due to internal calibration of the tracking system, and indicates the trade-off between tracking accuracy and tracking volume size.

Thus, if tracking sensors are kept close to this centre, accuracy will be optimal. However, this implies that the EM field generator needs to follow movement of the sensor, and thus needs to be tracked itself. Since such a feedback loop would be hard to implement

---

[2]For a revised version of this section, please refer to the subsequent publication. [Reic 13a]
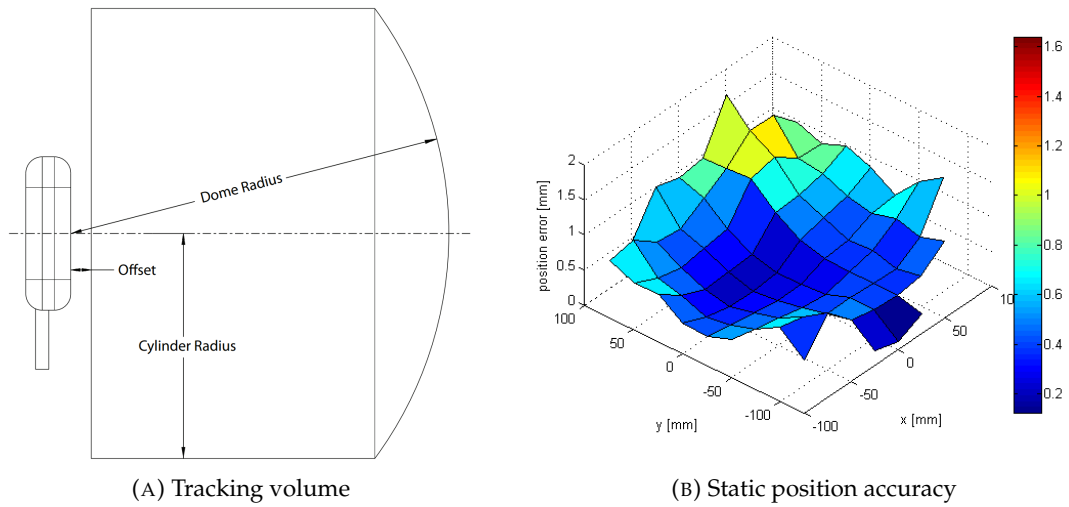
(A) Tracking volume

(B) Static position accuracy

FIGURE 4.22.: **Tracking volume and accuracy of a compact field generator for the Aurora tracking system (Northern Digital). 4.22a) Tracking volume, where volume offset is 10 mm, cylinder radius is 110 mm, and dome radius is 185 mm [Nort 11]. 4.22b) Typically bowl-shaped plot of static tracking position accuracy, with mean errors computed in the z direction.**

manually, it is a direct consequence to use a robot for automated movement of the field generator. In addition, the robot also provides the required pose information about field generator movement. Such *electromagnetic servoing* results in uniform, optimal EM tracking accuracy, only diminished by robotic relative accuracy, which is usually negligible in comparison. As an additional benefit, the effective tracking volume is increased, and the robot may rotate the field generator around the sensor, if required by the application, or in order to avoid a suboptimal sensor orientation relative to the field generator [Shen 08].

Set-Up: Our set-up (cf. Figure 4.23) consists of a six-axis robotic arm (UR-6-85-5-A, Universal Robots, Odense, Denmark, stated accuracy 0.1 mm) and an EM tracking system (Aurora, Northern Digital, Waterloo, ON, Canada) with a compact field generator (stated accuracy 0.6 mm). For evaluation purposes we also use an optical tracking system (Polaris Vicra, Northern Digital, stated accuracy 0.25 mm).

In order to avoid distortions of the EM tracking field, the field generator was fixed to the robot hand using a custom-designed spacer made of biocompatible DuraForm PA plastic (3D Systems, Rock Hill, SC, USA), which is shown in Figure 4.24b. For evaluation three EM sensors were fixed in orthogonal orientations to a holder made of the same material, as shown in Figure 4.24a. Two non-metallic optical tracking targets were attached to both the EM field generator and to the EM sensors.

It can be derived from theoretical considerations that secondary EM fields from any metallic object, whose distance from the EM field generator is at least twice the distance between EM field generator and sensor, contributes less than one per cent to the measured field strength [Raab 79]. Since our goal is to track an object at the center of the tracking volume, the distance between EM field generator and sensor is kept at approximately 95 mm.
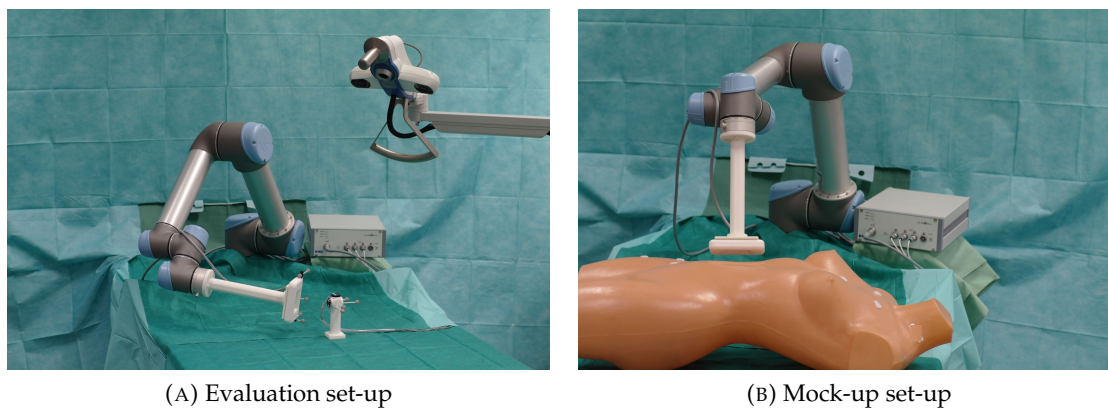
(A) Evaluation set-up   (B) Mock-up set-up

FIGURE 4.23.: **4.23a) Evaluation set-up for electromagnetic servoing, arranged for display purposes. 4.23b) Mock-up set-up for tracking during abdominal intervention.**

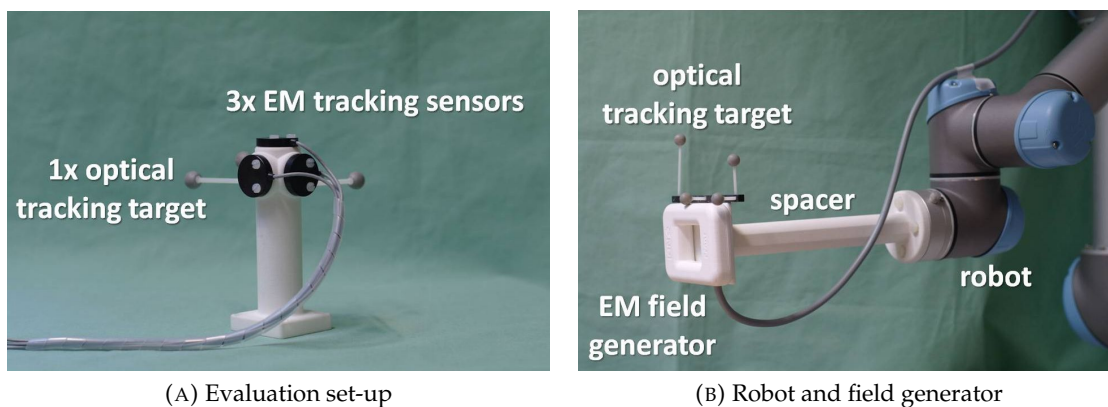(A) Evaluation set-up   (B) Robot and field generator

FIGURE 4.24.: **EM sensors and EM field generator attached to robot. 4.24a) EM sensors are mounted in orthogonal orientations, with an optical tracking target for evaluation. 4.24b) The EM field generator is attached to the robot, and also equipped with an optical tracking target for evaluation.**

Thus, a spacer of 220 mm length between robot and EM field generator is sufficient to avoid EM distortions from metals in the robot.

Polyamide screws were used in the vicinity of the EM field generator and EM sensors. Evaluations were performed over a metal-free table, with as much distance from other electrical equipment (computers, power supplies, lamps, etc.) as possible.

Hand-Eye Calibration: We performed hand-eye calibration as described in section 3.3. Measurements during a sequence of motions can be rewritten as $AX = XB$, where A in our case is the measured motion of the EM field generator relative to a fixed sensor, B is the motion of the robot hand relative to the robot base, and $X = {}^{H}\mathbf{T}_F$ is the transformation from the EM field generator to the robot hand. Motions were chosen following Tsai's and Lenz' recommendations for optimal accuracy [Tsai 89].

Choosing appropriate input motions for the hand-eye calibration algorithm (cf. section 3.3), it is possible to compute all fixed transformations in our set-up. We are interested in the transformation matrix ${}^{H}\mathbf{T}_F$ from the EM field generator (F) to the robot hand (H), and in the transformation ${}^{T}\mathbf{T}_S$ from the EM sensors (S) to the optical tracking target (T). The latter is only relevant for determining ground truth for evaluation, and our set-up does indeed not depend on optical tracking.

Hand-eye calibration is fully automated and takes only seconds to perform. In 54 repetitions of the hand-eye calibration procedure, the results for the transformation ${}^{H}\mathbf{T}_F$ from field generator to robot hand had a mean deviation from their mean of 1.91 mm and 2.55°.

Feedback Loop and EM-Servoing: In order to keep the EM sensor at the centre of the tracking volume, its position is constantly monitored via EM tracking. Whenever its distance from a preselected, relative position is larger than a specified threshold, the required translation ${}^{\acute{F}}\vec{\mathbf{t}}_F$ of the field generator is computed. Then the robot hand pose is updated as

$$ {}^{B}\acute{\mathbf{T}}_H = {}^{B}\mathbf{T}_H \cdot {}^{H}\mathbf{T}_F \cdot \begin{bmatrix} I & {}^{\acute{F}}\vec{\mathbf{t}}_F \\ 0 & 1 \end{bmatrix} \cdot \left({}^{H}\mathbf{T}_F \right)^{-1}, \tag{4.34} $$

where ${}^{B}\mathbf{T}_H$ is the previous transformation from robot hand to base and ${}^{H}\mathbf{T}_F$ is the transformation from the field generator to the robot hand. The new hand pose ${}^{B}\acute{\mathbf{T}}_H$ is then sent to the robot and executed.

This method does not depend on any particular preselected position within the tracking volume, nor on a specific motion threshold, and the volume centre and a threshold of 20 mm were chosen only as proof-of-concept.

Static Accuracy Evaluation: In order to verify that our proposed set-up including the robot did not negatively influence tracking accuracy, we measured static accuracy. Here, one object was simultaneously tracked by EM and optical tracking systems. In particular we used three sensors mounted in mutually orthogonal orientations, in order not to favour a specific orientation of the sensor with respect to the EM field (cf. Figure 4.24a). There have been numerous works benchmarking EM tracking systems, e.g. [Humm 05, Yani 09, Gerg 12], and we employ a standard methodology for evaluation of our set-up.

The scanning volume was defined according to the field generator specifications (cf. Figure 4.22) and transformed into robot coordinates using hand-eye calibration results. The sensors remained static, while the field generator was moved through the tracking volume without changing the orientation of field generator or sensors. The volume was sampled on a regular 3-D grid with a spacing of 25 mm, at each measurement position the robot was stopped for one second, in order to avoid vibrations, and 10 samples were recorded at each position and averaged.

Optical tracking was used as ground truth, and since the relative orientation between sensors and field generator was constant, it is possible to directly compute a transformation $^E\mathbf{T}_O$ between point coordinates $\mathbf{p}_{O,i}$ from optical tracking (O) and point coordinates $\mathbf{p}_{E,i}$ from EM tracking (E) as

$$\underset{^E\mathbf{T}_O}{\arg\min}\left[\frac{1}{N}\sum_{i=1}^{N}\left\|\mathbf{p}_{E,i} - {}^E\mathbf{T}_O \cdot \mathbf{p}_{O,i}\right\|^2\right] \tag{4.35}$$

Position errors can then be computed as distance between original points $\mathbf{p}_{E,i}$ and transformed points $\mathbf{p}_{O,i}$. The orientation error was computed as the mean deviation from the average measured orientation, since the true orientation of both the sensors and the field generator remained constant.

Only a subset of measurements was used for point-based registration. For optimal registration we picked the 10% of measurement points with best signal quality (quality as reported by the tracking system), since this ratio seems to avoid both over- and underestimation. If too few points are used for point-based registration (or if these points' accuracy is worse than average), measurement errors in these points may lead to an overestimation of errors for the remaining points. However, if too many points are used, this may lead to an underestimate, since the same errors are minimised during registration.

In five separate experiments on three different days we measured a mean static position error between 0.54 and 0.68 mm, and a mean static orientation error between 0.49 and 0.67°, as shown in Figure 4.25. This agrees with the specified accuracy for the EM tracking system (0.6 mm and 0.8°). This also confirms that the robot does not adversely influence tracking accuracy.

Dynamic Accuracy Evaluation: In order to evaluate the accuracy of electromagnetic servoing, we moved the EM sensors by hand, while the robot was following one of the sensors. Whenever this sensor was detected more than 20 mm away from the centre of the tracking system, the robot would move accordingly and re-focus on the sensor. EM tracking measurements $^F\mathbf{T}_S$ were transformed into the robot base coordinate system (B) as

$$^B\mathbf{T}_S = {}^B\mathbf{T}_H \cdot {}^H\mathbf{T}_F \cdot {}^F\mathbf{T}_S, \tag{4.36}$$

where $^B\mathbf{T}_H$ is the current robot hand pose and $^H\mathbf{T}_F$ is the calibrated transformation from EM field generator to robot hand. For comparison to the traditional set-up with a fixed field generator, in another type of experiment the robot remained *static*, while measurements were recorded. Both cases were evaluated against optical tracking as ground truth data.

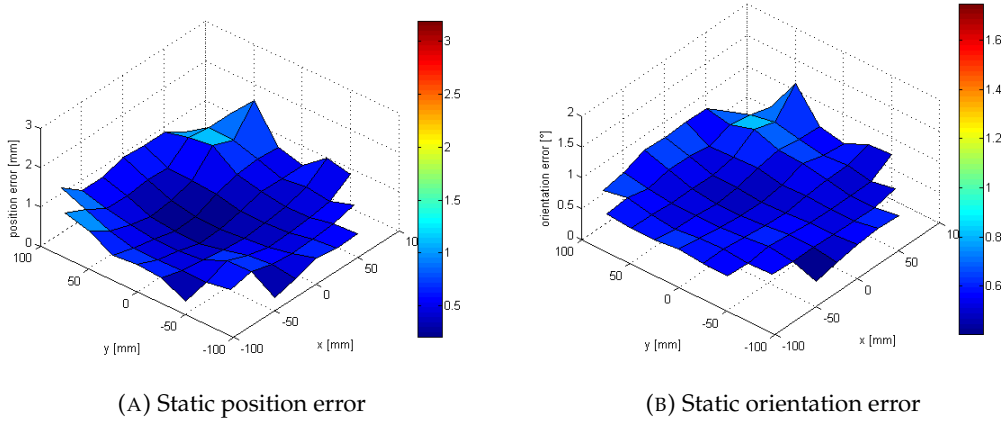(A) Static position error   (B) Static orientation error

FIGURE 4.25.: **Static position (4.25a) and orientation errors (4.25b) of our set-up, with mean errors computed in the z direction.**

Since in the general case the rotation between the EM sensors and field generator is not constant, we need to transform the measurements into fixed coordinate systems first. The EM tracking measurements were already transformed into robot coordinates, cf. equation 4.36. From hand-eye calibration the positions $^T\mathbf{T}_S$ of the EM sensors to the tracking target are known and can be transformed to the fixed optical tracking coordinate system (O) using optical tracking measurements $^O\mathbf{T}_T$ as

$$^O\mathbf{T}_S = {}^O\mathbf{T}_T \cdot {}^T\mathbf{T}_S. \tag{4.37}$$

Then again, point-based registration with the EM measurements was performed and position errors were computed. Measurements were performed four times with a moving field generator, and four times with a static field generator, yielding between 11200 and 29600 samples per experiment, each consisting of measurements for all EM sensors and optical targets as well as the robot.

The mean errors determined in each experiment were {2.23, 5.35, 2.43, 2.55} mm, when the field generator was moving, and {10.60, 3.51, 6.11, 2.78} mm, when the field generator was static. *Thus, the proposed method was able to reduce the overall error from* 5.75 ± 3.54 *mm to* 3.14 ± 1.48 *mm.* The accuracy distribution over the tracking volume is shown in Figure 4.26.

The particular robot in our set-up is rather low-cost and was only used as proof of concept. With a more advanced robot, several issues could be avoided. E.g. there was no suitable real-time interface available, and there was considerable lag before commands were executed (up to 600 ms). Thus, the robot was only able to follow the tracked object at slow speeds, but this could be remedied with a real-time interface. Also, the robot currently used is rather heavy (18 kg weight, 5 kg payload), and for better integration into clinical environment and workflow it could easily be replaced with a more lightweight robot, since the EM field generator weighs only 120 grams.

Following the considerations above regarding distance from metals, a set-up like the proposed is potentially more robust against influences from operating room (OR) tables or similar than set-ups with larger field generators. Such influences will usually be twice
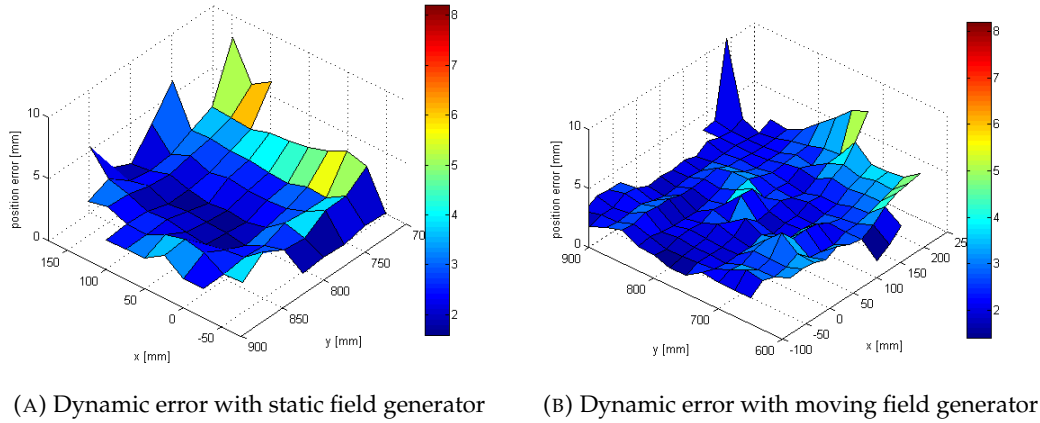
(A) Dynamic error with static field generator   (B) Dynamic error with moving field generator

FIGURE 4.26.: **Dynamic position errors of set-up with static and moving field generator. Traditional set-up with static field generator (4.26a) and proposed set-up with moving field generator (4.26b) are shown, with mean errors computed in the z direction. Please note that the proposed method provides uniform errors across the tracking volume, while the traditional set-up shows the typical bowl shape.**

as far from the field generator as the sensors, and thus will have less influence on the EM field. Also, metal-free OR tables with carbon fibre tops are already used for intra-operative C-arm imaging.

During the dynamic acquisition, EM-robotic and optical tracking measurements were acquired with changing orientation in different reference frames. Thus, orientation error computation is not trivial and inevitably requires a calibrated transformation between those frames. The calibration error would strongly bias an error measure towards an over-estimate.

In contrast to previous works concerning hybrid EM-optical tracking [Birk 98b, Naka 08a, Fran 11], we do not only provide a larger effective tracking volume and relocation ability of the EM field generator, but we are also able to maintain the optimal level of accuracy throughout the tracking volume, otherwise only obtained close to the tracking volume centre.

We presented a novel and general solution for improving EM tracking accuracy. Mounting an EM field generator onto a robotic arm is a new automated tracking paradigm. We have shown the feasibility of the set-up, and in a thorough accuracy evaluation we have shown that the accuracy can significantly be improved from 5.75 ± 3.54 mm to 3.14 ± 1.48 mm. Thus, the proposed method promises application to a wide range of clinical procedures.

5. Outlook and Conclusion

In our final chapter, we will show how such concepts for advanced hybrid tracking might be applied for a novel intra-operative functional imaging modality.

5.1. Tracking Challenges in Endoscopic Time-of-Flight PET & US

Pancreatic cancer is one of the most deadly cancers, with an extremely low five-year survival rate of less than five percent [Jema 08]. In particular, pancreatic cancer is usually detected late, and if detection could be improved by only six months compared to current clinical diagnosis (where the majority of patients is still asymptomatic), this will have great impact on resectability [Char 07].

Functional imaging like positron emission tomography (PET) can be useful in screening for high-risk patients, e.g. with chronic pancreatitis [Kouw 05]. However, diagnostic abilities are limited by the achievable imaging resolution, which in turn is limited by the sensitivity of the imaging system. There have been approaches towards better sensitivity and higher signal-to-noise ratio by bringing detectors closer to the region of interest, i.e. by using dedicated, smaller scanners for the prostate [Hube 06], high-resolution inserts within conventional PET scanners [Park 07], or even transrectal PET probes [Tai 05, Gari 10, Maje 10]. However, no such approaches have been targeting pancreatic cancer so far.

The main clinical objective of the "Endoscopic Time-of-Flight PET and Ultrasound" project (EndoTOFPET-US, European Union, FP7-Health grant n°256984) is "a miniaturised bimodal endoscopic probe with a millimetre spatial resolution and a 100 times higher sensitivity than whole-body PET scanners".

Detector Design: The preliminary design of this endoscopic probe is shown in Figure 5.1a: A commercial ultrasound (US) endoscope is equipped with a PET detector. In order to capture both photons from the annihilation event, and thus establish coincidences, a second detector plate is needed outside the patient, as shown in Figure 5.2b.

During the endoscopic examination, the endoscope is navigated to the region of interest with US guidance, and the pancreas can then be examined using US imaging through the stomach wall (pancreas body and tail), or through the duodenum wall (pancreas head). In order to be able to pass the duodenal bulb, the endoscopic PET detector will be mounted at the endoscope with one degree of freedom.

Signals from both PET detectors, and position information for both detectors, are then used to reconstruct the 3-D radioactivity distribution in the region of interest.

Challenges: In such a highly dynamic detector set-up, tracking accuracy directly affects image reconstruction. According to semi-empirical models of PET imaging, the image
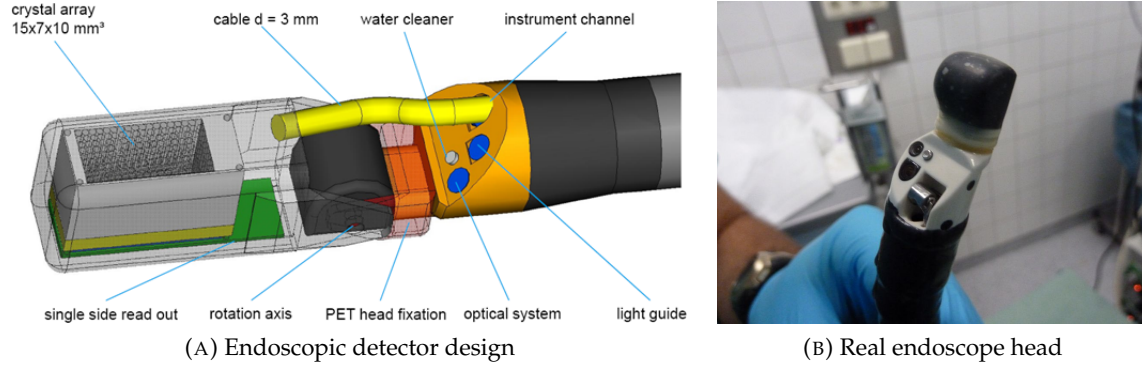
(A) Endoscopic detector design

(B) Real endoscope head

FIGURE 5.1.: **Endoscopic TOF-PET detector and ultrasound probe. 5.1a) Details of EndoTOFPET-US detector details, electromagnetic tracking sensors are not shown. Please note that the PET detector may rotate around the rotation axis, in order to pass the duodenal bulb. 5.1b) Close-up picture of Olympus GF UTC140-AL5 endoscopic ultrasound probe. Images courtesy of Karsten Gadow.**

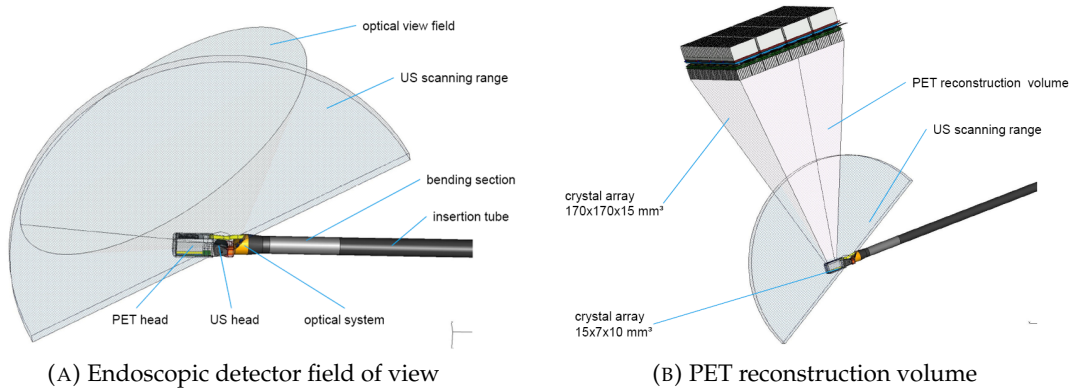
(A) Endoscopic detector field of view

(B) PET reconstruction volume

FIGURE 5.2.: **Field of view and PET reconstruction volume. 5.2a) Field of view (ultrasound and video) of the endoscopic detector. 5.2b) PET reconstruction volume between both parts of the EndoTOFPET-US detector. Note that the reconstruction volume is mostly limited by the size of the endoscopic detector. Images courtesy of Karsten Gadow.**

resolution Γ can be estimated [Dere 93] as

$$\Gamma = 1.25 \cdot \sqrt{(d/2)^2 + (0.0022 \cdot D)^2 + r^2 + b^2}, \tag{5.1}$$

where d is the crystal (pixel) size, D is the detector array diameter, r is the effective positron range, and b is the systematic error of the positioning scheme. Thus, the positioning inaccuracy b has even more influence on imaging resolution as e.g. crystal size d has. Noise or uncertainty in the assumed position of the detectors will lead to blur, and systematic errors will lead to distortions of the reconstructed image. Breathing and other patient motion need to be compensated for, in order to avoid motion blur. Also, it will be beneficial to use pre-operative computed tomography (CT) data for attenuation correction, but this requires precise tracking relative to the patient.

The different parts of the pancreas will need to be imaged from different positions – from the stomach for pancreas body and tail, and from the duodenum for pancreas head. Therefore, and in order to achieve as much depth resolution as possible, the detector set-up will need to rotate around the region of interest, keeping it within the reconstruction volume between the two detectors. This implies automated and highly flexible motion of the outer detector plate, mirroring motion of the endoscopic detector. On the other hand, robotic motion will provide high accuracy position information for the outer detector plate.

5.2. Conclusion

Only a decade ago, tracking of a flexible instrument in an abdominal setting with such a high accuracy might have been dismissed as impossible. However, in line with the previous chapters, the following considerations may lead to novel solutions within the next years:

First, the PET detector will be mounted at the endoscope with one degree of freedom. Thus, in order to capture its motion relative to the video and US imaging devices, motion models will be needed (as presented in section 4.1), and redundant tracking information will be employed for tracking error detection and correction.

Second, in order to track patient movement, or movement of the detector relative to the patient, video and ultrasound (US) images from the endoscope will be used. Similar to 2-D/3-D registration between video images and a pre-operative CT volume (as presented in section 4.3), registration between US and CT can be performed [Wein 07]. However, in contrast to e.g. abdominal US the endoscopic field of view is very small, only few centimetres. Thus, it will be important to have a sufficiently accurate initial estimate.

Finally, electromagnetic tracking alone will not be sufficient to achieve the required accuracy. However, the accuracy of electromagnetic tracking may be improved, when combined with robotic motion for electromagnetic servoing (as presented in section 4.4) in a novel tracking paradigm. We presented the first general solution providing uniform tracking accuracy throughout the volume, improving tracking accuracy by a factor of two, and at the same time extending the tracking volume up to the reach of the robot.

Of course, even though based on the current state on the art, these considerations are optimistic, and the challenge of accurate intra-operative tracking will remain an interesting research subject for years to come.

Appendix

A. Other Major Contributions

A.1. Real-time Ultrasound Simulation from Computed X-Ray Tomography

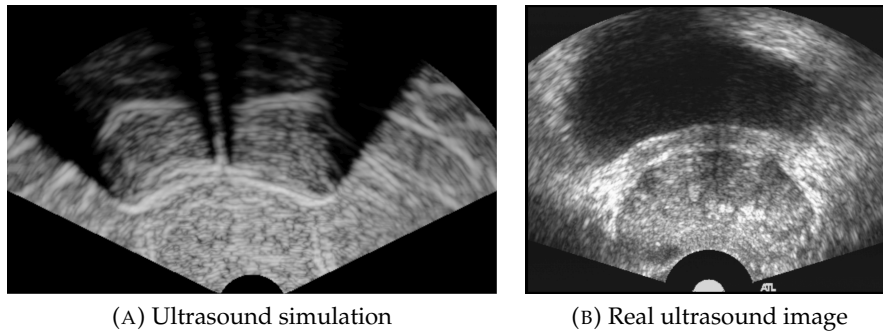(A) Ultrasound simulation   (B) Real ultrasound image

FIGURE A.1.: **Ultrasound simulation and real transrectal ultrasound image. Screen shot of our simulation (A.1a), and similar image from a real transrectal ultrasound examination of a different patient (A.1b).**

Tobias Reichl, Josh Passenger, Oscar Acosta, and Olivier Salvado

[Reic 09] Despite the increasing adoption of other imaging modalities, ultrasound guidance is widely used for surgical procedures and clinical imaging due to its low cost, non-invasiveness, real-time visual feedback. Many ultrasound-guided procedures require extensive training and where possible training on simulations should be preferred over patients. Computational resources for existing approaches to ultrasound simulation are usually limited by real-time requirements. Unlike previous approaches we simulate free-hand ultrasound images from CT data on the Graphics Processing Unit (GPU). We build upon the method proposed by Wein *et al.* for estimating ultrasound reflection properties of tissue and modify it to a computationally more efficient form. In addition to previous approaches, we also estimate ultrasound absorption properties from CT data. Using NVIDIA's Compute Unified Device Architecture (CUDA), we provide a physically plausible simulation of ultrasound reflection, shadowing artefacts, speckle noise and radial blurring. The same algorithm can be used for simulating either linear or radial imaging, and all parameters of the simulated probe are interactively configurable at run-time, including ultrasound frequency and intensity as well as field geometry. With current hardware we are able to achieve an image width of up to 1023 pixels from raw CT data in real-time, without any pre-processing and without any loss of information from the CT image other than from interpolation of the input data.

A.2. Optimisation of Acquisition Geometry for Intra-Operative Tomographic Imaging
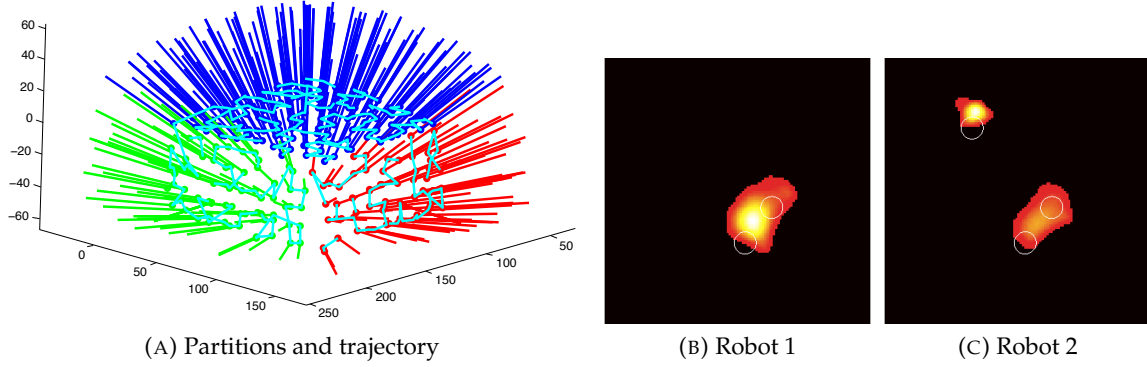

(A) Partitions and trajectory   (B) Robot 1   (C) Robot 2

FIGURE A.2.: **Acquisition locations and robot trajectory and reconstruction results. A.2a) View through the (invisible) region of interest towards three measured planes, with partitioned acquisition locations and robot trajectory. A.2b–A.2c) Results of two *real* acquisitions performed by a robot following a trajectory created by our method, with ground truth spheres overlaid.**

Jakob Vogel, Tobias Reichl, Nassir Navab, and Tobias Lasser

[Voge 12] Acquisition geometries for tomographic reconstruction are usually densely sampled in order to keep the underlying linear system used in iterative reconstruction as well–posed as possible. While this objective is easily enforced in imaging systems with gantries, this issue is more critical for intra–operative set-ups using freehand–guided data sensing. This paper investigates an incremental method to monitor the numerical condition of the system based on the singular value decomposition of the system matrix, and presents an approach to find optimal detector positions via a randomised optimisation scheme. The feasibility of this approach is demonstrated using simulations of an intra–operative functional imaging setup and actual robot–controlled phantom experiments.

A.3. Flexible Robotic Intra-Operative Nuclear Imaging for Image-Guided Surgery

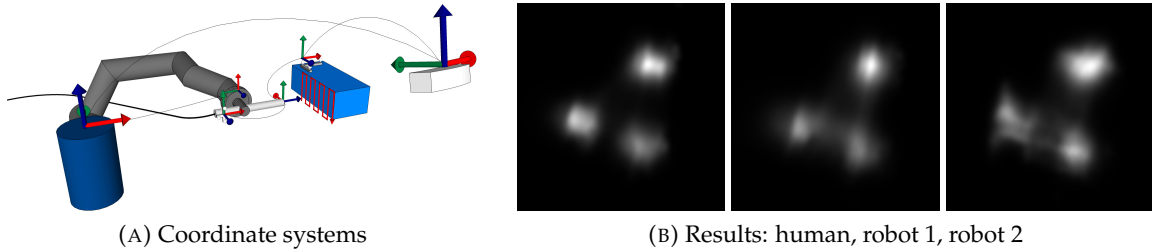(A) Coordinate systems

(B) Results: human, robot 1, robot 2

FIGURE A.3.: **Coordinate systems in the robot set-up and reconstruction results. A.3a) Coordinate systems involved in the set-up: robot base, robot hand, probe target, probe tip, phantom target and optical tracking system. A.3b) Reconstruction results of (from left) human operator, robot following human path, and robot following synthetic path.**

José Gardiazabal, Tobias Reichl, Philipp Matthies, Aslı Okur, Jakob Vogel, Sibylle I. Ziegler, Tobias Lasser, and Nassir Navab

[Gard 13] Functional imaging systems for intra-operative use, like freehand SPECT, have been successfully demonstrated in the past, with remarkable results. These results, even though very positive in some cases, tend to suffer from high variability depending on the expertise of the operator. A well trained operator can produce datasets that will lead to a reconstruction that can rival a conventional SPECT machine, while an untrained one will not be able to achieve such results. In this paper we present (to our knowledge) the first flexible robotic functional imaging set-up for intra-operative use, replacing the operator in the scanning process with a robotic arm. The robot can assure good coverage of the area of interest, thus producing a consistent scanning pattern that can be reproduced with high accuracy, and provides the option to compensate for radioactive decay. We show first results on phantoms demonstrating the feasibility of the set-up to perform 3-D nuclear imaging suitable for the operating room.

B. Authored and Co-Authored Publications

[Aich 12]   A. Aichert, W. Wein, A. Ladikos, T. Reichl, and N. Navab. "Image-based tracking of the teeth for orthodontic augmented reality". In: *Proceedings of Int'l Conference on Medical Image Computing and Computer-Assisted Intervention (MICCAI)*, 2012. To appear.

[Dres 10]   P. Dressel, M. Feuerstein, T. Reichl, T. Kitasaka, N. Navab, and K. Mori. "Direct co-calibration of endobronchial ultrasound and video". In: *Proc. Int'l Workshop on Medical Imaging and Augmented Reality (MIAR)*, pp. 513–520, Springer Berlin / Heidelberg, 2010.

[Feue 07]   M. Feuerstein, T. Reichl, J. Vogel, A. Schneider, H. Feussner, and N. Navab. "Magneto-optic tracking of a flexible laparoscopic ultrasound transducer for laparoscope augmentation". In: *Proceedings of Int'l Conference on Medical Image Computing and Computer-Assisted Intervention (MICCAI)*, p. 909, Springer Berlin / Heidelberg, November 2007.

[Feue 08]   M. Feuerstein, T. Reichl, J. Vogel, J. Traub, and N. Navab. "New approaches to online estimation of electromagnetic tracking errors for laparoscopic ultrasonography". *Computer Assisted Surgery*, Vol. 13, pp. 311–323, September 2008.

[Feue 09]   M. Feuerstein, T. Reichl, J. Vogel, J. Traub, and N. Navab. "Magneto-optical tracking of flexible laparoscopic ultrasound: model-based online detection and correction of magnetic tracking errors". *IEEE Transactions on Medical Imaging*, Vol. 28, No. 6, pp. 951–967, June 2009.

[Feue 10]   M. Feuerstein, T. Sugiura, D. Deguchi, T. Reichl, T. Kitasaka, and K. Mori. "Marker-free registration for electromagnetic navigation bronchoscopy under respiratory motion". In: *Proc. Int'l Workshop on Medical Imaging and Augmented Reality (MIAR)*, pp. 237–246, Springer Berlin / Heidelberg, 2010.

[Gard 13]   J. Gardiazabal, T. Reichl, A. Okur, T. Lasser, and N. Navab. "First flexible robotic intra-operative nuclear imaging for image-guided surgery". In: *International Conference on Information Processing in Computer Assisted Interventions (IPCAI)*, Heidelberg, Germany, June 2013. To appear.

[Luo 10a]   X. Luo, M. Feuerstein, T. Reichl, T. Kitasaka, and K. Mori. "An application driven comparison of several feature extraction algorithms in bronchoscope tracking during navigated bronchoscopy". In: *Proc. Int'l Workshop on Medical Imaging and Augmented Reality (MIAR)*, 2010.

[Luo 10b]   X. Luo, T. Reichl, M. Feuerstein, T. Kitasaka, and K. Mori. "Modified hybrid broncho-scope tracking based on sequential Monte Carlo sampler: dynamic phantom validation". In: *Asian Conference on Computer Vision*, pp. 409–421, Queenstown, New Zealand, November 2010.

[Mori 11]   K. Mori, T. Kugo, X. Luo, P. Dressel, T. Reichl, M. Feuerstein, N. Navab, and T. Kitasaka. "Endobronchial ultrasound endoscope navigation system based on CT-US calibration". In: *Proceedings of Int'l Congress on Computer Assisted Radiology and Surgery (CARS) Workshop on NOTES: An Interdisciplinary Challenge*, 2011.

[Reic 09a]   T. Reichl, J. Passenger, O. Acosta, and O. Salvado. "Echtzeit-Ultraschallsimulation auf Grafik-Prozessoren mit CUDA". In: *Proceedings of Bildverarbeitung für die Medizin (BVM)*, pp. 157–161, Springer Berlin / Heidelberg, 2009.

[Reic 09b] T. Reichl, J. Passenger, O. Acosta, and O. Salvado. "Ultrasound goes GPU: real-time simulation using CUDA". In: M. I. Miga and K. H. Wong, Eds., *Proceedings of SPIE Medical Imaging 2009: Visualization, Image-Guided Procedures, and Modeling*, p. 726116, February 2009.

[Reic 10] T. Reichl, O. Kutter, B. Schultis, M. Menzel, H. Hautmann, and N. Navab. "Video-basiertes Tracking eines Bronchoskops". In: *Proceedings of Bildverarbeitung für die Medizin (BVM)*, pp. 410–414, Springer Berlin / Heidelberg, Aachen, Germany, 2010.

[Reic 11] T. Reichl, X. Luo, M. Menzel, H. Hautmann, K. Mori, and N. Navab. "Deformable registration of bronchoscopic video sequences to CT volumes with guaranteed smooth output". In: *Proceedings of Int'l Conference on Medical Image Computing and Computer-Assisted Intervention (MICCAI)*, pp. 17–24, Springer Berlin / Heidelberg, Toronto, Canada, September 2011.

[Reic 12a] T. Reichl, I. Gergel, M. Menzel, H. Hautmann, I. Wegner, H.-P. Meinzer, and N. Navab. "Real-time motion compensation for EM bronchoscope tracking with smooth output – ex-vivo validation". In: *Proceedings of SPIE Medical Imaging 2012: Image-Guided Procedures, Robotic Interventions, and Modeling*, p. 83163A, SPIE, 2012.

[Reic 12b] T. Reichl, I. Gergel, M. Menzel, H. Hautmann, I. Wegner, H.-P. Meinzer, and N. Navab. "Motion compensation for bronchoscope navigation using electromagnetic tracking, airway segmentation, and image similarity". In: *Proceedings of Bildverarbeitung für die Medizin (BVM)*, pp. 45–50, Springer, Berlin, Germany, 2012.

[Reic 12c] T. Reichl, I. Gergel, M. Menzel, H. Hautmann, I. Wegner, H.-P. Meinzer, and N. Navab. "New methods for tracking error compensation in transbronchial interventions". In: *Proceedings of Int'l Congress on Computer Assisted Radiology and Surgery (CARS)*, 2012.

[Reic 13a] T. Reichl, J. Gardiazabal, and N. Navab. "Electromagnetic servoing – a new tracking paradigm". *IEEE Transactions on Medical Imaging*, 2013. To appear.

[Reic 13b] T. Reichl, X. Luo, M. Menzel, H. Hautmann, K. Mori, and N. Navab. "Hybrid electromagnetic and image-based tracking of endoscopes with guaranteed smooth output". *International Journal of Computer Assisted Radiology and Surgery*, 2013. To appear.

[Voge 12] J. Vogel, T. Reichl, N. Navab, and T. Lasser. "Optimization of Acquisition Geometry for Intra-operative Tomographic Imaging". In: *Proceedings of Int'l Conference on Medical Image Computing and Computer-Assisted Intervention (MICCAI)*, pp. 42–49, Springer Berlin / Heidelberg, Nice, France, October 2012.

C. List of Figures

D. Bibliography

[Abda 09]   R. Abdallah, T. R. Gildea, M. K. Ghanem, M. M. Metwally, M. Machuzac, P. J. Mazzone, A. H. Osman, and A. C. Mehta. "The evolution of electromagnetic navigation bronchoscopy". *Chest*, Vol. 136, No. 4, pp. 85S–c–86, 2009.

[Adva 12]   Advanced Realtime Tracking. "How does optical tracking work?". http://www.ar-tracking.com/technology/optical-tracking/, 2012.

[Aich 12]   A. Aichert, W. Wein, A. Ladikos, T. Reichl, and N. Navab. "Image-based tracking of the teeth for orthodontic augmented reality". In: *Proceedings of Int'l Conference on Medical Image Computing and Computer-Assisted Intervention (MICCAI)*, 2012. To appear.

[Amin 01]   D. Amin, T. Kanade, B. Jaramaz, A. DiGioia, C. Nikou, R. LaBarca, and J. Moody Jr. "Calibration method for determining the physical location of the ultrasound image plane". In: *Proceedings of Int'l Conference on Medical Image Computing and Computer-Assisted Intervention (MICCAI)*, p. 947, Springer Berlin / Heidelberg, 2001.

[Ande 00]   M. E. Anderson, M. S. McKeag, and G. E. Trahey. "The impact of sound speed errors on medical ultrasound imaging". *Journal of the Acoustical Society of America*, Vol. 107, No. 6, pp. 3540–3548, June 2000.

[Aqui 99]   S. L. Aquino and D. J. Vining. "Virtual bronchoscopy". *Clinics in Chest Medicine*, Vol. 20, No. 4, pp. 725–30, vii–viii, December 1999.

[Arms 07]   B. Armstrong, T. Verron, L. Heppe, R. Karonde, J. Reynolds, and K. Schmidt. "RGR-6D: low-cost, high-accuracy measurement of 6-DOF pose from a single image". Manuscript, University of Wisconsin – Milwaukee, 2007.

[Arms 11]   B. S. R. Armstrong. "Orientation dependent radiation source and methods". Patent US 8,059,267, Go Sensors LLC, November 2011.

[Arul 02]   M. Arulampalam, S. Maskell, N. Gordon, and T. Clapp. "A tutorial on particle filters for online nonlinear/non-Gaussian Bayesian tracking". *IEEE Transactions on signal processing*, Vol. 50, No. 2, pp. 174–188, 2002.

[Arun 87]   K. S. Arun, T. S. Huang, and S. D. Blostein. "Least-squares fitting of two 3-D point sets". *IEEE Transactions on Pattern Analysis and Machine Intelligence*, Vol. PAMI-9, No. 5, pp. 698–700, 1987.

[Asce 04]   Ascension. "laserBird 2 specifications". http://www.ascension-tech.com/realtime/laserbird2.php, June 2004.

[Ashe 01]   W. S. Ashe. "Magnetic field permeable barrier for magnetic position measurement system". Patent US 6,246,231, Ascension Technology Corporation, June 2001.

[Ashe 03]   W. Ashe. "Magnetic position measurement system with field containment means". Patent US 6,528,991, Ascension Technology Corporation, March 2003.

[Atas 08]   S. Atasoy, D. P. Noonan, S. Benhimane, N. Navab, and G.-Z. Yang. "A global approach for automatic fibroscopic video mosaicing in minimally invasive diagnosis". In: *Proceedings of Int'l Conference on Medical Image Computing and Computer-Assisted Intervention (MICCAI)*, pp. 850–857, Springer Berlin / Heidelberg, New York, USA, September 2008.

[Bail 03a]   Y. Baillot, J. J. Eliason, G. S. Schmidt, I. Swan, J. E., D. Brown, S. Julier, M. A. Livingston, and L. Rosenblum. "Evaluation of the ShapeTape tracker for wearable, mobile interaction". In: *Proc. IEEE Virtual Reality*, pp. 285–286, 2003.

[Bail 03b]   Y. Baillot, S. J. Julier, D. Brown, and M. A. Livingston. "A tracker alignment framework for augmented reality". In: *Proceedings of IEEE and ACM International Symposium on Mixed and Augmented Reality (ISMAR)*, pp. 142–150, 2003.

[Balt 05]   J. M. Balter, J. N. Wright, L. J. Newell, B. Friemel, S. Dimmer, Y. Cheng, J. Wong, E. Vertatschitsch, and T. P. Mate. "Accuracy of a wireless localization system for radiotherapy". *International Journal of Radiation Oncology*Biology*Physics*, Vol. 61, No. 3, pp. 933 – 937, 2005.

[Baue 04]   M. Bauer, M. Feuerstein, *et al.* "Hand-Eye Calibration". http://campar.in.tum.de/Chair/HandEyeCalibration, 2004.

[Baue 07]   M. A. Bauer. *Tracking errors in Augmented Reality*. PhD thesis, Technische Universität München, München, 2007.

[Besl 92]   P. Besl and H. McKay. "A method for registration of 3-D shapes". *IEEE Transactions on Pattern Analysis and Machine Intelligence*, Vol. 14, No. 2, pp. 239–256, 1992.

[Bigd 12]   A. Bigdelou, L. Schwarz, T. Benz, and N. Navab. "A flexible platform for developing context-aware 3D gesture-based interfaces". In: *Proceedings of the 2012 ACM international conference on Intelligent User Interfaces*, pp. 335–336, ACM, New York, NY, USA, 2012.

[Birk 98a] W. Birkfellner, F. Watzinger, F. Wanschitz, G. Enislidis, M. Truppe, R. Ewers, and H. Bergmann. "Concepts and results in the development of a hybrid tracking system for CAS". In: *Proceedings of Int'l Conference on Medical Image Computing and Computer-Assisted Intervention (MICCAI)*, pp. 343–351, 1998.

[Birk 98b] W. Birkfellner, F. Watzinger, F. Wanschitz, R. Ewers, and H. Bergmann. "Calibration of tracking systems in a surgical environment". *IEEE Transactions on Medical Imaging*, Vol. 17, No. 5, pp. 737–742, October 1998.

[Blac 00]   J. Blackall, D. Rueckert, C. Maurer Jr, G. Penney, D. Hill, and D. Hawkes. "An image registration approach to automated calibration for freehand 3D ultrasound". In: *Proceedings of Int'l Conference on Medical Image Computing and Computer-Assisted Intervention (MICCAI)*, pp. 462–471, Springer Berlin / Heidelberg, 2000.

[Boct 03]   E. Boctor, A. Jain, M. Choti, R. Taylor, and G. Fichtinger. "Rapid calibration method for registration and 3D tracking of ultrasound images using spatial localizer". In: *Proceedings of SPIE Medical Imaging*, p. 521, SPIE, 2003.

[Bors 04]   C. W. Borst. "Tracker calibration using tetrahedral mesh and tricubic spline models of warp". In: *Proc. IEEE Virtual Reality*, pp. 19–26, 2004.

[Bren 04]   B. Brendel, S. Winter, and H. Ermert. "A simple and accurate calibration method for 3D freehand ultrasound". *Biomedizinische Technik*, Vol. 49, No. Suppl. 2, pp. 872–873, 2004.

[Bric 98]   I. Bricault, G. Ferretti, and P. Cinquin. "Registration of real and CT-derived virtual bronchoscopic images to assist transbronchial biopsy". *IEEE Transactions on Medical Imaging*, Vol. 17, No. 5, pp. 703–714, October 1998.

[Brun 06]   G. Brunner and M. Schmid. "Reflector system for determining position". Patent US 7,137,712, Northern Digital Inc., November 2006.

[Cann 86]   J. Canny. "A Computational Approach to Edge Detection". *IEEE Transactions on Pattern Analysis and Machine Intelligence*, Vol. 8, No. 6, pp. 679–698, 1986.

[Catm 74]   E. Catmull and R. Rom. "A class of interpolating splines". *Computer Aided Geometric Design*, pp. 317–326, 1974.

[Char 07]   S. T. Chari. "Detecting early pancreatic cancer: problems and prospects". *Seminars in Oncology*, Vol. 34, No. 4, pp. 284–294, August 2007.

[Chas 98]   F. Chassat and S. Lavallée. "Experimental protocol for accuracy evaluation of 6-D localizers for computer-integrated surgery: Application to four optical localizers". In: *Proceedings of Int'l Conference on Medical Image Computing and Computer-Assisted Intervention (MICCAI)*, p. 277, Springer Berlin / Heidelberg, 1998.

[Chen 06]   T. K. Chen, P. Abolmaesumi, A. D. Thurston, and R. E. Ellis. "Automated 3D freehand ultrasound calibration with real-time accuracy control". In: *Proceedings of Int'l Conference on Medical Image Computing and Computer-Assisted Intervention (MICCAI)*, pp. 899–906, Springer Berlin / Heidelberg, 2006.

[Chen 09] T. K. Chen, A. D. Thurston, R. E. Ellis, and P. Abolmaesumi. "A real-time freehand ultrasound calibration system with automatic accuracy feedback and control". *Ultrasound in Medicine & Biology*, Vol. 35, No. 1, pp. 79–93, January 2009.

[Chin 10] L. Y. Ching, K. Moller, and J. Suthakorn. "Non-radiological colonoscope tracking image guided colonoscopy using commercially available electromagnetic tracking system". In: *IEEE Conference on Robotics Automation and Mechatronics (RAM)*, pp. 62 –67, 2010.

[Chun 04] A. Chung, P. Edwards, F. Deligianni, and G. Yang. "Freehand cocalibration of optical and electro-magnetic trackers for navigated bronchoscopy". In: *Proc. Int'l Workshop on Medical Imaging and Augmented Reality (MIAR)*, pp. 320–328, Springer Berlin / Heidelberg, 2004.

[Clim 04] J. Climent and P. Marés. "Automatic instrument localization in laparoscopic surgery". *Electronic Letters on Computer Vision and Image Analysis*, Vol. 4, No. 1, pp. 21–31, 2004.

[Come 98] R. M. Comeau, A. Fenster, and T. M. Peters. "Integrated MR and ultrasound imaging for im-proved image guidance in neurosurgery". In: K. M. Hanson, Ed., *Proceedings of SPIE Medical Imaging 1998: Image Processing*, pp. 747–754, SPIE, 1998.

[Corn 11] D. C. Cornish and W. E. Higgins. "Real-time method for bronchoscope motion measurement and tracking". In: K. H. Wong and D. R. H. III, Eds., *Proceedings of SPIE Medical Imaging 2011: Visualization, Image-Guided Procedures, and Modeling*, p. 79640M, SPIE, 2011.

[Dani 99a] K. Daniilidis. "Hand-eye calibration using dual quaternions". *International Journal of Robotics Research*, Vol. 18, No. 3, pp. 286–298, 1999.

[Dani 99b] L. Danisch, K. Englehart, and A. Trivett. "Spatially continuous six degree of freedom position and orientation sensor". *Sensor Review*, Vol. 19, No. 2, pp. 10–11, 1999.

[Dari 03] P. Dario, B. Hannaford, and A. Menciassi. "Smart surgical tools and augmenting devices". *IEEE Transactions on Robotics and Automation*, Vol. 19, No. 5, pp. 782–792, 2003.

[Das 85] Y. Das, J. Mcfee, and R. Chesney. "Determination of Depth of Shallowly Buried Objects by Elec-tromagnetic Induction". *IEEE Transactions on Geoscience and Remote Sensing*, Vol. GE-23, No. 1, pp. 60 –66, January 1985.

[Day 00] J. S. Day, D. J. Murdoch, and G. A. Dumas. "Calibration of position and angular data from a magnetic tracking device". *Journal of Biomechanics*, Vol. 33, No. 8, pp. 1039–1045, August 2000.

[De B 07] S. De Buck, F. Maes, A. D´Hoore, and P. Suetens. "Evaluation of a novel calibration technique for optically tracked oblique laparoscopes". In: N. Ayache, S. Ourselin, and A. Maeder, Eds., *Proceed-ings of Int'l Conference on Medical Image Computing and Computer-Assisted Intervention (MICCAI)*, pp. 467–474, Springer-Verlag, Brisbane, Australia, October/November 2007.

[De W 05] W. De Wever, J. Bogaert, and J. A. Verschakelen. "Virtual bronchoscopy: accuracy and usefulness – an overview". *Seminars in Ultrasound, CT, and MRI*, Vol. 26, No. 5, pp. 364–373, October 2005.

[Degu 03] D. Deguchi, K. Mori, Y. Suenaga, J. Hasegawa, J. Toriwaki, H. Takabatake, and H. Natori. "New image similarity measure for bronchoscope tracking based on image registration". In: *Proceed-ings of Int'l Conference on Medical Image Computing and Computer-Assisted Intervention (MICCAI)*, Springer Berlin / Heidelberg, 2003.

[Degu 06] D. Deguchi, K. Akiyama, K. Mori, T. Kitasaka, Y. Suenaga, C. R. Maurer, H. Takabatake, M. Mori, and H. Natori. "A method for bronchoscope tracking by combining a position sensor and image registration". *Computer Aided Surgery*, Vol. 11, No. 3, pp. 109–117, May 2006.

[Degu 07] D. Deguchi, K. Ishitani, T. Kitasaka, K. Mori, Y. Suenaga, H. Takabatake, M. Mori, and H. Na-tori. "A method for bronchoscope tracking using position sensor without fiducial markers". In: *Proceedings of SPIE Medical Imaging*, p. 65110N, SPIE, 2007.

[Deke 05] D. Dekel and C. Gatti. "Video pose tracking system and method". Patent US 6,978,167, Claron Technology Inc., December 2005.

[Deli 04] F. Deligianni, A. Chung, and G.-Z. Yang. "Patient-specific bronchoscope simulation with pq-space-based 2D/3D registration". *Computer Aided Surgery*, Vol. 9, No. 5, pp. 215–226, 2004.

[Dere 93] S. Derenzo, W. Moses, R. Huesman, and T. Budinger. "Critical instrumentation issues for resolu-tion <2 mm, high sensitivity brain PET". In: *Proceedings of PET: Quantification of Brain Function:: Tracer Kinetics and Image Analysis in Brain PET*, p. 25, Elsevier Science & Technology, Akita, Japan, May 1993.

[Ding 03]   M. Ding and A. Fenster. "A real-time biopsy needle segmentation technique using Hough transform". *Medical Physics*, Vol. 30, No. 8, pp. 2222–2233, August 2003.

[Doig 06]   C. Doignon, F. Nageotte, and M. de Mathelin. "Segmentation and guidance of multiple rigid objects for intra-operative endoscopic vision". In: *Proc. of Workshop on Dynamic Vision, European Conference on Computer Vision*, 2006.

[Dres 10]   P. Dressel, M. Feuerstein, T. Reichl, T. Kitasaka, N. Navab, and K. Mori. "Direct co-calibration of endobronchial ultrasound and video". In: *Proc. Int'l Workshop on Medical Imaging and Augmented Reality (MIAR)*, pp. 513–520, Springer Berlin / Heidelberg, 2010.

[Eber 07]   R. Eberhardt, D. Anantham, F. Herth, D. Feller-Kopman, and A. Ernst. "Electromagnetic navigation diagnostic bronchoscopy in peripheral lung lesions". *Chest*, Vol. 131, No. 6, pp. 1800–1805, June 2007.

[Egli 81]   W. H. Egli, D. Kuhlmann, and J. E. Wier. "Helmet-mounted sighting system". Patent US 4,287,809, Honeywell Inc., September 1981.

[Ells 04]   J. Ellsmere, J. Stoll, W. Wells, R. Kikinis, K. Vosburgh, R. Kane, D. Brooks, and D. Rattner. "A new visualization technique for laparoscopic ultrasonography". *Surgery*, Vol. 136, No. 1, pp. 84–92, July 2004.

[Engl 98]   K.-H. Englmeier, M. Haubner, C. Krapichler, D. Schuhmann, M. Seemann, H. Fürst, and M. Reiser. "Virtual bronchoscopy based on spiral CT images". In: Y. Kim and S. K. Mun, Eds., *Proceedings of SPIE Medical Imaging 1998: Image Display*, pp. 427–438, SPIE, 1998.

[Erik 09]   M.-O. Eriksson, A. Wanhainen, and R. Nyman. "Intravascular ultrasound with a vector phased-array probe (AcuNav) is feasible in endovascular abdominal aortic aneurysm repair". *Acta Radiologica*, Vol. 50, No. 8, pp. 870–875, 2009.

[Fall 10a]   P. Fallavollita, Z. K. Aghaloo, E. C. Burdette, D. Y. Song, P. Abolmaesumi, and G. Fichtinger. "Registration between ultrasound and fluoroscopy or CT in prostate brachytherapy". *Medical Physics*, Vol. 37, No. 6, pp. 2749–2760, 2010.

[Fall 10b]   P. Fallavollita, C. Burdette, D. Song, P. Abolmaesumi, and G. Fichtinger. "C-arm pose estimation in prostate brachytherapy by registration to ultrasound". In: *Proceedings of Int'l Conference on Medical Image Computing and Computer-Assisted Intervention (MICCAI)*, pp. 311–318, Springer Berlin / Heidelberg, 2010.

[Feue 07]   M. Feuerstein, T. Reichl, J. Vogel, A. Schneider, H. Feussner, and N. Navab. "Magneto-optic tracking of a flexible laparoscopic ultrasound transducer for laparoscope augmentation". In: *Proceedings of Int'l Conference on Medical Image Computing and Computer-Assisted Intervention (MICCAI)*, p. 909, Springer Berlin / Heidelberg, November 2007.

[Feue 08a]   M. Feuerstein, T. Mussack, S. M. Heining, and N. Navab. "Intraoperative laparoscope augmentation for port placement and resection planning in minimally invasive liver resection". *IEEE Transactions on Medical Imaging*, Vol. 27, No. 3, pp. 355–369, March 2008.

[Feue 08b]   M. Feuerstein, T. Reichl, J. Vogel, J. Traub, and N. Navab. "New approaches to online estimation of electromagnetic tracking errors for laparoscopic ultrasonography". *Computer Assisted Surgery*, Vol. 13, pp. 311–323, September 2008.

[Feue 09]   M. Feuerstein, T. Reichl, J. Vogel, J. Traub, and N. Navab. "Magneto-optical tracking of flexible laparoscopic ultrasound: model-based online detection and correction of magnetic tracking errors". *IEEE Transactions on Medical Imaging*, Vol. 28, No. 6, pp. 951–967, June 2009.

[Feue 10]   M. Feuerstein, T. Sugiura, D. Deguchi, T. Reichl, T. Kitasaka, and K. Mori. "Marker-free registration for electromagnetic navigation bronchoscopy under respiratory motion". In: *Proc. Int'l Workshop on Medical Imaging and Augmented Reality (MIAR)*, pp. 237–246, Springer Berlin / Heidelberg, 2010.

[Fisc 05a]   G. S. Fischer and R. H. Taylor. "Electromagnetic tracker measurement error simulation and tool design". In: *Proceedings of Int'l Conference on Medical Image Computing and Computer-Assisted Intervention (MICCAI)*, pp. 73–80, Springer Berlin / Heidelberg, 2005.

[Fisc 05b]   G. S. Fischer. *Electromagnetic tracker characterization and optimal tool design (with applications to ENT surgery)*. Master's thesis, Johns Hopkins University, Baltimore, Maryland, April 2005.

[Fitz 98]   J. M. Fitzpatrick, J. B. West, and C. R. Maurer, Jr. "Predicting error in rigid-body point-based registration". *IEEE Transactions on Medical Imaging*, Vol. 14, No. 5, pp. 694–702, October 1998.

[Flei 97]   T. Fleiter, E. M. Merkle, A. J. Aschoff, G. Lang, M. Stein, J. Görich, F. Liewald, N. Rilinger, and R. Sokiranski. "Comparison of real-time virtual and fiberoptic bronchoscopy in patients with bronchial carcinoma: opportunities and limitations". *American Journal of Roentgenology*, Vol. 169, No. 6, pp. 1591–1595, December 1997.

[Fran 03]   D. D. Frantz, A. D. Wiles, S. E. Leis, and S. R. Kirsch. "Accuracy assessment protocols for electromagnetic tracking systems". *Physics in Medicine and Biology*, Vol. 48, No. 14, pp. 2241–2251, July 2003.

[Fran 04]   D. Frantz, S. Kirsch, and A. Wiles. "Specifying 3D tracking system accuracy. One manufacturer's views". In: *Proceedings of Bildverarbeitung für die Medizin (BVM)*, p. 234, Springer, 2004.

[Fran 11]   D. D. Frantz, S. E. Leis, S. Kirsch, and C. Schilling. "System for determining spatial position and/or orientation of one or more objects". Patent US 6,288,785, Northern Digital Inc., September 2011.

[Gabr 96]   C. Gabriel, S. Gabriel, and E. Corthout. "The dielectric properties of biological tissues: I. Literature survey". *Phys Med Biol*, Vol. 41, No. 11, pp. 2231–2249, November 1996.

[Gang 06]   S. Ganguli, J. B. Kruskal, D. D. Brennan, and R. A. Kane. "Intraoperative laparoscopic ultrasound". *Radiologic Clinics of North America*, Vol. 44, pp. 925–935, 2006.

[Gard 13]   J. Gardiazabal, T. Reichl, A. Okur, T. Lasser, and N. Navab. "First flexible robotic intra-operative nuclear imaging for image-guided surgery". In: *Proceedings of Int'l Conference on Information Processing in Computer Assisted Interventions (IPCAI)*, Heidelberg, Germany, June 2013. To appear.

[Gari 10]   F. Garibaldi, R. De Leo, A. Ranieri, F. Loddo, M. Floresta, C. Tamma, A. Gabrielli, F. Giorgi, F. Cusanno, P. Musico, R. Perrino, P. Finocchiaro, L. Cosentino, A. Pappalardo, F. Meddi, B. Maraviglia, F. Giove, T. Gili, S. Capuani, M. Turisini, N. Clinthorne, S. Huh, S. Majewski, M. Lucentini, M. Gricia, F. Giuliani, and E. Monno. "TOPEM: A multimodality probe (PET TOF, MRI, and MRS) for diagnosis and follow up of prostate cancer". In: *Nuclear Science Symposium Conference Record (NSS/MIC), 2010 IEEE*, pp. 2442 –2444, November 2010.

[Gerg 10]   I. Gergel, T. R. dos Santos, R. Tetzlaff, L. Maier-Hein, H.-P. Meinzer, and I. Wegner. "Particle filtering for respiratory motion compensation during navigated bronchoscopy". In: K. H. Wong and M. I. Miga, Eds., *Proceedings of SPIE Medical Imaging 2010: Visualization, Image-Guided Procedures, and Modeling*, p. 76250W, SPIE, 2010.

[Gerg 12]   I. Gergel, J. Gaa, M. Müller, H.-P. Meinzer, and I. Wegner. "A novel fully automatic system for the evaluation of electromagnetic tracker". In: D. R. H. III and K. H. Wong, Eds., *Proceedings of SPIE Medical Imaging 2012: Image-Guided Procedures, Robotic Interventions, and Modeling*, p. 831608, SPIE, 2012.

[Ghaz 95]   M. Ghazisaedy, D. Adamczyk, D. Sandin, R. Kenyon, and T. DeFanti. "Ultrasonic calibration of a magnetic tracker in a virtual reality space". In: *Virtual Reality Annual International Symposium, 1995. Proceedings.*, pp. 179 –188, March 1995.

[Gild 05]   T. Gildea. "Electromagnetic navigation bronchoscopy". *Lung Cancer*, Vol. 49, No. S2, p. S12, 2005.

[Gild 06]   T. R. Gildea, P. J. Mazzone, D. Karnak, M. Meziane, and A. C. Mehta. "Electromagnetic navigation diagnostic bronchoscopy: a prospective study". *American Journal of Respiratory and Critical Care Medicine*, Vol. 174, No. 9, pp. 982–989, November 2006.

[Hanl 99]   J. Hanley, M. M. Debois, D. Mah, G. S. Mageras, A. Raben, K. Rosenzweig, B. Mychalczak, L. H. Schwartz, P. J. Gloeggler, W. Lutz, C. C. Ling, S. A. Leibel, Z. Fuks, and G. J. Kutcher. "Deep inspiration breath-hold technique for lung tumors: the potential value of target immobilization and reduced lung density in dose escalation". *International Journal of Radiation Oncology*Biology*Physics*, Vol. 45, No. 3, pp. 603–611, October 1999.

[Hans 98]   P. K. Hansen. "Hybrid motion tracker". Patent US 5,831,260, Ascension Technology Corporation, November 1998.

[Hapo 99]   E. F. Haponik, S. L. Aquino, and D. J. Vining. "Virtual bronchoscopy". *Clinics in Chest Medicine*, Vol. 20, No. 1, pp. 201–217, March 1999.

[Harm 01]   J. Harms, H. Feussner, M. Baumgartner, A. Schneider, M. Donhauser, and G. Wessels. "Three-dimensional navigated laparoscopic ultrasonography". *Surgical Endoscopy*, Vol. 15, No. 12, pp. 1459–1462, December 2001.

[Hart 03]   R. Hartley and A. Zisserman. *Multiple view geometry in computer vision*. Cambridge University Press, 2nd Ed., 2003.

[Haus 04]   K. Häussinger, A. Ballin, H. D. Becker, P. Bölcskei, R. Dierkesmann, I. Dittrich, W. Frank, L. Freitag, R. Gottschall, W. R. Guschall, W. Hartmann, R. Hauck, F. Herth, D. Kirsten, M. Kohlhäufl, A. Kreuzer, R. Loddenkemper, N. Macha, A. Markus, F. Stanzel, H. Steffen, and M. Wagner. "Recommendations for quality standards in bronchoscopy". *Pneumologie*, Vol. 58, No. 5, pp. 344–356, May 2004.

[Haut 05]   H. Hautmann, A. Schneider, T. Pinkau, F. Peltz, and H. Feussner. "Electromagnetic catheter navigation during bronchoscopy: validation of a novel method by conventional fluoroscopy". *Chest*, Vol. 128, No. 1, pp. 382–387, July 2005.

[Hayh 09]   C. Hayhurst, P. Byrne, P. R. Eldridge, and C. L. Mallucci. "Application of electromagnetic technology to neuronavigation: a revolution in image-guided neurosurgery". *Journal of Neurosurgery*, Vol. 111, No. 6, pp. 1179–1184, 2009.

[Heik 00]   J. Heikkilä. "Geometric camera calibration using circular control points". *IEEE Transactions on Pattern Analysis and Machine Intelligence*, Vol. 22, No. 10, pp. 1066–1077, 2000.

[Heik 97]   J. Heikkilä and O. Silvén. "A four-step camera calibration procedure with implicit image correction". In: *Proc. IEEE Conf. Computer Vision and Pattern Recognition (CVPR)*, pp. 1106–1112, IEEE Computer Society, 1997.

[Heki 10]   C. Hekimian-Williams, B. Grant, X. Liu, Z. Zhang, and P. Kumar. "Accurate localization of RFID tags using phase difference". In: *RFID, 2010 IEEE International Conference on*, pp. 89 –96, April 2010.

[Helf 01]   J. P. Helferty, A. J. Sherbondy, A. P. Kiraly, J. Z. Turlington, E. A. Hoffman, G. McLennan, and W. E. Higgins. "Image-guided endoscopy for lung-cancer assessment". In: *Proc. International Conference on Image Processing*, pp. 307–310, 2001.

[Hild 08]   P. Hildebrand, S. Schlichting, V. Martens, A. Besirevic, M. Kleemann, U. Roblick, L. Mirow, C. Bürk, A. Schweikard, and H.-P. Bruch. "Prototype of an intraoperative navigation and documentation system for laparoscopic radiofrequency ablation: first experiences". *European Journal of Surgical Oncology*, Vol. 34, No. 4, pp. 418–421, April 2008.

[Hoff 00]   W. Hoff and T. Vincent. "Analysis of head pose accuracy in augmented reality". *IEEE Transactions on Visualization and Computer Graphics*, Vol. 6, No. 4, pp. 319–334, 2000.

[Hofs 99]   R. Hofstetter, M. Slomczykowski, M. Sati, and L. P. Nolte. "Fluoroscopy as an imaging means for computer-assisted surgical navigation". *Computer Aided Surgery*, Vol. 4, No. 2, pp. 65–76, 1999.

[Holl 09]   K. Höller, J. Penne, A. Schneider, J. Jahn, J. G. Boronat, T. Wittenberg, H. Feussner, and J. Hornegger. "Endoscopic orientation correction". In: *Proceedings of Int'l Conference on Medical Image Computing and Computer-Assisted Intervention (MICCAI)*, pp. 459–466, Springer Berlin / Heidelberg, 2009.

[Horn 87]   B. Horn. "Closed-form solution of absolute orientation using unit quaternions". *Journal of the Optical Society of America A: Optics, Image Science, and Vision*, Vol. 4, No. 4, pp. 629–642, 1987.

[Horn 88]   B. Horn, H. Hilden, and S. Negahdaripour. "Closed-form solution of absolute orientation using orthonormal matrices". *Journal of the Optical Society of America A: Optics, Image Science, and Vision*, Vol. 5, No. 7, pp. 1127–1135, 1988.

[Houg 62]   P. Hough. "Method and means for recognizing complex patterns". Patent US 3,069,654, December 1962.

[Hous 07]   R. Housden, G. Treece, A. Gee, R. Prager, and T. Street. "Hybrid systems for reconstruction of freehand 3D ultrasound data". CUED/F-INFENG/TR 574, University of Cambridge, Department of Engineering, March 2007.

[Hous 08]   R. J. Housden, A. H. Gee, R. W. Prager, and G. M. Treece. "Rotational motion in sensorless freehand three-dimensional ultrasound". *Ultrasonics*, Vol. 48, No. 5, pp. 412–422, September 2008.

[Hube 06]   J. S. Huber, W. S. Choong, W. W. Moses, J. Qi, J. Hu, G. C. Wang, D. Wilson, S. Oh, R. H. Huesman, S. E. Derenzo, and T. F. Budinger. "Initial results of a positron tomograph for prostate imaging". *IEEE Transactions on Nuclear Science*, Vol. 53, No. 5, pp. 2653–2659, 2006.

[Humm 05]   J. B. Hummel, M. R. Bax, M. L. Figl, Y. Kang, C. Maurer, Jr., W. W. Birkfellner, H. Bergmann, and R. Shahidi. "Design and application of an assessment protocol for electromagnetic tracking systems". *Medical Physics*, Vol. 32, No. 7, pp. 2371–2379, July 2005.

[Humm 06]   J. Hummel, M. Figl, W. Birkfellner, M. R. Bax, R. Shahidi, C. R. Maurer, Jr., and H. Bergmann. "Evaluation of a new electromagnetic tracking system using a standardized assessment protocol". *Physics in Medicine and Biology*, Vol. 51, No. 10, pp. 205–210, May 2006.

[Humm 09]   J. Hummel, M. Figl, M. Bax, R. Shahidi, H. Bergmann, and W. Birkfellner. "Evaluation of dynamic electromagnetic tracking deviation". In: M. I. Miga and K. H. Wong, Eds., *Proceedings of SPIE Medical Imaging 2009: Visualization, Image-Guided Procedures, and Modeling*, p. 72612U, SPIE, 2009.

[Jaki 06]   J. J. Jakimowicz. "Intraoperative ultrasonography in open and laparoscopic abdominal surgery: an overview". *Surgical Endoscopy*, Vol. 20, pp. 425–435, March 2006.

[Jema 08]   A. Jemal, R. Siegel, E. Ward, Y. Hao, J. Xu, T. Murray, and M. J. Thun. "Cancer statistics, 2008". *CA Cancer Journal for Clinicians*, Vol. 58, No. 2, pp. 71–96, 2008.

[Kalm 60]   R. Kalman. "A new approach to linear filtering and prediction problems". *Journal of Basic Engineering*, Vol. 82, No. 1, pp. 35–45, 1960.

[Kham 05]   A. Khamene and F. Sauer. "A novel phantom-less spatial and temporal ultrasound calibration method". In: *Proceedings of Int'l Conference on Medical Image Computing and Computer-Assisted Intervention (MICCAI)*, pp. 65–72, Springer Berlin / Heidelberg, 2005.

[Khar 10]   R. Khare and W. E. Higgins. "Toward image-based global registration for bronchoscopy guidance". In: K. H. Wong and M. I. Miga, Eds., *Proceedings of SPIE Medical Imaging 2010: Visualization, Image-Guided Procedures, and Modeling*, p. 762510, SPIE, 2010.

[Khar 11]   R. Khare and W. E. Higgins. "Image-based global registration system for bronchoscopy guidance". In: K. H. Wong and D. R. H. III, Eds., *Proceedings of SPIE Medical Imaging 2011: Visualization, Image-Guided Procedures, and Modeling*, p. 79640I, SPIE, 2011.

[Khay 11]   Y. Khaykin, R. Oosthuizen, L. Zarnett, Z. A. Wulffhart, B. Whaley, C. Hill, D. Giewercer, and A. Verma. "CARTO-guided vs. NavX-guided pulmonary vein antrum isolation and pulmonary vein antrum isolation performed without 3-D mapping: effect of the 3-D mapping system on procedure duration and fluoroscopy time". *Journal of Interventional Cardiac Electrophysiology*, Vol. 30, No. 3, pp. 233–240, April 2011.

[Kind 00]   V. Kindratenko. "A survey of electromagnetic position tracker calibration techniques". *Virtual Reality: Research, Development, and Applications*, Vol. 5, No. 3, pp. 169–182, 2000.

[Kirs 03]   S. R. Kirsch, H. R. Schild, and C. J. Schilling. "Gain factor and position determination system". Patent US 6,625,563, Northern Digital Inc., September 2003.

[Kirs 06]   S. R. Kirsch, C. Schilling, and G. Brunner. "Assesment of metallic distortions of an electromagnetic tracking system". In: K. R. Cleary, R. L. Galloway, and Jr., Eds., *Proceedings of SPIE Medical Imaging 2006: Visualization, Image-Guided Procedures, and Display*, p. 61410J, SPIE, 2006.

[Klee 06]   M. Kleemann, P. Hildebrand, M. Birth, and H. P. Bruch. "Laparoscopic ultrasound navigation in liver surgery: technical aspects and accuracy". *Surgical Endoscopy*, Vol. 20, No. 5, pp. 726–729, May 2006.

[Klei 06]   G. Klein and D. Murray. "Full-3D edge tracking with a particle filter". In: *Proceedings of the British Machine Vision Conference (BMVC)*, pp. 1119–1128, BMVA, Edinburgh, September 2006.

[Klei 07]   T. Klein, J. Traub, H. Hautmann, A. Ahmadian, and N. Navab. "Fiducial-free registration procedure for navigated bronchoscopy". In: *Proceedings of Int'l Conference on Medical Image Computing and Computer-Assisted Intervention (MICCAI)*, p. 475, Springer Berlin / Heidelberg, 2007.

[Koiz 02]   N. Koizumi, K. Sumiyama, N. Suzuki, A. Hattori, H. Tajiri, and A. Uchiyama. "Development of three-dimensional endoscopic ultrasound system with optical tracking". In: T. Dohi and R. Kikinis, Eds., *Proceedings of Int'l Conference on Medical Image Computing and Computer-Assisted Intervention (MICCAI)*, pp. 60–65, Springer Berlin / Heidelberg, 2002.

[Koni 07]   K. Konishi, M. Nakamoto, Y. Kakeji, K. Tanoue, H. Kawanaka, S. Yamaguchi, S. Ieiri, Y. Sato, Y. Maehara, S. Tamura, and M. Hashizume. "A real-time navigation system for laparoscopic surgery based on three-dimensional ultrasound using magneto-optic hybrid tracking configuration". *International Journal of Computer Assisted Radiology and Surgery*, Vol. 2, No. 1, pp. 1–10, June 2007.

[Kouw 05]   M. C. A. van Kouwen, J. B. M. J. Jansen, H. van Goor, S. de Castro, W. J. G. Oyen, and J. P. H. Drenth. "FDG-PET is able to detect pancreatic carcinoma in chronic pancreatitis". *European Journal of Nuclear Medicine and Molecular Imaging*, Vol. 32, No. 4, pp. 399–404, April 2005.

[Kruc 05]   J. Krücker, A. Viswanathan, J. Borgert, N. Glossop, Y. Yanga, and B. J. Wood. "An electromagnetically tracked laparoscopic ultrasound for multi-modality minimally invasive surgery". In: *Proceedings of Int'l Congress on Computer Assisted Radiology and Surgery (CARS)*, pp. 746–751, May 2005.

[Krum 05]   D. Krum, A. Goel, J. Hauck, J. Schweitzer, J. Hare, M. Attari, A. Dhala, R. Cooley, M. Akhtar, and J. Sra. "Catheter location, tracking, cardiac chamber geometry creation, and ablation using cutaneous patches". *Journal of Interventional Cardiac Electrophysiology*, Vol. 12, pp. 17–22, 2005.

[Kuip 80]   J. B. Kuipers. "SPASYN – an electromagnetic relative position and orientation tracking system". *Instrumentation and Measurement, IEEE Transactions on*, Vol. 29, No. 4, pp. 462 –466, December 1980.

[Kuku 02]   M. Kukuk and B. Geiger. "A real-time deformable model for flexible instruments inserted into tubular structures". In: *Proceedings of Int'l Conference on Medical Image Computing and Computer-Assisted Intervention (MICCAI)*, pp. 331–338, Springer Berlin / Heidelberg, 2002.

[Kupe 07]   P. Kupelian, T. Willoughby, A. Mahadevan, T. Djemil, G. Weinstein, S. Jani, C. Enke, T. Solberg, N. Flores, D. Liu, D. Beyer, and L. Levine. "Multi-institutional clinical experience with the Calypso system in localization and continuous, real-time monitoring of the prostate gland during external radiotherapy". *International Journal of Radiation Oncology*Biology*Physics*, Vol. 67, No. 4, pp. 1088–1098, March 2007.

[Lang 00]   T. Langø. *Ultrasound guided surgery: image processing and navigation*. PhD thesis, Norwegian University of Science and Technology, December 2000.

[Lang 08]   T. Langø, G. A. Tangen, R. Mårvik, B. Ystgaard, Y. Yavuz, J. H. Kaspersen, O. V. Solberg, and T. A. N. Hernes. "Navigation in laparoscopy: prototype research platform for improved image-guided surgery". *Minimally Invasive Therapy and Allied Technologies*, Vol. 17, No. 1, pp. 17–33, 2008.

[Lave 00]   J. Lavest, G. Rives, and J. Lapreste. "Underwater camera calibration". In: *Proceedings of the European Conference on Computer Vision (ECCV)*, pp. 654–668, Springer Berlin / Heidelberg, 2000.

[Leot 97]   D. F. Leotta, P. R. Detmer, and R. W. Martin. "Performance of a miniature magnetic position sensor for three-dimensional ultrasound imaging". *Ultrasound in Medicine & Biology*, Vol. 23, No. 4, pp. 597–609, 1997.

[Leve 05]   J. Leven, D. Burschka, R. Kumar, G. Zhang, S. Blumenkranz, X. D. Dai, M. Awad, G. D. Hager, M. Marohn, M. Choti, C. Hasser, and R. H. Taylor. "DaVinci Canvas: a telerobotic surgical system with integrated, robot-assisted, laparoscopic ultrasound capability". In: *Proceedings of Int'l Conference on Medical Image Computing and Computer-Assisted Intervention (MICCAI)*, pp. 811–818, Springer Berlin / Heidelberg, 2005.

[Leve 44]   K. Levenberg. "A method for the solution of certain problems in least squares". *Quarterly of Applied Mathematics*, Vol. 2, pp. 164–168, 1944.

[Li 04]   Y. Li, R. Aissaoui, M. Lacoste, and J. Dansereau. "Development and evaluation of a new body-seat interface shape measurement system". *IEEE Transactions on Biomedical Engineering*, Vol. 51, No. 11, pp. 2040–2050, November 2004.

[Lind 03a]   F. Lindseth, J. Bang, and T. Langø. "A robust and automatic method for evaluating accuracy in 3-D ultrasound-based navigation". *Ultrasound in Medicine & Biology*, Vol. 29, No. 10, pp. 1439–1452, October 2003.

[Lind 03b]   F. Lindseth, G. A. Tangen, T. Langø, and J. Bang. "Probe calibration for freehand 3-D ultrasound". *Ultrasound in Medicine & Biology*, Vol. 29, No. 11, pp. 1607–1623, November 2003.

[Lore 87] W. Lorensen and H. Cline. "Marching cubes: A high resolution 3D surface construction algorithm". In: *Proceedings of Conference on Computer Graphics and Interactive Techniques (SIGGRAPH)*, pp. 163–169, ACM New York, NY, USA, 1987.

[Luo 10a] X. Luo, M. Feuerstein, T. Sugiura, T. Kitasaka, K. Imaizumi, Y. Hasegawa, and K. Mori. "Towards hybrid bronchoscope tracking under respiratory motion: evaluation on a dynamic motion phantom". In: K. H. Wong and M. I. Miga, Eds., *Proceedings of SPIE Medical Imaging 2010: Visualization, Image-Guided Procedures, and Modeling*, p. 76251B, SPIE, 2010.

[Luo 10b] X. Luo, T. Reichl, M. Feuerstein, T. Kitasaka, and K. Mori. "Modified hybrid bronchoscope tracking based on sequential Monte Carlo sampler: dynamic phantom validation". In: *Asian Conference on Computer Vision*, pp. 409–421, Queenstown, New Zealand, November 2010.

[Luo 11] X. Luo, T. Kitasaka, and K. Mori. "Bronchoscopy navigation beyond electromagnetic tracking systems: a novel bronchoscope tracking prototype". In: *Proceedings of Int'l Conference on Medical Image Computing and Computer-Assisted Intervention (MICCAI)*, pp. 194–202, 2011.

[Ma 08] Y. L. Ma, K. S. Rhode, G. Gao, A. P. King, P. Chinchapatnam, T. Schaeffter, D. J. Hawkes, R. Razavi, and G. P. Penney. "Ultrasound calibration using intensity-based image registration: for application in cardiac catheterization procedures". In: M. I. Miga and K. R. Cleary, Eds., *Proceedings of SPIE Medical Imaging 2008: Visualization, Image-guided Procedures, and Modeling*, p. 69180O, SPIE, 2008.

[Maje 10] S. Majewski and J. Proffitt. "Dedicated mobile high resolution prostate PET imager with an insertable transrectal probe". Patent US 7,858,944, Jefferson Science Associates, LLC, December 2010.

[Mark 10] P. Markelj, D. Tomazevic, B. Likar, and F. Pernus. "A review of 3D/2D registration methods for image-guided interventions". *Medical Image Analysis*, Vol. 16, No. 3, pp. 642–661, 2010.

[Masc 05] C. R. Mascott. "Comparison of magnetic tracking and optical tracking by simultaneous use of two independent frameless stereotactic systems". *Neurosurgery*, Vol. 57, No. 4 Suppl, pp. 295–301; discussion 295–301, October 2005.

[Matt 04] L. Matthews, T. Ishikawa, and S. Baker. "The template update problem". *IEEE Transactions on Pattern Analysis and Machine Intelligence*, Vol. 26, No. 6, pp. 810 –815, June 2004.

[Maur 97] C. R. Maurer, J. M. Fitzpatrick, M. Y. Wang, R. L. Galloway, R. J. Maciunas, and G. S. Allen. "Registration of head volume images using implantable fiducial markers". *IEEE Transactions on Medical Imaging*, Vol. 16, No. 4, pp. 447–462, August 1997.

[Maur 98] C. R. Maurer, R. J. Maciunas, and J. M. Fitzpatrick. "Registration of head CT images to physical space using a weighted combination of points and surfaces". *IEEE Transactions on Medical Imaging*, Vol. 17, No. 5, pp. 753–761, October 1998.

[Miro 09] D. Mirota, R. H. Taylor, M. Ishii, and G. D. Hager. "Direct endoscopic video registration for sinus surgery". In: M. I. Miga and K. H. Wong, Eds., *Proceedings of SPIE Medical Imaging 2009: Visualization, Image-Guided Procedures, and Modeling*, p. 72612K, SPIE, 2009.

[Mori 00] K. Mori, Y. Suenaga, J. ichiro Toriwaki, J. ichi Hasegawa, K. Katada, H. Takabatake, and H. Natori. "Method for tracking camera motion of real endoscope by using virtual endoscopy system". In: C.-T. Chen and A. V. Clough, Eds., *Proceedings of SPIE Medical Imaging 2000: Physiology and Function from Multidimensional Images*, pp. 122–133, SPIE, 2000.

[Mori 01] K. Mori, D. Deguchi, J. Hasegawa, Y. Suenaga, J. Toriwaki, H. Takabatake, and H. Natori. "A method for tracking the camera motion of real endoscope by epipolar geometry analysis and virtual endoscopy system". In: *Proceedings of Int'l Conference on Medical Image Computing and Computer-Assisted Intervention (MICCAI)*, pp. 1–8, Springer, 2001.

[Mori 02] K. Mori, D. Deguchi, J. Sugiyama, Y. Suenaga, J. Toriwaki, C. R. Maurer, H. Takabatake, and H. Natori. "Tracking of a bronchoscope using epipolar geometry analysis and intensity-based image registration of real and virtual endoscopic images". *Medical Image Analysis*, Vol. 6, No. 3, pp. 321–336, September 2002.

[Mori 05] K. Mori, D. Deguchi, K. Akiyama, T. Kitasaka, C. R. Maurer, Y. Suenaga, H. Takabatake, M. Mori, and H. Natori. "Hybrid bronchoscope tracking using a magnetic tracking sensor and image registration". In: *Proceedings of Int'l Conference on Medical Image Computing and Computer-Assisted Intervention (MICCAI)*, pp. 543–550, Springer Berlin / Heidelberg, 2005.

[Mori 06]   K. Mori, D. Deguchi, T. Kitasaka, Y. Suenaga, H. Takabatake, M. Mori, H. Natori, and C. R. Maurer. "Bronchoscope tracking based on image registration using multiple initial starting points estimated by motion prediction". In: *Proceedings of Int'l Conference on Medical Image Computing and Computer-Assisted Intervention (MICCAI)*, pp. 645–652, Springer Berlin / Heidelberg, 2006.

[Moun 10]   P. Mountney, D. Stoyanov, and G.-Z. Yang. "Three-dimensional tissue deformation recovery and tracking". *Signal Processing Magazine, IEEE*, Vol. 27, No. 4, pp. 14 –24, July 2010.

[Much 06]   D. Mucha, B. Kosmecki, and J. Bier. "Plausibility check for error compensation in electromagnetic navigation in endoscopic sinus surgery". *International Journal of Computer Assisted Radiology and Surgery*, Vol. 1, pp. 316–318, 2006.

[Mung 11]   J. Mung, S. Han, and J. T. Yen. "Design and in vitro evaluation of a real-time catheter localization system using time of flight measurements from seven 3.5 MHz single element ultrasound transducers towards abdominal aortic aneurysm procedures". *Ultrasonics*, Vol. 51, No. 6, pp. 768–775, 2011.

[Mura 01]   D. M. Muratore and R. L. Galloway. "Beam calibration without a phantom for creating a 3-D freehand ultrasound system". *Ultrasound in Medicine & Biology*, Vol. 27, No. 11, pp. 1557–1566, November 2001.

[Murr 94]   R. M. Murray, Z. Li, and S. S. Sastry. *A mathematical introduction to robotic manipulation*. CRC Press, 1994.

[Nafi 06]   C. Nafis, V. Jensen, L. Beauregard, and P. Anderson. "Method for estimating dynamic EM tracking accuracy of surgical navigation tools". In: *Proceedings of SPIE Medical Imaging 2006: Visualization, Image-Guided Procedures, and Display*, 2006.

[Nafi 08]   C. Nafis, V. Jensen, and R. v. Jako. "Method for evaluating compatibility of commercial electromagnetic (EM) microsensor tracking systems with surgical and imaging tables". In: M. I. Miga and K. R. Cleary, Eds., *Proceedings of SPIE Medical Imaging 2008: Visualization, Image-guided Procedures, and Modeling*, p. 691820, SPIE, 2008.

[Naga 04]   J. Nagao, K. Mori, T. Enjouji, D. Deguchi, T. Kitasaka, Y. Suenaga, J. Hasegawa, J. Toriwaki, H. Takabatake, and H. Natori. "Fast and accurate bronchoscope tracking using image registration and motion prediction". In: *Proceedings of Int'l Conference on Medical Image Computing and Computer-Assisted Intervention (MICCAI)*, pp. 551–558, Springer Berlin / Heidelberg, 2004.

[Naka 00]   M. Nakamoto, Y. Sato, Y. Tamaki, H. Nagano, M. Miyamoto, T. Sasama, M. Monden, and S. Tamura. "Magneto-optic hybrid 3-D sensor for surgical navigation". In: *Proceedings of Int'l Conference on Medical Image Computing and Computer-Assisted Intervention (MICCAI)*, pp. 839–848, Springer Berlin / Heidelberg, 2000.

[Naka 02]   M. Nakamoto, Y. Sato, M. Miyamoto, Y. Nakamjima, , K. Konishi, M. Shimada, M. Hashizume, and S. Tamura. "3D ultrasound system using a magneto-optic hybrid tracker for augmented reality visualization in laparoscopic liver surgery". In: *Proceedings of Int'l Conference on Medical Image Computing and Computer-Assisted Intervention (MICCAI)*, 2002.

[Naka 08a] M. Nakamoto, K. Nakada, Y. Sato, K. Konishi, M. Hashizume, and S. Tamura. "Intraoperative magnetic tracker calibration using a magneto-optic hybrid tracker for 3-D ultrasound-based navigation in laparoscopic surgery". *IEEE Transactions on Medical Imaging*, Vol. 27, No. 2, pp. 255–270, 2008.

[Naka 08b] M. Nakamoto, O. Ukimura, I. Gill, A. Mahadevan, T. Miki, M. Hashizume, and Y. Sato. "Realtime organ tracking for endoscopic augmented reality visualization using miniature wireless magnetic tracker". In: T. Dohi, I. Sakuma, and H. Liao, Eds., *Proc. Int'l Workshop on Medical Imaging and Augmented Reality (MIAR)*, pp. 359–366, Springer Berlin / Heidelberg, 2008.

[Nava 09]   N. Navab, S. M. Heining, and J. Traub. "Camera augmented mobile C-arm (CAMC): calibration, accuracy study and clinical applications". *IEEE Transactions on Medical Imaging*, Vol. PP, No. 99, pp. 1–1, 2009.

[Nico 09]   S. A. Nicolau, X. Pennec, L. Soler, X. Buy, A. Gangi, N. Ayache, and J. Marescaux. "An augmented reality system for liver thermal ablation: design and evaluation on clinical cases". *Medical Image Analysis*, Vol. 13, No. 3, pp. 494–506, June 2009.

[Niem 11] J. M. Nieminen and S. R. Kirsch. "Eddy current detection and compensation". Patent US 7,957,925, Northern Digital Inc., June 2011.

[Nixo 98] M. A. Nixon, B. C. McCallum, W. R. Fright, and N. B. Price. "The effects of metals and interfering fields on electromagnetic trackers". *Presence: Teleoperators & Virtual Environments*, Vol. 7, No. 2, pp. 204–218, 1998.

[Nolt 95] L.-P. Nolte, L. Zamorano, H. Visarius, U. Berlemann, F. Langlotz, E. Arm, and O. Schwarzenbach. "Clinical evaluation of a system for precision enhancement in spine surgery". *Clinical Biomechanics*, Vol. 10, No. 6, pp. 293–303, September 1995.

[Nort 11] Northern Digital. "Aurora compact field generator data sheet". IL-1070219 Rev 2, August 2011.

[Okat 97] T. Okatani and K. Deguchi. "Shape reconstruction from an endoscope image by shape from shading technique for a point light source at the projection center". *Computer Vision and Image Understanding*, Vol. 66, No. 2, p. 131, 1997.

[Pago 00] N. Pagoulatos, R. N. Rohling, W. S. Edwards, and Y. Kim. "New spatial localizer based on fiber optics with applications in 3D ultrasound imaging". In: S. K. Mun, Ed., *Proceedings of SPIE Medical Imaging 2000: Image Display and Visualization*, pp. 595–602, SPIE, 2000.

[Pago 01] N. Pagoulatos, D. R. Haynor, and Y. Kim. "A fast calibration method for 3-D tracking of ultrasound images using a spatial localizer". *Ultrasound in Medicine & Biology*, Vol. 27, No. 9, pp. 1219–1229, September 2001.

[Pago 98] N. Pagoulatos, W. S. Edwards, D. R. Haynor, and Y. Kim. "Calibration and validation of freehand 3D ultrasound systems based on DC magnetic tracking". In: Y. Kim and S. K. Mun, Eds., *Proceedings of SPIE Medical Imaging 1998: Image Display*, pp. 59–71, SPIE, 1998.

[Park 05] D. M. Parkin, F. Bray, J. Ferlay, and P. Pisani. "Global cancer statistics, 2002". *CA Cancer Journal for Clinicians*, Vol. 55, No. 2, pp. 74–108, 2005.

[Park 07] S.-J. Park, W. L. Rogers, and N. H. Clinthorne. "Design of a very high-resolution small animal PET scanner using a silicon scatter detector insert". *Physics in Medicine and Biology*, Vol. 52, No. 15, pp. 4653–4677, August 2007.

[Paul 10] O. Pauly, H. Heibel, and N. Navab. "A machine learning approach for deformable guide-wire tracking in fluoroscopic sequences". In: *Proceedings of Int'l Conference on Medical Image Computing and Computer-Assisted Intervention (MICCAI)*, pp. 343–350, Springer Berlin / Heidelberg, 2010.

[Penn 98] X. Pennec and N. Ayache. "Uniform distribution, distance and expectation problems for geometric features processing". *Journal of Mathematical Imaging and Vision*, Vol. 9, pp. 49–67, 1998.

[Pete 08] T. Peters and K. Cleary. *Image-guided interventions: technology and applications*. Springer Science + Business Media, 2008.

[Pete 10] M. Peterhans, S. Anderegg, P. Gaillard, T. Oliveira-Santos, and S. Weber. "A fully automatic calibration framework for navigated ultrasound imaging". In: *Proceedings of the International Conference of the IEEE Engineering in Medicine and Biology Society*, pp. 1242–1245, 2010.

[Poon 05] T. C. Poon and R. N. Rohling. "Comparison of calibration methods for spatial tracking of a 3-D ultrasound probe". *Ultrasound in Medicine & Biology*, Vol. 31, No. 8, pp. 1095 – 1108, 2005.

[Poul 02] F. Poulin and L.-P. Amiot. "Interference during the use of an electromagnetic tracking system under OR conditions". *Journal of Biomechanics*, Vol. 35, No. 6, pp. 733–737, June 2002.

[Prag 98a] R. Prager. "Ultrasound machine calibration". Patent WIPO 99/07284, Cambridge University Technical Services, August 1998.

[Prag 98b] R. Prager, R. Rohling, A. Gee, and L. Berman. "Rapid calibration for 3-D freehand ultrasound". *Ultrasound in Medicine and Biology*, Vol. 24, No. 6, pp. 855–869, July 1998.

[Raab 77] F. H. Raab. "Remote object position locater". Patent US 4,054,881, The Austin Company, October 1977.

[Raab 79] F. Raab, E. Blood, T. Steiner, and H. Jones. "Magnetic position and orientation tracking system". *IEEE Transactions on Aerospace and Electronic Systems*, Vol. AES-15, No. 5, pp. 709–718, September 1979.

[Raab 82]   F. H. Raab. "Remote object position and orientation locater". Patent US 4,314,251, The Austin Company, February 1982.

[Rai 08]   L. Rai, J. Helferty, and W. Higgins. "Combined video tracking and image-video registration for continuous bronchoscopic guidance". *International Journal of Computer Assisted Radiology and Surgery*, Vol. 3, No. 3, pp. 315–329, 2008.

[Rama 99]   K. Ramaswamy and W. E. Higgins. "Interactive dynamic navigation for virtual endoscopy". *Computers in Biology and Medicine*, Vol. 29, No. 5, pp. 303–331, September 1999.

[Rash 92]   H. Rashid and P. Burger. "Differential algorithm for the determination of shape from shading using a point light source". *Image and Vision Computing*, Vol. 10, No. 2, pp. 119–127, 1992.

[Rass 09]   J. Rassweiler, M. Baumhauer, U. Weickert, H.-P. Meinzer, D. Teber, L.-M. Su, and V. R. Patel. "The role of imaging and navigation for natural orifice translumenal endoscopic surgery". *J Endourol*, Vol. 23, No. 5, pp. 793–802, May 2009.

[Rau 02]   B. Rau, M. Hünerbein, and P. M. Schlag. "Is there additional information from laparoscopic ultrasound in tumor staging?". *Digestive Surgery*, Vol. 19, pp. 479–483, 2002.

[Reic 07]   T. Reichl. *Online error correction for the tracking of laparoscopic ultrasound*. Master's thesis, Technische Universität München, Munich, July 2007.

[Reic 09]   T. Reichl, J. Passenger, O. Acosta, and O. Salvado. "Ultrasound goes GPU: real-time simulation using CUDA". In: M. I. Miga and K. H. Wong, Eds., *Proceedings of SPIE Medical Imaging 2009: Visualization, Image-Guided Procedures, and Modeling*, p. 726116, February 2009.

[Reic 11]   T. Reichl, X. Luo, M. Menzel, H. Hautmann, K. Mori, and N. Navab. "Deformable registration of bronchoscopic video sequences to CT volumes with guaranteed smooth output". In: *Proceedings of Int'l Conference on Medical Image Computing and Computer-Assisted Intervention (MICCAI)*, pp. 17–24, Springer Berlin / Heidelberg, Toronto, Canada, September 2011.

[Reic 12]   T. Reichl, I. Gergel, M. Menzel, H. Hautmann, I. Wegner, H.-P. Meinzer, and N. Navab. "Real-time motion compensation for EM bronchoscope tracking with smooth output – ex-vivo validation". In: *Proceedings of SPIE Medical Imaging 2012: Image-Guided Procedures, Robotic Interventions, and Modeling*, p. 83163A, SPIE, 2012.

[Reic 13a]   T. Reichl, J. Gardiazabal, and N. Navab. "Electromagnetic servoing – a new tracking paradigm". *IEEE Transactions on Medical Imaging*, 2013. To appear.

[Reic 13b]   T. Reichl, X. Luo, M. Menzel, H. Hautmann, K. Mori, and N. Navab. "Hybrid electromagnetic and image-based tracking of endoscopes with guaranteed smooth output". *International Journal of Computer Assisted Radiology and Surgery*, 2013. To appear.

[Rous 02]   F. Rousseau and C. Barillot. "Quality assessment of electromagnetic localizers in the context of 3D ultrasound". Research Report RR-4408, INRIA, 2002.

[Schm 01]   S. Schmerber and F. Chassat. "Accuracy evaluation of a CAS system: laboratory protocol and results with 6D localizers, and clinical experiences in otorhinolaryngology". *Computer Aided Surgery*, Vol. 6, No. 1, pp. 1–13, 2001.

[Schn 07]   M. Schneider and C. Stevens. "Development and testing of a new magnetic-tracking device for image guidance". In: *Proceedings of SPIE Medical Imaging 2007: Visualization and Image-Guided Procedures*, p. 65090I, SPIE, February 2007.

[Schn 10]   M. R. Schneider. "System and method for measuring position and orientation using distortion-compensated magnetic fields". Patent U 7,788,060, Ascension Technology Corp., August 2010.

[Schw 06]   Y. Schwarz, J. Greif, H. D. Becker, A. Ernst, and A. Mehta. "Real-time electromagnetic navigation bronchoscopy to peripheral lung lesions using overlaid CT images: the first human study". *Chest*, Vol. 129, No. 4, pp. 988–994, April 2006.

[Seem 07]   M. D. Seemann, J. F. Schaefer, and K.-H. Englmeier. "Virtual positron emission tomography/computed tomography-bronchoscopy: possibilities, advantages and limitations of clinical application". *European Radiology*, Vol. 17, No. 3, pp. 709–715, March 2007.

[Seil 00]   P. Seiler, H. Blattmann, S. Kirsch, R. Muench, and C. Schilling. "A novel tracking technique for the continuous precise measurement of tumour positions in conformal radiotherapy". *Physics in Medicine and Biology*, Vol. 45, p. N103, 2000.

[Shah 02] R. Shahidi, M. R. Bax, C. R. Maurer, J. A. Johnson, E. P. Wilkinson, B. Wang, J. B. West, M. J. Citardi, K. H. Manwaring, and R. Khadem. "Implementation, calibration and accuracy testing of an image-enhanced endoscopy system". *IEEE Transactions on Medical Imaging*, Vol. 21, No. 12, pp. 1524–1535, December 2002.

[Shch 10] T. Shchory, D. Schifter, R. Lichtman, D. Neustadter, and B. W. Corn. "Tracking accuracy of a real-time fiducial tracking system for patient positioning and monitoring in radiation therapy". *International Journal of Radiation Oncology*Biology*Physics*, Vol. 78, No. 4, pp. 1227 – 1234, 2010.

[Shen 08] E. Shen, G. Shechter, J. Kruecker, and D. Stanton. "Effects of sensor orientation on AC electromagnetic tracking system accuracy in a CT scanner environment". In: M. I. Miga and K. R. Cleary, Eds., *Proceedings of SPIE Medical Imaging 2008: Visualization, Image-guided Procedures, and Modeling*, p. 691823, SPIE, 2008.

[Sher 00] A. J. Sherbondy, A. P. Kiraly, A. L. Austin, J. P. Helferty, S.-Y. Wan, J. Z. Turlington, T. Yang, C. Zhang, E. A. Hoffman, G. McLennan, and W. E. Higgins. "Virtual bronchoscopic approach for combining 3D CT and endoscopic video". In: *Proceedings of SPIE Medical Imaging 2000: Physiology and Function from Multidimensional Images*, p. 104, SPIE, 2000.

[Shim 05] J. Shimada, K. Itoh, S. Yamaguchi, A. Nishikawa, and F. Miyazaki. "Magnetic navigation system for thoracoscopic surgery of the pig lung partial resection with transbronchial marking". In: *Proceedings of Int'l Congress on Computer Assisted Radiology and Surgery (CARS)*, pp. 752–755, Elsevier, 2005.

[Shiu 89] Y. Shiu and S. Ahmad. "Calibration of wrist-mounted robotic sensors by solving homogeneous transform equations of the form AX=XB". *IEEE Transactions on Robotics and Automation*, Vol. 5, No. 1, pp. 16–29, February 1989.

[Shoe 85] K. Shoemake. "Animating rotation with quaternion curves". In: *Proceedings of Conference on Computer Graphics and Interactive Techniques (SIGGRAPH)*, pp. 245–254, ACM New York, NY, USA, 1985.

[Shoj 01] H. Shoji, K. Mori, J. Sugiyama, Y. Suenaga, J. ichiro Toriwaki, H. Takabatake, and H. Natori. "Camera motion tracking of real endoscope by using virtual endoscopy system and texture information". In: C.-T. Chen and A. V. Clough, Eds., *Proceedings of SPIE Medical Imaging 2001: Physiology and Function from Multidimensional Images*, pp. 122–133, SPIE, 2001.

[Siel 06] T. Sielhorst, M. Feuerstein, J. Traub, O. Kutter, and N. Navab. "CAMPAR: A software framework guaranteeing quality for medical augmented reality". *International Journal of Computer Assisted Radiology and Surgery*, Vol. 1, pp. 29–30, 2006.

[Siel 07] T. Sielhorst, M. Bauer, O. Wenisch, G. Klinker, and N. Navab. "Online estimation of the target registration error for n-ocular optical tracking systems". In: *Proceedings of Int'l Conference on Medical Image Computing and Computer-Assisted Intervention (MICCAI)*, pp. 652–659, 2007.

[Solb 09] O. V. Solberg, T. Langø, G. A. Tangen, R. Mårvik, B. Ystgaard, A. Rethy, and T. A. N. Hernes. "Navigated ultrasound in laparoscopic surgery". *Minimally Invasive Therapy and Allied Technologies*, Vol. 18, No. 1, pp. 36–53, 2009.

[Solo 00] S. B. Solomon, P. White, C. M. Wiener, J. B. Orens, and K. P. Wang. "Three-dimensional CT-guided bronchoscopy with a real-time electromagnetic position sensor: a comparison of two image registration methods". *Chest*, Vol. 118, No. 6, pp. 1783–1787, December 2000.

[Solo 98] S. B. Solomon, P. White, D. E. Acker, J. Strandberg, and A. C. Venbrux. "Real-time bronchoscope tip localization enables three-dimensional CT image guidance for transbronchial needle aspiration in swine". *Chest*, Vol. 114, No. 5, pp. 1405–1410, November 1998.

[Sope 09] T. D. Soper, D. R. Haynor, R. W. Glenny, and E. J. Seibel. "Validation of CT-video registration for guiding a novel ultrathin bronchoscope to peripheral lung nodules using electromagnetic tracking". In: M. I. Miga and K. H. Wong, Eds., *Proceedings of SPIE Medical Imaging 2009: Visualization, Image-Guided Procedures, and Modeling*, p. 72610C, SPIE, 2009.

[Sope 10] T. Soper, D. Haynor, R. Glenny, and E. Seibel. "In vivo validation of a hybrid tracking system for navigation of an ultrathin bronchoscope within peripheral airways". *IEEE Transactions on Biomedical Engineering*, Vol. 57, No. 3, pp. 736–745, 2010.

[Spar 03]   M. Sparmann, B. Wolke, H. Czupalla, D. Banzer, and A. Zink. "Positioning of total knee arthroplasty with and without navigation support". *Journal of Bone & Joint Surgery, British Volume*, Vol. 85-B, No. 6, pp. 830–835, 2003.

[Stol 05]   J. Stoll and P. Dupont. "Passive markers for ultrasound tracking of surgical instruments". In: *Proceedings of Int'l Conference on Medical Image Computing and Computer-Assisted Intervention (MIC-CAI)*, pp. 41–48, Springer Berlin / Heidelberg, 2005.

[Stro 08]   K. H. Strobl and G. Hirzinger. "More accurate camera and hand-eye calibrations with unknown grid pattern dimensions". In: *Proceedings of IEEE International Conference on Robotics and Automation (ICRA)*, pp. 1398–1405, Pasadena, CA, USA, May 2008.

[Sute 04]   M. J. Suter, J. M. Reinhardt, M. Sonka, W. E. Higgins, E. A. Hoffman, and G. McLennan. "Three-dimensional true color topographical analysis of the pulmonary airways". In: A. A. Amini and A. Manduca, Eds., *Proceedings of SPIE Medical Imaging 2004: Physiology, Function, and Structure from Medical Images*, pp. 189–198, SPIE, 2004.

[Tai 05]   Y.-C. Tai. "Method and apparatus for increasing spatial resolution of a PET scanner". Patent US 6,946,658, Washington University, September 2005.

[Tang 03]   J. Tang and K. Cleary. "Breakdown of tracking accuracy for electromagnetically guided abdominal interventions". In: *Proceedings of Int'l Congress on Computer Assisted Radiology and Surgery (CARS)*, pp. 452–459, Elsevier, 2003.

[Tebo 96]   S. Tebo, D. Leopold, D. Long, S. Zinreich, and D. Kennedy. "An optical 3D digitizer for frameless stereotactic surgery". *IEEE Computer Graphics and Applications*, Vol. 16, No. 1, pp. 55 –64, January 1996.

[Trau 08]   J. Traub, T. Sielhorst, S. M. Heining, and N. Navab. "Advanced display and visualization concepts for image guided surgery". *Journal of Display Technology*, Vol. 4, No. 4, pp. 483–490, 2008.

[Tree 03]   G. M. Treece, A. H. Gee, R. W. Prager, C. J. C. Cash, and L. H. Berman. "High-definition freehand 3-D ultrasound". *Ultrasound in Medicine and Biology*, Vol. 29, No. 4, pp. 529–546, 2003.

[Tsai 87]   R. Tsai. "A versatile camera calibration technique for high accuracy". *IEEE Journal of Robotics and Automation*, Vol. 3, No. 4, pp. 323–344, August 1987.

[Tsai 89]   R. Y. Tsai and R. K. Lenz. "A new technique for fully autonomous and efficient 3D robotics hand/eye calibration". *IEEE Transactions on Robotics and Automation*, Vol. 5, No. 3, pp. 345–358, 1989.

[Umey 91]   S. Umeyama. "Least-squares estimation of transformation parameters between twopoint patterns". *IEEE Transactions on Pattern Analysis and Machine Intelligence*, Vol. 13, No. 4, pp. 376–380, 1991.

[Vett 07]   M. Vetter, I. Wolf, I. Wegner, H.-P. Meinzer, and H. Becker. "Incremental real-time recording of tracked instruments in tubular organ structures inside the human body". Patent application US 20080033452, Deutsches Krebsforschungszentrum, Heidelberg, February 2007.

[Viol 97]   P. Viola and W. Wells III. "Alignment by maximization of mutual information". *International Journal of Computer Vision*, Vol. 24, No. 2, pp. 137–154, 1997.

[Visw 04]   A. Viswanathan, E. Boctor, R. Taylor, G. Hager, and G. Fichtinger. "Immediate ultrasound calibration with three poses and minimal image processing". In: *Proceedings of Int'l Conference on Medical Image Computing and Computer-Assisted Intervention (MICCAI)*, pp. 446–454, Springer, 2004.

[Voge 12]   J. Vogel, T. Reichl, N. Navab, and T. Lasser. "Optimization of Acquisition Geometry for Intraoperative Tomographic Imaging". In: *Proceedings of Int'l Conference on Medical Image Computing and Computer-Assisted Intervention (MICCAI)*, pp. 42–49, Springer Berlin / Heidelberg, Nice, France, October 2012.

[Vogt 02]   S. Vogt, A. Khamene, F. Sauer, and H. Niemann. "Single camera tracking of marker clusters: multiparameter cluster optimization and experimental verification". In: *Proceedings of IEEE and ACM International Symposium on Mixed and Augmented Reality (ISMAR)*, pp. 127 – 136, 2002.

[Voro 06]   S. Voros, J.-A. Long, and P. Cinquin. "Automatic localization of laparoscopic instruments for the visual servoing of an endoscopic camera holder". In: *Proceedings of Int'l Conference on Medical Image Computing and Computer-Assisted Intervention (MICCAI)*, pp. 535–542, Springer Berlin / Heidelberg, 2006.

[Wagn 02] A. Wagner, K. Schicho, W. Birkfellner, M. Figl, R. Seemann, F. König, F. Kainberger, and R. Ewers. "Quantitative analysis of factors affecting intraoperative precision and stability of optoelectronic and electromagnetic tracking systems". *Medical Physics*, Vol. 29, No. 5, pp. 905–912, 2002.

[Walk 91] M. Walker, L. Shao, and R. Volz. "Estimating 3-D location parameters using dual number quaternions". *CVGIP: Image Understanding*, Vol. 54, No. 3, pp. 358–367, 1991.

[Wegn 08] I. Wegner, R. Tetzlaff, J. Biederer, I. Wolf, and H. Meinzer. "An evaluation environment for respiratory motion compensation in navigated bronchoscopy". In: *Proceedings of SPIE Medical Imaging*, p. 691811, SPIE, 2008.

[Wein 07] W. Wein, A. Khamene, D. Clevert, O. Kutter, and N. Navab. "Simulation and fully automatic multimodal registration of medical ultrasound". In: *Proceedings of Int'l Conference on Medical Image Computing and Computer-Assisted Intervention (MICCAI)*, pp. 136–143, Springer Berlin / Heidelberg, October 2007.

[Wein 08] W. Wein and A. Khamene. "Image-based method for in-vivo freehand ultrasound calibration". In: *Proceedings of SPIE Medical Imaging 2008: Ultrasonic Imaging and Signal Processing*, p. 69200K, SPIE, February 2008.

[Wein 10] J. T. Weinhandl, B. S. R. Armstrong, T. P. Kusik, R. T. Barrows, and K. M. O'Connor. "Validation of a single camera three-dimensional motion tracking system". *Journal of Biomechanics*, Vol. 43, No. 7, pp. 1437–1440, May 2010.

[Weng 06] C. Wengert, M. Reeff, P. Cattin, and G. Szekely. "Fully automatic endoscope calibration for intraoperative use". In: *Proceedings of Bildverarbeitung für die Medizin (BVM)*, pp. 419–423, Springer Berlin / Heidelberg, 2006.

[West 04] J. B. West and J. Maurer, C. R. "Designing optically tracked instruments for image-guided surgery". *IEEE Transactions on Medical Imaging*, Vol. 23, No. 5, pp. 533–545, 2004.

[Wile 04] A. D. Wiles, D. G. Thompson, and D. D. Frantz. "Accuracy assessment and interpretation for optical tracking systems". In: R. L. Galloway and Jr., Eds., *Proceedings of SPIE Medical Imaging 2004: Visualization, Image-Guided Procedures, and Display*, pp. 421–432, SPIE, 2004.

[Wile 10] A. D. Wiles and T. M. Peters. "Target tracking errors for 5D and 6D spatial measurement systems". *IEEE Transactions on Medical Imaging*, Vol. 29, No. 3, pp. 879–894, March 2010.

[Will 06] T. R. Willoughby, P. A. Kupelian, J. Pouliot, K. Shinohara, M. Aubin, M. Roach, L. L. Skrumeda, J. M. Balter, D. W. Litzenberg, S. W. Hadley, J. T. Wei, and H. M. Sandler. "Target localization and real-time tracking using the Calypso 4D localization system in patients with localized prostate cancer". *International Journal of Radiation Oncology*Biology*Physics*, Vol. 65, No. 2, pp. 528–534, June 2006.

[Will 11] A. Wille, M. Broll, and S. Winter. "Phase difference based RFID navigation for medical applications". In: *Proceedings of IEEE International Conference on RFID (RFID)*, pp. 98 –105, April 2011.

[Wils 07] E. Wilson, Z. Yaniv, H. Zhang, C. Nafis, E. Shen, G. Shechter, A. D. Wiles, T. Peters, D. Lindisch, and K. Cleary. "A hardware and software protocol for the evaluation of electromagnetic tracker accuracy in the clinical environment: a multi-center study". In: K. R. Cleary and M. I. Miga, Eds., *Proceedings of SPIE Medical Imaging 2007: Visualization and Image-Guided Procedures*, p. 65092T, SPIE, 2007.

[Wu 04] C.-H. Wu, Y.-C. Chen, C.-Y. Liu, C.-C. Chang, and Y.-N. Sun. "Automatic extraction and visualization of human inner structures from endoscopic image sequences". In: A. A. Amini and A. Manduca, Eds., *Proceedings of SPIE Medical Imaging 2004: Physiology, Function, and Structure from Medical Images*, pp. 464–473, SPIE, 2004.

[Yama 04] T. Yamaguchi, M. Nakamoto, Y. Sato, K. Konishi, M. Hashizume, N. Sugano, H. Yoshikawa, and S. Tamura. "Development of a camera model and calibration procedure for oblique-viewing endoscopes". *Computer Aided Surgery*, Vol. 9, No. 5, pp. 203–214, 2004.

[Yani 09] Z. Yaniv, E. Wilson, D. Lindisch, and K. Cleary. "Electromagnetic tracking in the clinical environment". *Medical Physics*, Vol. 36, No. 3, pp. 876–892, 2009.

[Youd 50] W. J. Youden. "Index for rating diagnostic tests". *Cancer*, Vol. 3, No. 1, pp. 32–35, 1950.

[Zhan 00]   Z. Zhang. "A flexible new technique for camera calibration". *IEEE Transactions on Pattern Analysis and Machine Intelligence*, Vol. 22, No. 11, pp. 1330–1334, November 2000.

[Zhan 99]   Z. Zhang. "Flexible camera calibration by viewing a plane from unknown orientations". In: *Proceedings of IEEE International Conference on Computer Vision (ICCV)*, pp. 666–673, 1999.